2020

# Gas Adsorption in Carbon Nanohorns: Equilibrium and Kinetics

Justin Matthew Petucci

# Gas Adsorption in Carbon Nanohorns: Equilibrium and Kinetics

A Dissertation

Presented to

the Faculty of the College of Natural Sciences and Mathematics

University of Denver

In Partial Fulfillment

of the Requirements for the Degree

Doctor of Philosophy

by

Justin M. Petucci

June 2020

Advisor: Dr. M. Mercedes Calbi

Author: Justin M. Petucci
Title: Gas Adsorption in Carbon Nanohorns: Equilibrium and Kinetics
Advisor: Dr. M Mercedes Calbi
Degree Date: June 2020

# Abstract

A study of gas adsorption has been carried out with the focus of better understanding the relationships between the individual properties of the adsorbent/adsorbate (*e.g.* material structure, interactions, gas size and shape, etc.) and the overall adsorptive properties of the combined system (*e.g.* capacity, binding strength, equilibration time, etc.) as a function of thermodynamical variables. This is useful from the perspective of a comprehensive and fundamental understanding as well as for practical applications. The equilibrium regime of adsorption on carbon nanostructure materials (nanohorns, nanotubes, and graphite) is investigated using molecular statics (MS) and grand canonical monte carlo (GCMC) methods for a variety of gas species (carbon dioxide, ethane, argon, etc.). Through the controlled variation and comparison of these simulations, interaction and structural models are developed to help interpret and understand experimental observations. For the case of the adsorption of ethane on closed carbon nanohorns, the lack of distinct features in the adsorption data was found to be a result of binding on exterior sites of the aggregate as well as the increased degrees of freedom of the molecular species. The isosteric heat of adsorption of carbon dioxide on both carbon nanotubes and nanohorns has been experimentally shown to trend through a minimum before approaching the bulk value, which contradicts what is observed for all other adsorbate species. Here it is

shown that carbon dioxide's unique behavior is due to the increased gas-gas interactions which are present due to its quadrupole moment. In order to study the effect of complex geometries and inhomogeneous interaction profiles in the kinetic regime, such as those present in carbon nanohorns, a general 3D on-lattice KMC modelling scheme was developed. A lattice model for carbon nanohorns was developed within this scheme and preliminary calculations show the variation of binding energy along the length of the pore serves to reduce the time to reach equilibrium as well as causes higher site occupancy near the bottom of the pore.

# Acknowledgements

I would like to express my sincerest gratitude to my dissertation advisor, Dr. María de las Mercedes Calbi. Her knowledge and expertise, patience, guidance, and availability have been paramount in the completion of this project. I would like to thank the University of Denver Physics and Astronomy department, in particular Dr. Davor Balzar and Dr. Kingshuk Ghosh for serving on my dissertation committee. I would also like to thank Dr. Aldo Migone for serving as a special member of my committee. Finally, I wish to thank my family for their unquestioning love and support over the years.

# Table of Contents

# List of Figures

# Chapter 1

# Introduction

A fundamental and comprehensive understanding of adsorption has been the pursuit of much scientific inquiry. From the many practical applications such as gas storage, separation, and purification to its prevalence in natural systems, this understanding is poised for continual societal and scientific impact. Today, this may be more true than ever with the incessant progression of global warming due to the build-up of greenhouse gases in the Earth's atmosphere[1]. While much theoretical and experimental work has contributed greatly to our knowledge in this area[2, 3, 4], the emergence of complex adsorbent materials (carbon materials, MOFs, zeolites, etc) and their potential applications necessitates further investigation. Porous materials or those that otherwise impose geometric restrictions, complex adsorbate gases with high internal degrees of freedom, as well as gas mixtures, present new theoretical challenges. A diverse range of adsorbate material phases and dimensions arise on the surfaces and in the pores of these materials, providing not only an opportunity to

probe and characterize the adsorbent but also to explore the behavior of matter in confined environments.

Carbon-based sorbents are one class of materials of particular interest in this area due to the highly desirable adsorptive properties that their unique, stable, and tunable geometries are believed to present, such as high storage capacity, strong binding, and fast kinetics. Two relatively new materials that fall into this class are single walled carbon nanotubes (SWNTs) [5] and single walled carbon nanohorns (SWNHs)[6]. These $sp^2$ hybridized forms of carbon can be thought of as being constructed out of a single graphene sheet that has been appropriately rolled and connected in such a way as to define a hollow and seamless surface with well-defined interior and exterior regions. Nanotubes are cylindrical in form, while nanohorns are conical like with a radius that varies along its length. Both individual SWNTs and SWNHs coalesce under attractive Van der Waals forces[7]. Nanotubes come together to form hexagonally packed bundles comprised of up to hundreds of individual tubes.[8] These bundles present multiple distinct potential adsorption sites to gases on both the interior and exterior regions. Nanohorns do not accumulate into cylindrical bundles like nanotubes, instead they form spherical aggregates[7, 9, 10]. While the configurational nature of these aggregates varies depending on the specifics of their production conditions, in the dahlia-like form thousands of the nanohorns are aligned radially with their capped tip oriented outwards.[6, 10, 11]. As with nanotube bundles, the aggregate form produces unique and distinct internal and external binding regions.

The purpose of this work is to enhance the understanding of adsorption on the aforementioned materials. Through the variation of structural models, interactions, adsorbates, etc. both the material specific and fundamental parameters and processes

that govern adsorption are investigated using computational simulations. This is facilitated through a strong collaboration between the Calbi group (at the University of Denver) and the (now former) experimental Migone group (at Southern Illinois University). This hybrid computational and experimental approach allows for the computational models to be validated which can then, in turn, be used to interpret and explain experimental observations. As discussed in later chapters, the explanatory power of the computational approaches is rooted in the ability to easily view the microscopic system configurations.

For a thorough treatment, it is imperative to study both the aspects of adsorption associated with the thermodynamic equilibrium of the adsorbed phase with the external gas and the time evolution of how the system reaches such an equilibrium state as determined by the underlying kinetic processes at play. Equilibrium information includes the composition and structure of the adsorbed phase, storage capacity of the adsorbent, etc. as a function of thermodynamic variables in addition to binding site locations and energies. With the kinetic regime, the focus is turned to the time-frame that adsorption takes place where quantities such as the rate of gas adsorption and equilibration times are determined.

The majority of effort in this study is concentrated on the equilibrium regime where several experimentally motivated questions are addressed. Experimental isotherm measurements[12, 13, 14] on unopened dahlia-like carbon nanohorns show smoother steps for spherical adsorbate gases (Ne, Ar, $CF_4$) (as compared to other sorbents) and practically a complete lack of steps for ethane and carbon dioxide. The reason for this change in behavior for different adsorbates is investigated through the simulation of gas adsorption using grand canonical Monte Carlo (GCMC) methods on several

different model structures. These structures are represented under the continuous carbon approximation using an extension built into LAMMPS[15] which enables the ability to compute interactions for arbitrarily parameterized surfaces.

Gas adsorption on as produced carbon nanotubes has been extensively studied for a variety of sorbate species such as $H_2$, $N_2$, $CH_4$, $CF_4$, $C_2H_6$, etc.[16, 17, 18, 19] The common equilibrium adsorptive behavior amongst these adsorbates includes the presence of two isotherm steps, which corresponds to adsorption in two energetically distinct binding sites. This isosteric heat of adsorption displays a monotonically decreasing dependence with coverage which achieves the maximum value at low coverage and approaches the corresponding bulk latent heat at high coverage. Experimental adsorption measurements conducted for $CO_2$ on this sorbent[17, 20] show results that contrast the set of common characteristics presented by the other adsorbates. Using both molecular statics (MS) and GCMC simulations, the unique behavior of carbon dioxide is elicited in this study.

A strong emphasis is placed on both carbon dioxide and ethane adsorbate species. From a practical standpoint, $CO_2$ sorption attracts much interest due to the various industrial applications which are centered around the capture and separation of the gas.[21, 22, 23]. More fundamentally there is interest due to $CO_2$'s unique gas-gas interactions, which manifest in a host of unique adsorptive properties. For ethane, its position as a model linear sorbate allows for the general examination of the relationship between the sorbate/sorbent structure and the ultimate adsorptive properties of a given system.

For the kinetic regime, the initial aim was to investigate the effect that more complex sorbent geometries and interactions can have on the dynamics of the system and

to identify the key parameters/processes at play. This was prompted by experimental results from the Migone lab[14] which showed a reversal in trend for the equilibration time for the adsorption of ethane on as produced carbon nanohorns (as compared to the behavior on graphite and closed carbon nanotubes). Additionally carbon dioxide exhibits an equilibration time that increases with coverage on open and closed nanohorns as well as nanotube bundles. This behavior is in contrast to the typical behavior of a simple adsorbate (Ne, Ar, $CF_4$) which displays a decreasing trend of the equilibration time with coverage. It became apparent that the modelling scheme used in our group's previous kinetic modelling efforts[24, 25, 26, 27, 28, 29] was inflexible and designed in an ad-hoc manner, where significant alterations to the underlying code base would be required to model more complex systems. This served to spur the development of a much more general 3D on-lattice kinetic Monte Carlo (KMC) modelling scheme based off the open source SPPARKS[30] code. Under this scheme, there is significant flexibility to model complex systems of varying lattice structure, interactions, rate constants, adsorbate species, etc. without requiring alterations to the code. The performance of the code also allows for the simulation of much larger systems due to the implementation of more efficient solvers which have better scaling as the number of possible moves in the system increases. As a first step toward addressing the original kinetic aim, a model for carbon nanohorns is developed within the new scheme which encompasses the salient features of the sorbent's unique conical pores. Preliminary KMC simulations on this system are conducted and discussed.

In this initial portion of Chapter 1 the purpose and merit of this work have been stated along with a brief overview of some specific knowledge gaps that the study aspires to close. The remaining sections of this chapter contain relevant background

information as well as a literature review of relevant work in the field. In Chapter 2, the methods and procedures are described. Chapters 3 and 4 contain a summary and discussion of the equilibrium and kinetic results. The project is concluded in Chapter 5 with a summary and recap of important findings.

## 1.1 Background

### 1.1.1 Adsorption

If we consider a substrate material (sorbent/adsorbent) that is exposed to a gaseous species (sorbate/adsorbate), adsorption is the spontaneous process ($\Delta G < 0$) in which molecules from the gas adhere to the surfaces and pores of the substrate, as depicted in Figure 1.1. Upon adsorption, energy is released ($\Delta H < 0$) into the surroundings and in the adsorbed phase the gas experiences a reduction in the degrees of freedom ($\Delta S < 0$). The gas-gas and gas-substrate interactions along with the adsorbent/adsorbate structures, the system temperature, pressure, and kinetic processes all factor into determining the properties of the adsorbed phase. Generally,

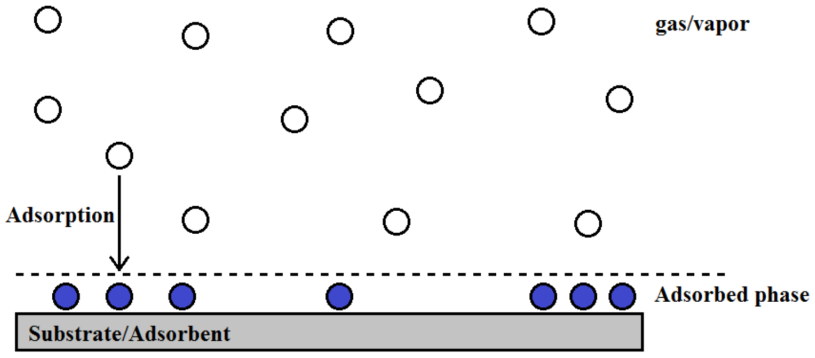


Figure 1.1: An idealized depiction of the adsorption process.

adsorption is broken into two categories: physical adsorption (physisorption) and chemical adsorption (chemisorption). This distinction is due to the differing binding energies associated with the two regimes. Physisorption is the weaker of the two, usually in the meV range, and is due to Van de Waals (dispersion)[31] forces acting between the gas and material. During this type of adsorption, the electronic structure of the sorbent and sorbate is not significantly perturbed. Chemisorption is much higher energy (eV range) where chemical bonds are formed and broken. This causes significant electronic structure changes to occur. For the gases and materials studied in this investigation, we will focus on the physisorption regime.

With adsorption there are two temporal regimes: kinetic and equilibrium. During the kinetic phase the system is dynamic and there is a net flux of molecules adsorbing. Here we are interested in following the evolution of the system as it reaches equilibrium; items of interest may include the equilibration time, adsorption rates, the coverage as a function of time, system configurations etc. Once the system reaches equilibrium, quantities are constant, on average, such that the number of adsorption events balances out the number of desorption events. Information such as how much adsorbate can be taken up by the sorbent (effective area and pore volume), the adsorbed phase structure, how strongly each gas species is bound to the material (binding sites and energies) along with how those values change as a function of pressure and temperature can be determined at equilibrium. A complete understanding of adsorption requires a study of both of these regimes.

### 1.1.2 Carbon Nanohorns and Nanotubes

The study of carbon-based materials, especially those with $sp^2$ hybridization, such as graphite, carbon nanotubes, fullerene, and graphene have attracted much theoretical and experimental attention in the recent years. These various forms of carbon exhibit interesting and unique electrical, mechanical, optical, thermal, and adsorptive properties that elicit many proposed practical applications. Additionally, their geometry provides an ideal environment for research in zero (fullerenes), one (nanotubes), and two dimensions (graphene). In 1999, a new type of single walled carbon was discovered in aggregate form, the nanohorn.[6]. This was proceeded by the discovery of carbon nanotubes almost a decade earlier. Individual single walled carbon nanohorns (SWNHs) were not isolated until 10 years after their initial discovery due to the difficulty in separating them from their preferred aggregate form.[32].

Like fullerenes and single walled carbon nanotubes (SWNTs), nanohorns can be thought of as being constructed out of a single graphene sheet that has been appropriately rolled and connected in such a way as to define a hollow and seamless surface with well-defined interior and exterior regions. The cylindrical nanotube has a length and diameter ranging from 100-1000 nm and 0.8-1.2 nm, respectively. Unlike SWNTs, the nanohorns are conical like and irregular with a varying diameter (2-5 nm) along their length (30-50 nm).[9, 10]. Generally, one of the nanohorn's ends is closed with a conical like cap while the other is flat or rounded.[9, 10] Though, through chemical treatment, the closed cap can be opened allowing for nanohorns to present in both open and closed varieties. This opening process is significantly eased due to the highly defective nature of nanohorns.[9, 33] In their closed form inter-nanohorn pores, defined as the region between nanohorns of the aggregate, are available. With

open nanohorns, intra-nanohorn pores in the interior region of the individual opened nanohorns are also accessible.

Nanotubes come together to form hexagonally packed cylindrical bundles which can be comprised of 100's-1000's of individual tubes with typical wall to wall separations of 3.2-3.4 Å. Nanohorns do not accumulate into bundles like nanotubes, instead they form spherical aggregates (80 -100 nm).[9, 10] The configurational nature of these aggregates varies depending on the specifics of their production conditions.[10, 11]. Four distinct categories of these aggregates have been identified: dahlia-like, bud-like, seed-like, and petal-like.[34] In the dahlia- like form, which is the aggregate of interest in this study, thousands of the nanohorns are aligned radially with their capped tip on the sphere's outer surface.[6]. Figure 1.2 depicts an idealized representation of an individual carbon nanohorn dahlia-like spherical aggregate as well as a idealized nanotube bundle. In this view, four adsorption sites are identified for each sorbent. For the nanohorns this includes two sites of strong binding (deep in the inter- nanohorn conical pore and the intra-nanohorn pore at the tips of the horns) and two of weak binding (on the outside of the nanohorn surfaces). Similarly, nanotube bundles have two inner sites, the interior of the nanotubes and the interstitial region between nanotubes. On the exterior there are two additional sites, in the groove between adjacent tubes and on the exterior of individual tubes.

The high interest in the dahlia-like spherical aggregates stems from their unique radial arrangement which creates large conical like pores (due to the decrease in wall to wall separation going from the exterior of the aggregate to its center). These interstitial sites, unlike those of nanotube bundles, are believed to be highly accessible. They should provide high energy binding sites with fast kinetics, both of which are

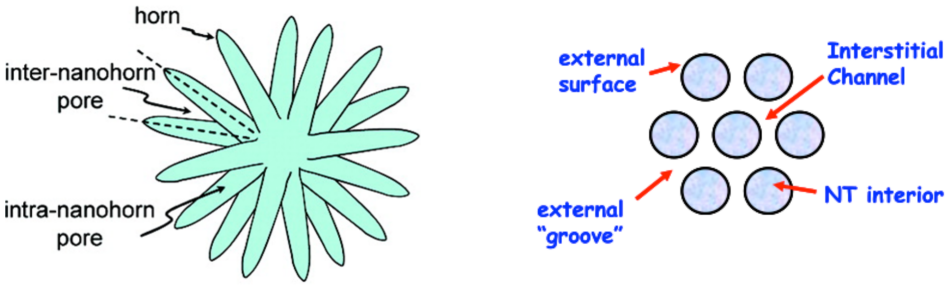


Figure 1.2: Idealized depiction of a spherical carbon nanohorn aggregate (left) and carbon nanotube bundle (right) with labelled potential adsorption sites.

highly desirable characteristics of an adsorbent material. For nanotubes, the interest is centered around the ability of the bundles to produce low dimensional phases of matter through adsorption on the inside of the tubes as well as the groove sites on the exterior.

## 1.2 Literature Review

The availability of the interstitial channel (IC) sites present in a nanotube bundle has attracted both experimental[35] and theoretical[36, 37] attention. Experimentally, Talapatra *et al.* measured the adsorptive properties of Xe, $CH_4$, and Ne on SWNT bundles. It was determined that the binding energies on these materials exceeded that on planar graphite by 75%. By comparing the effective specific area for the different sized adsorbates, it was determined that there was no adsorption in the interstitial channels. Additionally it is concluded that He adsorption in the interstitial channel is unlikely given its similar increase in binding energy. Grand canonical Monte Carlo simulations performed by LaBrosse *et al.* came to a similar conclusion, that gases do not adsorb in non-defect interstitial channels. The identification of defect ICs, which

could occur in bundles comprised of tubes with different diameters, where found to be large enough to accommodate gas adsorption.

In a study of the adsorption of Ne and $CH_4$ on closed dahlia-like nanohorns by Krungleviciute *et al.*[9] two steps were found in the experimental adsorption isotherms before monolayer completion. In order to explain this behavior, the aggregate's interstitial conical pores were modeled by considering the adsorption region between nanotubes with two characteristic separation distances. This different separation creates adsorption regions with high and low binding energy, mimicking the interstitial adsorption region of the more complicated aggregate conical nanohorn geometry. Within this model, Krungleviciute *et al.* were then able to explain the presence of the isotherm steps as two distinct adsorption sites in the monolayer regime. High energy binding occurs near the center of the aggregate at the base of the nanohorns at low pressure. At higher pressures, low energy binding sites on the exterior of the nanohorn walls and capped tips are active. The similar behavior of sorbates of different size strongly suggests that the interstitial sites are easily accessible due to the radial configuration of the nanohorns.[9] While this model adequately explained the experimental isotherm data, it greatly simplified the interstitial conical structure using a continuous parallel nanotube approximation with just two tube separation distances. In addition, this study only considered spherical sorbates with zero electrostatic multipole moments. It is expected that the use of a more complex model that includes the radial packing and a wider variety of sorbate gases may elicit greater detail of the interstitial pore structure along with more accurate isosteric heat values.

Adsorption on nanohorn aggregates has been extensively studied for a variety of adsorbates. In a combined experimental and computational study of $N_2$[38, 39, 40] the

presence of strong and accessible internal and external adsorption sites were confirmed through the analysis of isotherm data. Using a structural model of a tube with a sharply capped tip, an internal pore width of 2.9 nm was found. Methane adsorption was experimentally studied by Murata [41] where an enhancement effect was observed. As the adsorption in the interstitial spaces increased, the internal regions showed a corresponding concentration increase. This was attributed to the presence of holes in the nanohorn sidewalls which provide access as the exterior coverage increases.

The adsorption of $CO_2$ was carried out by Krungleviciute *et al.*[42] on closed dahlia-like nanohorn aggregates for six temperatures ranging from 147-193 K. The behavior of the $CO_2$ sorbate was found to significantly deviate from that of $CH_4$ and Ne in previous studies on nanohorn aggregates, but was consistent with studies on SWNTs. Mainly, the adsorption isotherms did not present two sub-steps and the isosteric heat was found to trend through a minimum before increasing at higher coverage values. It was proposed that these contrasting results are attributable to the existence of $CO_2$'s quadrupole moment, as this electrostatic energy contribution decreases the ratio of adsorbate-substrate to adsorbate-adsorbate interaction below that of typical adsorbates (Ne, $CH_4$, etc.).[33, 42] The effective specific surface area for monolayer completion was also calculated using the Point- B and BET methods yielding values of 358 $m^2/g$ and 239 $m^2/g$, respectively. The Point-B value fell in-between previously measured valued for Ne and $CH_4$, indicating the adsorbate can access fewer sites/surface area than Ne but more than $CH_4$.

$CO_2$ adsorption, among other sorbates, was experimentally investigated by Bienfait et al. on cylindrical SWNT bundles.[17] Using the volumetric method and isothermal calorimetry (at 77.4 K), adsorption isotherms and heats of adsorption

were measured. Similar to the previously discussed results on nanohorn aggregates, $CO_2$ trended differently than the other gases ($H_2$, $D_2$, $O_2$, Ar, $CH_4$) in the study. From the adsorption isotherms it was found that $CO_2$ has a fewer number of adsorption sites compared to the other gases, which signifies that the adsorption mechanism is different.[17] After an initial plateau, the isosteric heat for $CO_2$ was found to monotonically increase with coverage. The authors suggest that the initial plateau corresponds to groove adsorption and the overall trend is due to the weak attraction between the carbon bundle and $CO_2$. Similar experimental measurements conducted by the Migone group[20] yielded consistent results; mainly a lack of isotherm steps and an increasing trend in the isosteric heat. Additionally, kinetic measurements performed in the Migone group's study showed that the equilibration time for $CO_2$ increases with loading (and pressure), which contradicts the behavior observed for other gases (Ne, Ar, and $CH_4$) on the same material.

In a recent study by Krungleviciute *et al.* adsorption measurements have been performed for neon and carbon dioxide on open dahlia-like carbon nanohorn aggregates.[33] The opening process allows the sorbates to access the intra-nanohorn pores in the interior region of individual horns. The authors proposed four adsorption sites, two of strong binding (deep in the inter- nanohorn conical pore and the intra-nanohorn pore at the tips of the horns) and two of weak binding (on the outside of the nanohorn surfaces). When they compared the effective surface area obtained on open nanohorns to that on closed there was an increase by a factor of 2.7 for Ne and 2.4 for $CO_2$, which confirms that the opening process allows adsorption to occur in the intra-nanohorn pores. Two steps were observed (before saturation) in the Ne isotherms, corresponding to adsorption in the strong and weak binding sites, while no steps were identified

in the $CO_2$ isotherm data. Similarly to the closed nanohorn investigations by this group, the isosteric heat of Ne was found to be a monotonically decreasing function of coverage with two corresponding plateaus while that of $CO_2$ goes through a minimum before reaching the bulk $CO_2$ latent heat value.[33] Kinetic experiments that measured how long it takes for equilibration to occur were also carried out in this study. For $CO_2$ it was found that the equilibration time increases with increasing loading while the equilibration time for Ne decreases (similar to the behavior of the two gases on carbon nanotube bundles). The authors propose that the contrasting behavior between the two sorbate gases is due to the difference in the ratio of adsorbate–adsorbate and adsorbate-sorbent interactions, as in their earlier studies. In a separate study by Russel *et al*[43], similar kinetic behavior to Ne was observed for Ar and $CF_4$

Several additional studies of adsorption on both carbon nanotube bundles and nanohorn aggregates have been conducted.[14, 18, 44, 45, 46, 47, 19, 48]. The adsorption of ethane on as produced nanohorns was experimentally investigated by Russell et al.[14] Adsorption isotherms were measured for a temperature range between 123.66 K and 221.32 K. In these experiments, distinct isotherm substeps that arise in the adsorption of spherical adsorbates, such as Ne and CF4, were no longer present at similar relative temperatures for ethane adsorption. At lower relative temperatures, a possible single gentle sub-step was observed. This also contrasts the behavior of the same gas on nanotube bundles.[44] Isosteric heat curves show a plateau region at higher coverages, corresponding to the bulk heat of vaporization, while at intermediate coverages (5000 to 23000 cc-Torr/g) a quasi-plateau region region is found with an energy range of between 210 and 250 meV. Kinetic measurements show an increase in equilibra-

tion times, contrasting the observed behavior of ethane on both graphite and closed nanotube bundles.[19] These experimental results leave open questions that warrant further investigation in regards to why the linear adsorbate induces the equilibrium changes as well as why the kinetics are changed by the nanohorn structure.

A computational study by Burde [24] investigated physisorption on nanotube bundles using KMC, where the equilibration times was found to decrease linearly with increasing equilibrium coverage. This behavior is consistent with the majority of gases experimentally measured on carbon nanotube bundles.[49] The rate of decrease was found to be exponentially dependent on the ratio of the model's binding energy to simulation temperature. A later study by the same group[25] investigated physisorption on energetically heterogeneous surfaces. Here it was found that the adsorption rate is increased with the presence of heterogeneity due to indirect adsorption from the weaker sites. Burde *et al.*, also studied the reversal in equilibration time trend that was experimentally observed[19] for some alkanes (propane and larger). The KMC simulations showed that for any system with sufficiently strong gas-gas interactions, the equilibration time can be made to increase with coverage. This, along with the orientational freedom associated with longer hydrocarbons, is used to explain the change in trend for the equilibration time.

# Chapter 2

# Methods and Procedures

Computational simulation methods serve as a bridge between pure theory and experiment. When theoretical models are only analytically tractable for simplistic idealized cases and there is a need for solutions with additional levels of complexity that more closely resemble the real physical system that one desires to model, applying computational methods to the problem is a widely accepted approach. In this respect, numerical simulation complements theory but it can also be used to augment experiment. Accurate computational models can probe physical aspects of systems under conditions that are too difficult or expensive to perform in an actual experimental setting. After being validated, simulations can also be used to help interpret, or make sense of, experimentally obtained results.

In the case of adsorption, atomistic simulations provide direct access to the adsorbed phase configurations. This ability to explicitly view the system is key to matching isotherm and isosteric heat features to corresponding binding site loca-

tions, binding energies, relative site capacities, phase changes, in addition to enabling the identification of kinetic processes at play during equilibration.

The adsorption process begins at the atomic level, with individual adsorbate molecules or atoms spontaneously binding to a particular site (surface, pore, etc.). This bonding can be weak (physisorption) or strong (chemisorption). Regardless of the interaction strength, the most accurate approach would include an explicit treatment of each atom of the system. The modeling of a system at the atomistic level is inherently quantum mechanical in nature and therefore should involve solving the Schrodinger equation. However, this task is only analytically tractable for small hydrogen-like atoms and therefore requires numerical approximation methods. These so called *ab-initio* (or first-principle) methods, are the most accurate and reliable in modeling materials but this comes with a huge computational cost such that only small systems and time scales can be treated due to current constraints (computational and algorithmic limits).

Typically, the first step taken to model larger systems and time scales is to treat the system classically, where one forgoes explicit quantum mechanical effects. As with all approximations, the validity of a classical approach is dependent on the particular system of interest and the underlying phenomena one desires to investigate. With classical simulations, the effect of the individual electrons are encompassed in an interaction potential. This interaction defines the energy and ultimately the forces between the atoms in the system. The potentials are typically empirical in nature and fit to known experimental values or first principle calculations with ad-hoc functional forms that have some basis from quantum theory.

Classical Molecular Dynamics (MD), is the standard deterministic method in which the equations of motions (Newtonian or an equivalent formalism) are numerically integrated yielding the time evolution of the system. While the accuracy trade-off of the classical approximation significantly reduces the underlying computational task resulting in the ability to model larger systems for larger time spans, the limits are still not close to macroscopic sizes ($N_A \sim 6.022 \times 10^{23}\ mol^{-1}$) or time scales (seconds or more) for rare/activated events such as film growth and diffusion that occur in the study of adsorption.

One of the strengths of MD is that the dynamics of the system which include the underlying processes, transitions, events, etc. are automatically produced with no *a priori* knowledge. All of this information is contained in the interatomic potential and the atomistic model of the system. Due to this, there has been a large effort to effectively extend the temporal reach of MD with so-called Accelerated Molecular Dynamics (AMD) methods, which include temperature accelerated dynamics (TAD), hyperdynamics, parallel replica dynamics, and parallel replica splicing [50].

An alternative approach to the above is to take the deterministic problem given by the quantum mechanical or classical approach and recast it in a probabilistic form to be solved by stochastic sampling [51]. This wide class of methods is generally referred to as stochastic methods. Perhaps the most famous of these may be Metropolis Monte Carlo, which gives a general approach to generate a random sampling from a desired probability distribution. In the context of physical simulations, Metropolis Monte Carlo gives a recipe for calculating average properties for various statistical ensembles. As discussed in section 2.3, this is relevant in the study of adsorption within the context of chemical and thermal equilibrium in the grand conical ensemble.

Kinetic Monte Carlo (KMC) is a stochastic method that follows the dynamical evolution of a system. This is accomplished by restricting the evolution to a set of transitions which define the long-time behavior of the system and neglecting the motion between such events. That is, the dynamics are not a direct result of the interatomic potential. For example, in the study of diffusion, hops from one local minimum to another would define the rare transition events and the smaller time-scale vibrations about the equilibrium position are not followed. Traditionally, KMC requires prior knowledge of the transition events, their rates and frequency prefactors, and is carried out on a lattice with restricted interactions, although off-lattice methods or on-the-fly methods have been developed to deal with these limitations [52, 50].

This chapter will outline the basics of the classical computational methods used in this investigation of adsorption on carbon nanostructure materials, which includes Grand Canonical Monte Carlo (GCMC), Kinetic Monte Carlo (KMC), and Molecular Statics (MS). The equations and methods for determining key physical quantities such as isotherms, isosteric heat, equilibration/characteristic times, will be overviewed along with the adsorbent and adsorbate structural and interaction models. The software utilized will be also be presented.

## 2.1 Interaction and Structural Models

In order to study the process of adsorption using computational simulations, both an interaction and structural model is required. Each can be selected to represent either a real naturally occurring system, such as ethane adsorption on carbon nanohorns, or an idealized general system. In the former case, the investigation typ-

ically targets material specific aspects while the latter is more focused on probing fundamental processes and the factors that affect them. In practice, a hybrid approach is commonly used which aims to accomplish both. In any case, the selected aim of the investigation will play a large role in which interaction and structural models are adopted. In addition to this, the simulation method (e.g. GCMC or KMC), regime of interest (e.g. equilibrium or kinetic), energy scale (e.g. physisorption or chemisorption), computational complexity, etc. also contribute to the ultimate model determination.

### 2.1.1 Interactions and Structural Models: Off-lattice

In off-lattice classical simulations atoms are explicitly represented at a continuum of position values. The modeling of adsorption on a carbon nanohorn aggregate or nanotube bundle system begins with an atomistic representation of the sorbate and sorbent as well as with the selection of an appropriate potential for the sorbate-sorbate and sorbent-sorbate interactions. The sorbate structure can closely model the known geometry of a real material, encompass idealized yet representative features of a real material, or focus fundamentally on structural characteristics that may or may not be present in a material. Using a classical isotropic pair potential that neglects many body effects sacrifices accuracy for a reduction in computational workload. In the study of physisorption (i.e. Van der Waals forces or London dispersion forces), which deals with the interaction between instantaneously induced dipoles, the Lennard-Jones (LJ) is an adequate choice of interatomic potentials that is both computationally simple and complex enough to still capture the essential physics of the interaction.[53] With physisorption, The LJ interaction model has been used in nu-

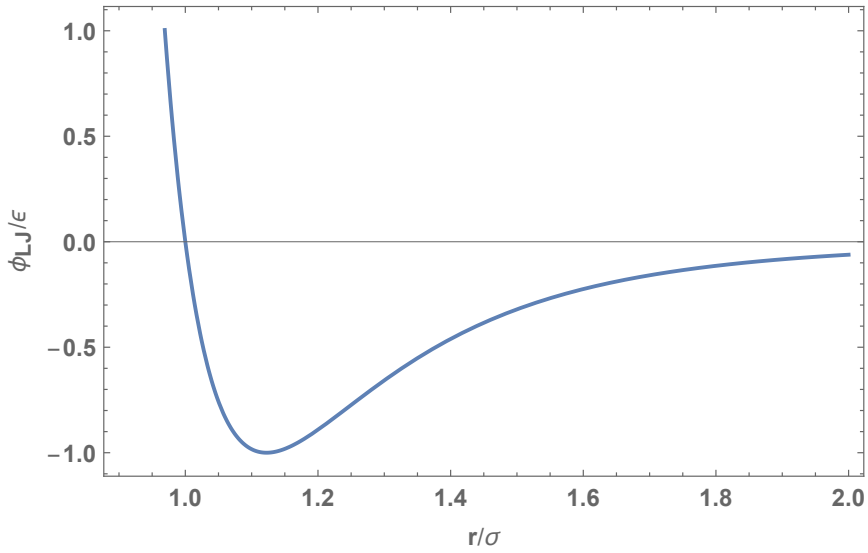


Figure 2.1: The Lennard-Jones (LJ) interatomic potential energy function. The minimum in potential energy occurs at $2^{1/6}\sigma$.

merous computational adsorption studies with reasonable success. The total energy of a system modelled using the Lennard-Jones interatomic potential is given by,

$$U_{total} = \sum_{ij\ pairs} \phi_{LJ}(r_{ij}) = \sum_{ij\ pairs} 4\epsilon_{ij} \left[ \left( \frac{\sigma_{ij}}{r_{ij}} \right)^{12} - \left( \frac{\sigma_{ij}}{r_{ij}} \right)^{6} \right] \tag{2.1}$$

where the summation is over unique pairs of atoms, $\epsilon$ and $\sigma$ are free parameters which serve to set the strength and location of the energy minimum, and $r_{ij}$ is separation distance between atoms $i$ and $j$. As shown in Figure 2.1, this potential energy function is weakly attractive at longer distances, due to the $r^{-6}$ term which represents the dispersion interaction, and strongly repulsive at small distance, due to the $r^{-12}$ term which represents Pauli repulsion. The potential's two parameters are material specific, fit to reproduce bulk properties. For pairs of dissimilar atom types, combination rules need to be used to calculate an effective $\epsilon$ and $\sigma$ value. A popular choice is the

Lorentz–Berthelot combining rules given by,

$$\sigma_{ij} = \frac{\sigma_i + \sigma_j}{2} \qquad \epsilon_{ij} = \sqrt{\epsilon_i \epsilon_j} \tag{2.2}$$

For molecular species with non-zero permanent multipole moments, such as carbon dioxide, an extended charge model will be utilized. With this approach, explicit charges are assigned to the atoms of the molecule (at the Lennard-Jones sites) as well as on so called 'ghost sites' which reside outside of atomic sites. Charge value locations and magnitudes are assigned to reproduce experimentally measured multipole moment values. These electrostatic interactions are calculated using the Coulombic potential for point charges given by,

$$U_{Coul} = \sum_{molecules} k \frac{q_i q_j}{r_{ij}} \tag{2.3}$$

where $k = 9 \times 10^9 Nm^2C^{-2}$ is Coulomb's constant, $q_i$ and $q_j$ are the charge values of the pair of charge sites, $r_{ij}$ is the separation distance between the charge sites, and the summation is over all unique pairs of charge sites occurring between the molecules comprising the system such that pairs of charge sites within the same molecule do not interact with each other.

The carbon $sp^2$ hybridized sorbent materials used in this study have been shown to have a non-zero electric field due do quadrupole moments which are oriented perpendicular to the surface.[54, 55, 56]. As shown in Chapter 3, interactions due to this effect can be neglected as they do not significantly contribute. While induction effects, which arise due to the sorbate and/or the sorbent, can be significant[57, 58], this study adopts the methods of Steele[54] in which the two-body LJ interactions are already

parameterized to include them. The quadrupole interactions utilized in this study include the interaction of a linear quadrupole with a point charge $q$ given by[55],

$$U_{Qq} = k\frac{Qq}{4r^3}(3\cos^2(\alpha) - 1) \tag{2.4}$$

where $Q$ is the quadrupole moment, $r$ is the distance between the point charge and the quadrupole, and $\alpha$ is the is the angle between the quadrupole axis and the vector separating the charge and quadrupole. For the comparison between an extended vs point quadrupole for linear quadrupoles, the interaction energy takes the form of[59],

$$U_{Q_iQ_j} = k\frac{Q_iQ_j}{3r^5}[(3/2)(3\gamma^2 - 1) - 5(9\alpha\beta\gamma - 1) + 5([3\alpha^2 - 1] + [3\beta^2 - 1]) + \frac{35}{4}(3\alpha^2 - 1)(3\beta^2 - 1)] \tag{2.5}$$

where quadrupole moments $Q_i$ and $Q_j$ are specified by unit vectors $\hat{l}_i$ and $\hat{l}_j$ with a separation vector $r\hat{r}$ from $i$ to $j$ where,

$$\alpha = \hat{l}_i \cdot \hat{r} \quad \beta = \hat{l}_j \cdot \hat{r} \quad \gamma = \hat{l}_i \cdot \hat{l}_j \tag{2.6}$$

With the above defined interactions, for a system of $N$ atoms or molecules there are 'N choose 2' ($N(N-1)/2$) unique pairs to consider. This $O(N^2)$ scaling is computationally expensive and can limit the system sizes that can be simulated. One method to reduce the computational task is to reduce the range of the interactions using a cutoff distance, beyond which the interaction pairs are neglected. This approach is only valid when the disregarded interactions are negligible. The feasibility of such an approach can be determined through the calculation of a tail correction fac-

tor, which serves to estimate the error in the potential energy due to the application of a cutoff. The error can be estimated with [60],

$$U_{tail} = 2\pi N\rho \int_{r_{cut}}^{\infty} r^2 u(r) dr \tag{2.7}$$

where is it is assumed that the particle density $\rho$ is constant beyond the cutoff, $N$ is the number of atoms in the system, and $u(r)$ is the potential function used to calculate the energy between a pair of atoms separated by a distance $r$. To ensure that the tail correction energy converges, the potential energy function must decay fast enough to account for the increase in neighboring pairs with increasing $r$. Specifically, for a potential of the form, $u(r) \propto r^{-x}$, $x > 3$ for convergence in 3D. This immediately rules out the Coulombic potential ($\propto r^{-1}$) and explicit dipole-dipole interactions ($\propto r^{-3}$) as those that can utilize an interaction cutoff. For the LJ potential, which scales as $r^{-6}$ at large separation, using a cutoff to truncate the interactions is valid. Furthermore, as shown in 3.1, the extended charge model used to represented the quadrupole-quadrupole interaction for carbon dioxide decays as $r^{-5}$, making the use of a cutoff valid provided that a molecular based cutoff is used such that the interaction occurs between full molecules with a net zero electric charge.

Another method to reduce the computational workload is known as *Coarse-Graining*, where each atom of the system is no longer explicitly represented, rather, groups of atoms are combined together and represented by 'pseudo-atoms'. In this study, both gas molecules and substrate materials will be coarse-grained to simply the interaction calculations and to freeze out unnecessary degrees of freedom. For the carbon sorbent materials studied, such as nanohorns and nanotubes, the coarse-graining

is taken to the extreme where the entire material (comprised of many thousands of carbon atoms) is represented as a continuous and uniform distribution of carbon with an effective atomic surface density. This approximation allows the discrete sum of two-body pair interactions to be replaced with an integral. It is valid when the adsorption occurs far enough away from the surface such that the atomistic surface corrugation effects are small enough to be neglected and when any barriers associated with the atomic structure (such as surface diffusion) are much less than $k_B T$ .

The molecular adsorbate gases investigated in this study are ethane ($C_2H_6$) and carbon dioxide ($CO_2$). The ethane molecule is modelled using a united atom approach in which two methyl group ($CH_3$) pseudo-atoms are rigidly connected with a bond length of 1.54 Å.[61]. Carbon dioxide is modelled as a rigid molecule with three Lennard-Jones (LJ) sites and three point charges centered at each atom. The bond length between the C and O atoms is 1.161 Å.[62] The charge values are set to reproduce the quadrupole moment value of $4.3 \times 10^{-26}$ esu. The LJ potential parameters used are given in Table 2.1, where the unlisted mixed parameters are given by the standard Lorentz-Berthelot combining rules (Eqn. 2.2).

| Species | $\sigma$ (Å) | $\epsilon$ (K) | $Q/e$ |
|---|---|---|---|
| C | 2.785 | 28.999 | 0.6645 |
| O | 3.064 | 82.997 | -0.3323 |
| $CH_3$ | 3.75 | 98 | 0 |
| Ar | 3.405 | 119.8 | 0 |
| C (solid) | 3.4 | 28 | 0 |

Table 2.1: LJ parameters and charges for the pairwise interactions

For the sorbent materials, continuous representations of carbon in the form of planar sheets, cylindrical tubes, paraboloids, and hemispheres are utilized to create structural models for carbon nanostructure materials, as presented in Chapter 3.

For example, carbon nanotube bundles can be modelled as a collection of isolated hexagonally packed cylinders or as a periodic array of cylinders. One representation of carbon nanohorn aggregates is an array of nanotubes with either hemi-spherical or paraboloid caps. The functional form of the interactions for continuous surfaces are given in Appendices A-D in integral form. In the simulations, the gas-sorbent interactions are represented as 1 or 2 dimensional precalculated tables of energy values with a resolution of at least 0.01 Å. This approach pays the upfront cost of numerically solving the required integrals once, in exchange for storing large multidimensional arrays as energy look-up tables during the simulations where bilinear interpolation is used to calculate the energy between adjacent table values.

### 2.1.2 Interactions and Structural Models: On-lattice

In on-lattice simulations atomic positions are discretized. A material is represented as a collection of sites, where the interconnectedness of the sites are explicitly defined. Typically this collection of sites adheres to a regular structure and is referred to as a lattice. As discussed in Section 2.4, rejection-free Kinetic Monte Carlo requires the ability to keep track of all the possible moves for the entire system. This task is most easily accomplished on lattices where all the possible moves are predefined.

A feature of interest in the spherical dahlia-like nanohorn aggregates is the conical pore regions formed between neighboring nanohorns. As depicted in Figure 1.2, these pores have a wide opening towards the exterior of the aggregate which becomes progressively more narrow deeper into the pore. The site binding energy in such a pore increases as the wall separation decreases moving deeper into the pore. Within a lattice based model, one way to represent a conical pore region is to impose a binding

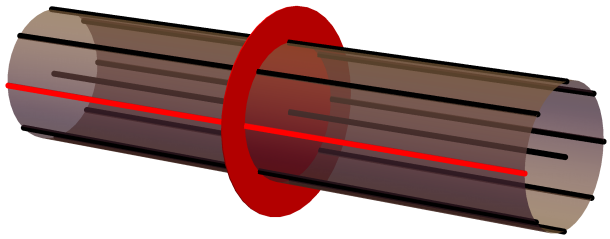

Figure 2.2: The simulation lattice with a highlighted lattice line and layer.

energy gradient along the length of the pore. Here, a 3-dimensional cylindrical lattice of 4500 sites and 500 layers is utilized as depicted in Figure 2.2. A lattice line (defined as a set of sites with common $(x, y)$ coordinates and a lattice layer (defined as a set of sites with common z-coordinates) are shown in red.

Figure 2.3 depicts the connectivity (neighbors) of each lattice site. Each layer is comprised of 9 sites, 8 outer sites (shown in red) and a single center site (blue). Center sites have 8 in-layer neighbors (all outer sites) and an additional 2 out-of-layer neighbors (center sites), which are above and below (the top-most and bottom-most center sites only have one out-of-layer neighbor which is either above or below). The

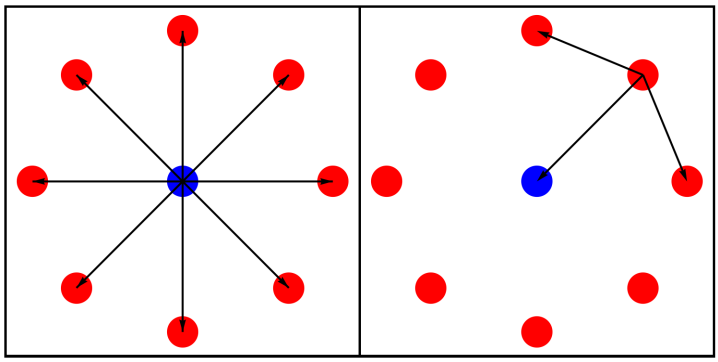

Figure 2.3: In layer lattice site connectivity for center site (left) and outer site (right).

red outer sites have 3 in-layer neighbors (two adjacent outer sides and the in-layer center site) and an additional 2 out-of-layer neighbors (outer sites), which are above and below. Outer sites in the topmost and bottom-most layer only have 1 out-of-layer neighbor above or below.

Monomer gaseous species are modelled through the occupation of single sites. This method is valid for noble gases (Ar, Ne, etc.) as well as spherically symmetric gases such as methane ($CH_4$). As monomers only have a single orientation with respect to the sorbent material, adsorption/desorption and diffusion events are easily represented by a change in occupancy of single sites. This also allows for single energy values to represent binding and interaction energies, respectively. The system energy is given as the sum over occupied sites $i$,

$$E_{total} = \sum_i E_i \tag{2.8}$$

where occupied sites have energies $E_i$,

$$E_i = \epsilon_{b_i} + \epsilon_{s_i} + \frac{1}{2} \sum_{j,NN} \delta_{ij} \epsilon_{int_{ij}} \tag{2.9}$$

here $\epsilon_{b_i}$ is the binding energy associated with the lattice site type, $\epsilon_{s_i}$ is the energy associated with the gas species, $\epsilon_{int_{ij}}$ is the interaction energy between sites $i$ and $j$, $\delta_{ij}$ takes the value of 1 for occupied neighboring sites and is 0 otherwise, and the factor of 1/2 accounts for the double counting which occurs for each interaction.

Interactions for on-lattice simulations are typically represented with position independent constant energy values as given above in Eqn. 2.9, due to the fixed distances associated with a rigid lattice. When modeling real materials the well depth associ-

ated with the LJ (or similar) interaction is used at the equilibrium position as shown above in Figure 2.1. It is convenient to use a dimensionless energy value,

$$\epsilon = \frac{E}{k_B T} \tag{2.10}$$

such that equivalent combinations of energies and temperatures are captured in a single simulation.

As presented in Chapter 4, the above defined lattice will be utilized with variations of binding energies for a monomer gas species. The impact of introducing a position dependent energy gradient along the length of the pore will also be investigated. For these simulations, adsorption/desorption events will be confined to one or both ends on the cylindrical pore.

## 2.2 Molecular Statics

Classically modeled systems are described by a position dependent interatomic potential energy function which describes the physics of the atomic interactions. The minima of this high dimensional ($3N$ atomic coordinates) function are of great interest as they correspond to the stable equilibrium configurations which are physically realizable stable states of the system. For the case of adsorption, minimum energy sites correspond to the most probable binding sites at low pressures.

Analytically determining the stationary points of the energy function by finding the configurations (set of atomic coordinates describing the system) that satisfy $\nabla V(\vec{r_1}, ..., \vec{r_N}) = 0$ is not feasible for systems with realistic $3N$ dimensional potential energy functions. Several numerical approaches to this geometric optimization

problem exist which iteratively perturb the atomic coordinates of the system from a starting configuration until a minimum in the potential energy is located. The methods differ in how they determine the direction and distance that each atom's position is altered during every iteration. A convergence criterion, which determines when a minimum is located, is checked at each step and signals the termination of the minimization routine when satisfied.

At a minimum of the potential energy the net force on each atom is zero and a small deviation of the configuration should result in a correspondingly small change in the potential energy. This gives two criteria that can be used to determine if a minimum is reached,

$$|\vec{F}_i| < F_{tolerance} \qquad |V_i - V_{i-1}| < E_{tolerance} \tag{2.11}$$

where $\vec{F}_i$ is the global force vector for the system configuration of the ith iteration, $V_i$ is the potential energy of the system configuration of the ith iteration, and the energy and force tolerance values are chosen to be small enough to ensure convergence while at the same time large enough to minimize the number of required iterations.

A reasonable choice for varying the system coordinates in the search for a minimum is to move each atom in the direction of the net force acting on it, which corresponds to the direction of greatest decrease of the potential energy function $F = -\nabla V$. The *Steepest Descent* minimization algorithm follows this approach for determining the direction to move the atoms of the system during minimization. The size of the displacement steps is either defined as a small constant to ensure that a step does not increase the total energy or it is determined through a series of one dimensional

line searches. In these line searches, the length of the step size that each atom moves in the direction of its local force is chosen to minimize the energy for that particular direction. The system trajectory produced through the application of the Steepest Descent algorithm is physical and corresponds to over-damped or highly quenched dynamics, with motion continually in the direction of the net force. Many other more sophisticated yet related methods exist, such as Conjugate Gradient (CG) and Newton-Raphson (NR), which utilize more advanced search direction and step size routines in an effort to decrease the number of iterations necessary to find an energy minimum.

The Steepest Decent, and other related algorithms, are local optimization methods, since the minimum of potential energy that they ultimately find is dependent on the initial configuration of the system. That is, they are not guaranteed to find the absolute minimum of the potential energy function. For cases when this is a necessity, global optimization methods can be employed to locate the true or absolute energy minimum of the system. Many such methods exist which span an extensive and very active area of research. In this investigation the heuristic method of simulated annealing will be employed when needed, where molecular dynamics simulations are carried out to heat up the system and then slowly cool the system [63]. The basic idea is to exploit higher temperatures to allow the system to evolve over the energy barriers of the local minima and reach the global minimum configuration.

In the study of gas adsorption, especially on surfaces, it is commonplace to utilize energy minimization methods to generate *Potential Energy Surfaces* (PES) which describe the energy of the system as a function of the position of a single gas atom/molecule. These can be used to determine the location of adsorption sites as

well as transition pathways between stable states. Figure 2.4 shows a PES calculated

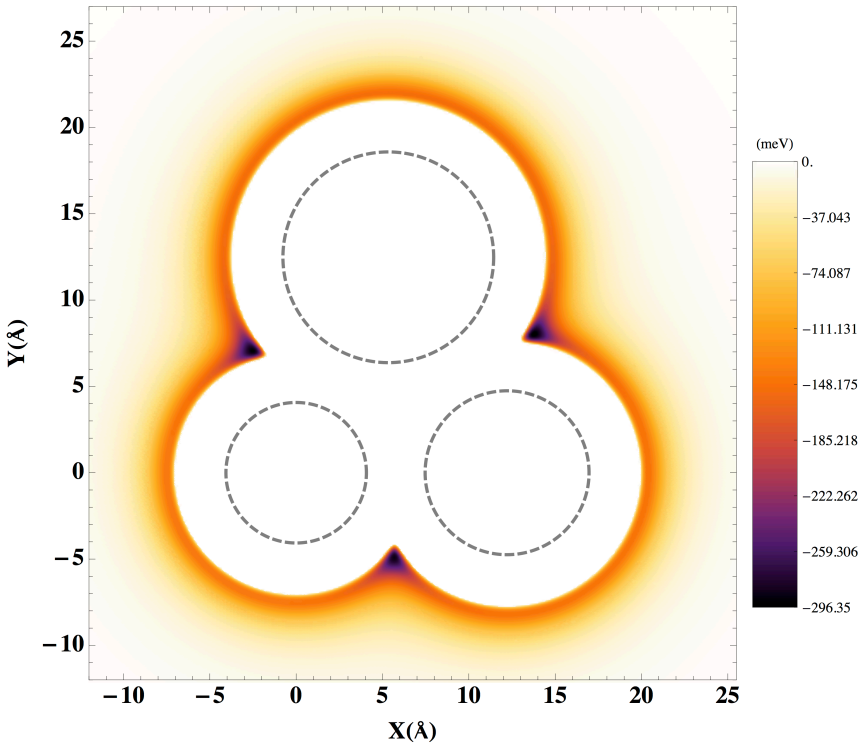


Figure 2.4: Potential Energy Surface for Ethane on a 3 tube heterogeneous closed nanotube bundle as viewed along the symmetry length axis. The gray dashed circles denote the external surface of the tubes.

for ethane ($C_2H_6$) on a heterogeneous bundle of closed carbon nanotubes. Here the energy is plotted in the plane perpendicular to the symmetry axis along the length of the nanotubes. Darker colors represent regions of stronger binding (lower energy values). In this case, there are two distinct adsorption sites: 1) In the groove region between adjacent tubes and 2) On the individual external surfaces of the tubes. This PES for an ethane molecule, $V_{min}(x, y)$ , was obtained by minimizing the potential energy $V(x, y, z, \vec{R}_n)$ with respect to the orientation of the molecule for various values

of $(x, y)$,

$$V_{min}(x, y) = min \left[ V(x, y, z, \vec{R_n}) \right]_{z, \vec{R_n}} \tag{2.12}$$

where $x$, $y$, and $z$ are the coordinates for the center of mass of $C_2H_6$ and $\vec{R_n}$ denotes the $3N$ coordinates of the atoms comprising the nanotube bundle. To find $V_{min}(x, y)$ for a specific point, $C_2H_6$ is placed at the $(x, y)$ location and the orientation of the molecule is permitted to relax to minimize the energy. In this case, $z$ (symmetry axis) and $\vec{R_n}$ are also held fixed at each $(x, y)$ point.

As mentioned, the PES can be used to find minimum energy pathways (transitions) between configurations. For example inspection of Figure 2.4 shows a barrierless transition from the external sites of the nanotubes to the groove sites, as the energy is shown to be monotonically decreasing along that path. Another, more robust method for calculating minimum energy pathways between stable configuration is the *Nudged Elastic Band* (NEB) method[64, 65]. NEB takes as input the initial and final configurations corresponding to a transition. A series of system replicas connecting these two states is generated where each atom is connected to its own image in adjacent replicas. This connection is described by an inter-replica spring force which acts parallel to the transition path. This can be useful in the determination of barriers and energy differences between states for the calculation of rate constants for use in Kinetic Monte Carlo simulations.

## 2.3 Grand Canonical Monte Carlo (GCMC)

A natural choice for the study of adsorption is the grand canonical ensemble $(\mu, V, T)$ which allows for both fluctuations in energy and the number of particles

through contact with a energy and particle reservoir. In this ensemble, which fixes the chemical potential, volume, and temperature, a system immersed or in contact with the reservoir will exchange both particles and energy until equilibrium is reached where both the chemical potential and temperature are equal to that of the reservoir.

Using Markov Chain Monte Carlo (MCMC) simulations with importance sampling, the main idea is to construct a random walk through configuration space that samples from a chosen statistical ensemble in order to calculate average values of quantities of interest. An example for the case of sampling from the grand canonical ensemble in the context of studying adsorption is the average number of molecules adsorbed to the surface of a material at equilibrium for a given chemical potential and temperature. Adsorption isotherm curves which give the coverage as a function of chemical potential for a given temperature can be generated by combining the average results from multiple independent samplings of grand canonical ensembles that differ only in chemical potential. For comparison with experiment, the chemical potential can be related to pressure through the ideal gas assumption or other equation of state expression. In this study, it is assumed that the gas/particle reservoir is sufficiently dilute such that excess coverage effects are negligible and $\mu$ is simply related to the reservoir pressure and temperature through the relation for the chemical potential of an ideal gas (fugacity coefficient = 1). This assumption is justified in GCMC simulations conducted in Chapter 3, where the contribution due to excess coverage is calculated.

The Metropolis Monte Carlo algorithm provides a general process for sampling from a chosen statistical distribution to calculate averages without explicit evaluation of the corresponding partition function. For the case of a rigid carbon nanostructure

material immersed in a heat bath and particle reservoir the partition function is given by, [60]

$$Z(\mu, V, T) = \sum_N \frac{\exp(\beta\mu N)V^N}{\Lambda^{3N}N!} \int_\Omega \exp(-\beta U(\vec{x}^N))d\vec{x}^N \tag{2.13}$$

where $\vec{x}^N$ is a 3N dimensional vector denoting the configurational state of the system, $U$ is the potential energy function, $\Lambda$ is thermal de Broglie wavelength, and $N$ is the number of gas molecules/atoms. The probability density for finding the system in the state $(\vec{x}^N, N)$ is proportional to, [60]

$$p(\vec{x}^N, N) \propto \frac{\exp(\beta\mu N)V^N}{\Lambda^{3N}N!} \exp(-\beta U(\vec{x}^N)) \tag{2.14}$$

The average value of the general observable $\mathcal{O}$ is then given by:

$$\langle \mathcal{O} \rangle = Z^{-1} \sum_N \int_\Omega \mathcal{O}(\vec{x}^N)p(\vec{x}^N, N)d\vec{x}^N \tag{2.15}$$

The average value given in Eqn. 2.15 can be numerically approximated by evaluating $\mathcal{O}$ and $p$ for $n$ selected configurations $\vec{x}_i^N$. If the configurations are selected according to a generic probability distribution $\rho$, the approximate average value takes the form of,

$$\langle \mathcal{O} \rangle \approx \sum_i^n \mathcal{O}(\vec{x}_i^N)\rho(\vec{x}_i^N)^{-1}p(\vec{x}_i^N, N) \Big/ \sum_i^n \rho(\vec{x}_i^N)^{-1}p(\vec{x}_i^N, N) \tag{2.16}$$

If the sampled configurations are chosen according to an optimal distribution, the number of required function evaluations needed to obtain an accurate value can be minimized along with the variance. *Importance Sampling* encompasses this idea of using a distribution where the integrand in Eqn. 2.15 is dominate. With this in mind,

a common choice is to use the probably density of the underlying statistical ensemble (here Eqn. 2.14). Using this probability distribution to choose states, the calculation of the average value simplifies to,

$$\langle \mathcal{O} \rangle \approx= \frac{1}{n} \sum_{i}^{n} \mathcal{O}(\vec{x}_i^N) \tag{2.17}$$

In order to generate random configuration states according to the underlying probability density (Eqn. 2.14) the Metropolis algorithm uses the concept of a Markov Chain, where an initial configuration is iteratively updated according to specific transition probabilities. The chain is evolved under the "no history" assumption, where the proposed transition only depends on the current state of the system. Through the repeated application of the transition rules, it is guaranteed that the chain will ultimately converge to the target distribution (Eqn. 2.14), provided it is irreducible and aperiodic[66].

In the Grand Canonical Monte Carlo Markov Chain, four transitions can occur:

1. **Displacement**: The center of mass of a randomly selected gas molecule/atom is randomly displaced within a cube centered about its initial position. A maximum displacement value is defined to limit the move.

2. **Rotation:** The orientation of a randomly selected gas molecule is perturbed such that the center of mass does not move. A maximum rotational displacement angle is defined to limit the move.

3. **Insertion:** A new molecule/atom is inserted into the system at a random location in the simulation cell.

4. **Deletion:** A randomly selected molecule/atom is removed from the simulation cell.

With GCMC, the transitions can be carried out both on a lattice with a discrete number of states or a continuous system.

Imposing the *detailed balance* condition, which is a sufficient but not necessary condition, ensures that the chain converges to the unique stationary distribution.[60] If we collapse the notation representing the state of a system which is uniquely defined by the number of atoms and their associated degrees of freedom as $(\vec{x}^N, N) \rightarrow (\vec{x}^N)$, the detailed balance condition takes the form of,

$$p(\vec{x}^N)\pi(\vec{x}^N \rightarrow \vec{x}^{N'}) = p(\vec{x}^{N'})\pi(\vec{x}^{N'} \rightarrow \vec{x}^N) \tag{2.18}$$

where the prime denotes a different state which could be comprised of a change in the number of atoms in the system (as shown with $\vec{x}^{N'}$), a change of the atomic configurations ($\vec{x'}^N$), or both ($\vec{x'}^{N'}$). Here we focus on a change in the number of atoms only for notational ease, but note that other changes can be equivalently handled without loss of generality. $\pi(\vec{x}^N \rightarrow \vec{x}^{N'})$ denotes the probability of the system for transitioning from the state defined by $\vec{x}^N$ to the state defined by $\vec{x}^{N'}$. This condition describes the flow of probability between different states of a system, which in equilibrium should not destroy the distribution being sampled from.

The transition probability given by $\pi$ can be decomposed into the product of two components, one for the probability of generating or proposing a particular state, $\alpha$,

and the other the probability of accepting the proposed state, $A$,

$$\pi(\vec{x}^N \rightarrow \vec{x}^{N'}) = \alpha(\vec{x}^N \rightarrow \vec{x}^{N'})A(\vec{x}^N \rightarrow \vec{x}^{N'}) \tag{2.19}$$

With knowledge of the desired distribution that one wants to sample from (Eqn. 2.14) and the detailed balance condition, a relation for the move acceptance probability can be found,

$$\frac{A(\vec{x}^N \rightarrow \vec{x}^{N'})}{A(\vec{x}^{N'} \rightarrow \vec{x}^N)} = \frac{p(\vec{x}^{N'})}{p(\vec{x}^N)} \frac{\alpha(\vec{x}^{N'} \rightarrow \vec{x}^N)}{\alpha(\vec{x}^N \rightarrow \vec{x}^{N'})} \tag{2.20}$$

There exists many possible valid selections for an acceptance probability that satisfies Eqn. 2.20. In the Metropolis-Hastings algorithm, the choice is given by,[60]

$$A(\vec{x}^N \rightarrow \vec{x}^{N'}) = min\left(1, \frac{p(\vec{x}^{N'})}{p(\vec{x}^N)} \frac{\alpha(\vec{x}^{N'} \rightarrow \vec{x}^N)}{\alpha(\vec{x}^N \rightarrow \vec{x}^{N'})}\right) \tag{2.21}$$

With the original Metropolis algorithm, the proposal distribution was chosen to be symmetric, $\alpha(\vec{x}^N \rightarrow \vec{x}^{N'}) = \alpha(\vec{x}^{N'} \rightarrow \vec{x}^N)$. However, the use of a non-symmetric state generation distribution is perfectly valid and is useful for biasing methods, such as *Configurational-Bias*. These schemes attempt to increase the acceptance of moves to more fully sample the configurational space and therefore reduce the number of moves (and simulation time) required to reach the target stationary distribution. It is also worth noting that Eqn. 2.21 contains a ratio of the ensemble probability density, $p$. Due to this the partition function drops out of the calculation, as after-all this Monte Carlo simulation scheme would not be necessary if the partition function was within the grasp of current computational limits.

For the grand canonical ensemble with a symmetric proposal distribution the move acceptance probabilities are given by:

1. **Insertion:**

$$A(\vec{x}^N \to \vec{x}^{(N+1)}) = min\left(1, \frac{V}{\Lambda^3(N+1)} e^{\beta\mu} e^{-\beta(U(\vec{x}^{N+1})-U(\vec{x}^N))}\right) \tag{2.22}$$

2. **Deletion:**

$$A(\vec{x}^N \to \vec{x}^{(N-1)}) = min\left(1, \frac{\Lambda^3 N}{V} e^{-\beta\mu} e^{-\beta(U(\vec{x}^{N-1})-U(\vec{x}^N))}\right) \tag{2.23}$$

3. **Displacement/Rotation:**

$$A(\vec{x}^N \to \vec{x'}^N) = min\left(1, e^{-\beta(U(\vec{x'}^N)-U(\vec{x}^N))}\right) \tag{2.24}$$

With the acceptance rules aptly defined, Algorithm 1 given below will allow for the sampling from a $\mu VT$ ensemble. There are several practical details absent from the given algorithm that warrant further discussion. A properly constructed Markov chain evolved as prescribed is guaranteed to converge to the stationary distribution from any valid initial state and any average observable can be determined to a specified accuracy in the limit that the number of performed transition approaches infinity. In practice, an infinite chain is impossible to simulate. From this, some questions naturally arise such as: How quickly does the chain converge? How many observations are required for an accurate observable estimate? How to deal with correlated samples? What can be done to increase the rate of convergence?

A general statement regarding the convergence to equilibrium is not possible.[66] In this study the above questions were approached heuristically. Simulations at each state point $(\mu, V, T)$ were performed multiple times with differing initial states, random seeds, system sizes, and chain lengths (number of transition moves) to ensure consistency. Quantities of interest such as the system energy and number of adsorbed molecules are monitored during the evolution of the simulations. Once these quantities are detected to be no longer changing on average (and fluctuations within ensemble limits), sampling occurs at regular intervals (every $n$ moves) to store the state of the system (including full configurational information). Data stored during the burn-in phase is discarded and not used for the calculation of average values.

Algorithm 1: Grand Canonical Monte Carlo (GCMC)

1. Configure the system in a suitable initial state
2. Randomly select a valid transition type from the list of allowed moves (Displacement, Rotation, Insertion, Deletion)
3. Carry out the selected move and calculate the associated change in energy.
4. Accept or reject the move based on the acceptance rules defined in Eqns. 2.22-2.24. For rejected moves, return the system to the state prior to Step 3.
5. Repeat Steps 2-4. Begin regularly sampling quantities of interest once the stationary distribution is reached.

Block averaging[51] is employed in a post processing step to estimate the correlation length, $s$ for each quantity of interest. Final averages are then determined using values

separated by at least $sn$ moves. In this study typical burn-in and equilibrium sampling phases range from 10's of millions to billions of Monte Carlo moves.

While detailed balance and the choice of a symmetric proposal distribution requires that the probably of proposing an insertion (adsorption) and deletion (desorption) must be equal ($\alpha_i = \alpha_d$), there are no constraints on the relation between the proposals for insertion/deletion and displacement/rotation. This freedom allows the moves in step 2 of Algorithm 1 to be selected with different probabilities, which can impact the rate of convergence.[51] A popular choice is selecting an insertion or deletion move 60% of the time and a displacement or rotation move 40% of the time, although it is not clear that this is an optimal choice.[51]

For displacement and rotational moves, a molecule is selected and either its center of mass is displaced randomly within a local sphere or rectangle with characteristic size $\delta$ or its orientation is perturbed within a maximum angular displacement of $\theta$. There is freedom in the choice of values for $\delta$ and $\theta$. Typically, large values will result in a high energy configurations and thus have a low acceptance probability. Smaller values are usually associated with lower changes in energy. While these configurations are more likely to be accepted, they come with the drawback that the configuration is only minimally changed which can increase the number of moves required to reach convergence. In practice, a value of $\delta$ and $\theta$ that corresponds to an average move acceptance of 50% is used. In this study, the maximum rotation and displacement steps were dynamically adjusted during the equilibration phase of the simulation to achieve a move acceptance value of 50%.

Monte Carlo simulations in the grand canonical ensemble can have difficulties obtaining sufficient sampling of configuration space for high density phases. This is due

to the low acceptance rate associated with insertion and deletion moves. At high system densities insertions are likely to result in near overlapping which is associated with high energy changes and therefore low acceptance probabilities. Deletion moves, which remove molecules without allowing relaxation around the removal site are similarly plagued with low acceptance rates. Various biasing methods exist with the aim of increasing the rate of move acceptance[51, 60]. This is accomplished by altering the proposal distribution, $\alpha$, to prefer (bias) trying moves which are more likely to be accepted. One method utilized in this study is energy biasing[67], which places a higher weight for attempting insertion moves in regions with lower potential energy (stronger binding). For this, the simulation cell is divided into small cubic cells of volume $v_i$ with an associated weight given by,

$$\omega_i = e^{-\beta U_i} \Big/ \sum_j e^{-\beta U_j} \tag{2.25}$$

where the potential energy associated with each cell, $U_i$, is calculated by placing a molecule at the center of the cell and averaging over a number of random orientations. Under energy biasing, insertion moves are then carried out by selecting a cubic cell according to the precalculated weight $\omega_i$ and placing a molecule in a random position and orientation in the cell. Deletion, displacement, and rotation moves still uniformly select a random molecule, however the insertion and deletion acceptance probabilities both require modification in order to maintain the detailed balance condition,

1. **Insertion:**

$$A(\vec{x}^N \rightarrow \vec{x}^{(N+1)}) = min\left(1, \frac{V_i}{\omega_i V} \frac{V}{\Lambda^3 (N+1)} e^{\beta\mu} e^{-\beta(U(\vec{x}^{N+1}) - U(\vec{x}^N))}\right) \tag{2.26}$$

2. **Deletion:**

$$A(\vec{x}^N \rightarrow \vec{x}^{(N-1)}) = min\left(1, \frac{V\omega_i}{V_i}\frac{\Lambda^3 N}{V}e^{-\beta\mu}e^{-\beta(U(\vec{x}^{N-1})-U(\vec{x}^N))}\right) \tag{2.27}$$

When the system potential energy surface is rugged with many local minima, Monte Carlo methods can fail to adequately sample the configuration space. In these cases, other biasing methods exist such as *Parallel Tempering*[60] which aim to "knock" the system out of a local minimum to increase sampling diversity in a manner similar to simulated annealing.

A successful GCMC simulation will yield the equilibrium number of adsorbed molecules in the simulation cell for the given temperature, volume, and chemical potential. The adsorbate material, represented by an interatomic potential, along with the molecular interactions play the critical role in determining the ultimate coverage amount, structure, location, etc. From the simulation data, adsorption/desorption isotherms can be obtained, which relate the equilibrium sorbate surface coverage to the pressure (or chemical potential) of the gas phase that the system is immersed in. Isotherm curves are generated by combining multiple independent GCMC simulation at fixed temperatures and volumes, but variable pressures (chemical potential). Through further analysis the isosteric heat of adsorption, defined as the energy released upon molecular adsorption at fixed loading, can be determined for a direct comparison with experiment. This quantity provides insights into the interaction strengths. The calculation of the isosteric heat is given by numeric differentiation of

the average potential energy,

$$q_{st} = k_B T - \left( \frac{\partial \langle U \rangle}{\partial \langle N \rangle} \right)_{T,V} \tag{2.28}$$

As discussed by Bakaev and Steele[68], the isosteric heat calculation can be used as a self consistency check of the GCMC code. This is accomplished by calculating the isosteric heat multiple different ways, and ensuring the results are in agreement. The isosteric heat can be determined from the isotherms using,

$$q_{st} = k_B T^2 \left( \frac{\partial \ln P}{\partial T} \right)_N \tag{2.29}$$

as well as with the fluctuations in energy and particle number,

$$q_{st} = k_B T - \left( \frac{\langle UN \rangle - \langle U \rangle \langle N \rangle}{\langle N^2 \rangle - \langle N \rangle^2} \right) \tag{2.30}$$

The coverage values obtained from GCMC calculations are absolute, which means that they include the number of molecules that would normally be present in the volume accessible to the adsorbate in the bulk phase without the presence of the sorbent. Experimentally measured coverage values do not include this extra coverage and therefore a conversion is required. In practice, this conversion is only necessary at higher pressures when the bulk contribution is significantly large. The excess coverage amount, $N_e$, can be estimated using the method of Palmer *et al.*[69] where the accessible volume, $V_g$ is found by considering the interaction potential of a helium atom with the sorbent,

$$N_e = N - \rho_g V_g \tag{2.31}$$

where $N$ is the absolute coverage and $\rho_g$ is the density obtained from the appropriate equation of state (usually assumed as ideal) for the gas of interest. The accessible volume is found using,

$$V_g = \int_{V_{cell}} \exp[-U_{He}(\vec{r})/k_B T]\, d^3r \tag{2.32}$$

where $U_{He}$ represents the He-adsorbent interaction and the integration is performed over the volume of the simulation cell, $V_{cell}$. In practice, an upper bound on $V_g$ can be found using,

$$V_g = V_{cell} - V_{adsorbent} \tag{2.33}$$

In many cases, such as the cylindrical nanotubes, the volume occupied by the adsorbent material, $V_{adsorbent}$, can be easily calculated using known analytic forms.

Along with the coverage and energy information, the configurations (atomic coordinates) of the molecules comprising the adsorbed phase are recorded at regular intervals throughout each of the simulations. The ability to explicitly view the position and orientation of the molecules is paramount to understanding where binding occurs, the adsorbed phase structure, and (as shown in Chapter 3) experimental isotherm and isosteric heat curve features.

## 2.4 Kinetic Monte Carlo (KMC)

The probabilistic time evolution of a system with explicitly defined states and transitions is governed by a *Master equation*,

$$\frac{\partial p(\vec{x_i}, t)}{\partial t} = \sum_j [W(\vec{x_j} \rightarrow \vec{x_i}) p(\vec{x_j}, t) - W(\vec{x_i} \rightarrow \vec{x_j}) p(\vec{x_i}, t)] \tag{2.34}$$

where $p(\vec{x_i}, t)$ is the probability that the system is in state $i$ at time $t$ and $W(\vec{x_j} \rightarrow \vec{x_i})$ is the probability per unit time for transitioning from state $\vec{x_j}$ to state $\vec{x_i}$. This master equation can be interpreted as a rate or balance equation, where the first term denotes the gain (transitions into the current state) and the second term represents the loss (transitions out of the current state). The full solution, which comprises solving a coupled set of equations similar to Eqn. 2.34 for each state, gives a probabilistic description of the system that can be used to determine the average dynamics of the system, *inter alia*.

For systems with a large number of states and transitions, an exact analytical approach to solving the Master equation is unfeasible. A numerical approach, known by many names such as Kinetic Monte Carlo, N-fold way, BKL algorithm, residence-time algorithm, Gillespie algorithm, Direct Method, Variable Step Size Method, dynamical Monte Carlo, etc.[70, 71, 52], utilizes Markov Chains (similar to equilibrium Monte Carlo methods) to evolve the system from one state to another by generating stochastic trajectories according to transition probabilities (rates) and their associated times. By averaging over a sufficiently large number of such trajectories, the time dependent probability of state occupancy can be obtained. Furthermore, if all possible transi-

tions are properly and accurately included, the state to state trajectory is identical to that of a similarly averaged molecular dynamics simulation.[52]

There have been many approaches [70, 71, 52] for developing an algorithm that generates trajectories (sets of successive states) that have probabilities and escape times in accordance with the Master equation. These can be generally classified as *rejection* or *rejection-free* methods. With rejection Monte Carlo, the same methodology that is used in the equilibrium approach discussed in Section 2.3 is again employed to select and accept a random transition/event based on a probability consistent with the rate for the selected transition ($W(\vec{x_i} \rightarrow \vec{x_j})$). Just as with equilibrium Monte Carlo, this approach is plagued with the same inefficiencies that arise when acceptance probabilities are low. With rejection-free Monte Carlo, a transition or event occurs each step without the possibility of rejection. This increased move efficiency comes at the cost of having to calculate and keep track of all the possible transitions for the entire system in order for the selection process to occur with the appropriate probability. The rejection-free approach therefore has much larger memory requirements and requires additional computation each step. Furthermore, the requirement of knowing the rate constants or transition probabilities for all possible events in the system is usually handled by restricting the system to a discrete lattice, although off-lattice and/or on-the-fly rejection are an active area of investigation[70].

For the study of gas adsorption on carbon nanostructure materials, where the goal is to analyze the fundamental variables that impact equilibration times, the lattice rejection-free kinetic Monte Carlo method will be utilized. Assuming that the possible transitions or system events are Markovian (depend only on the initial and final states) and behave as a Poisson process such that events occur at a known

average rate and are independent of the time since last occurrence, it has been shown [70, 71, 52] that the probability distribution/density for the time of first escape from the present state (time between successive events) is given by,

$$p_{escape}(t) = k_{tot} e^{-k_{tot} t} \tag{2.35}$$

where,

$$k_{tot} = \sum_{j} W(\vec{x_i} \rightarrow \vec{x_j}) \tag{2.36}$$

This probability of transitioning out of a state can then be used to calculate the average time of escape,

$$\langle t_{escape} \rangle = \int_0^\infty t \; p_{escape}(t) dt = 1/k_{tot} \tag{2.37}$$

Given the stochastic nature of the process and the underlying Poisson distribution (Eqn. 2.35), a consistent definition for the individual escape time takes the form of,[70, 71, 52]

$$t_{escape} = -\frac{\ln(R)}{k_{tot}} \tag{2.38}$$

where $R$ is a uniform randomly generated number between 0 and 1. As the average value of $\ln(R) = -1$, this definition is consistent with average escape time given in Eqn. 2.37.

With the above definitions and concepts in place, a stochastic algorithm to evolve a system from state to state in a manner consistent with a solution to the Master equation can now be presented, assuming all of the transition probabilities or rate constants are known. A naive but perfectly valid approach would be to first calculate

the escape times (Eqn. 2.38) for every possible transition out of the current state.[52] From there, move the system to the state that corresponds to the pathway with the smallest escape time and repeat this process iteratively. This method, known as the *first reaction method* is inefficient since it requires a random number to be generated for each pathway and not well suited for systems with dissimilar rate constants.

A more efficient and widely accepted method, known as *N-Fold way*, *the BKL algorithm*, or *the Gillespie algorithm*, only requires two uniformly drawn random numbers to evolve the system from state to state. Algorithm 2 below describes the procedure for carrying out this type of Monte Carlo simulation. One method of selecting an event or pathway with a probability proportional to the rate constant (for Step 5) is to find the smallest $m$ that satisfies the inequality,

$$Rk_{tot} < \sum_{j}^{m} W_{ij} \tag{2.39}$$

where $R$ is a uniform random number $(0, 1]$. The event corresponding to the value

Algorithm 2: Rejection-Free Kinetic Monte Carlo (rf-KMC)

1. Configure the system in a suitable initial state
2. Create a list of all possible pathways/events for the to move out of the current state.
3. Calculate the rate constant (transition probability) for each possible event in Step 2.
4. Calculate the total rate constant by summing the rates in Step 3 (Eqn. 2.36).
5. Select an event to execute based on the weighted probability of the rates given by Step 3.
6. Execute the selected event in Step 5. Increase the simulation time as given in Eqn. 2.38.
7. Repeat Steps 2-6. Sample quantities of interest and store system configurations.

of $m$ found through Eqn.2.39 is then executed. This method is analogous to first vertically stacking blocks with heights proportional to the individual rate constants ($W_{ij}$). Eqn. 2.39 then randomly selects a position along that vertical stack. Since the height of each block is proportional to the corresponding rate constant, the events are then selected with the correct probability. The computational work required for this method scales as $O(N)$, where $N$ is the number of events/pathways. There are other more efficient methods for event selection, such as the binary tree $O(logN)$ and group $O(1)$ methods.[72]

The KMC algorithm will generate a time dependent state to state trajectory which must be ensemble averaged to produce the time dependent probability of state occupancy. This is typically accomplished by simultaneously running identical simulations that differ only by their initial random seed number. Results from each simulation are then averaged together at equivalent time values to produce the final trajectory which can be used to calculate kinetic properties such as the rate of gas adsorption, equilibration time, etc.

As previously alluded to, the critical piece of input to the KMC algorithm is the underlying rate constants or transition probabilities for each of the elementary processes that one wishes to include in the model. Unknowingly neglecting a reaction pathway or using an unphysical or inaccurate rate constant can serve to nullify the validity of the simulations. Studies which aim to produce accurate results for a specific material and/or gas of interest typically attempt to use rate constants that are calculated from *Transition State Theory* (TST). Other studies, such as this present investigation, which are more motivated in eliciting the fundamentals or probing how the general kinetic features are impacted by changing variables that the rate constant depends on (energetics, degrees of freedom, lattice configuration, pathways, etc.), typically forgo an exact treatment of the rate constants in favor of capturing the general trends. This flexibility in the explicit form of the rate constants is similar to the acceptance probability defined in equilibrium Monte Carlo. Here, the steady state regime ($\frac{\partial p(\vec{x_i},t)}{\partial t} = 0$) of the master equation imposes a constraint that the rate constants must adhere to,

$$0 = \sum_j [W(\vec{x_j} \rightarrow \vec{x_i})p(\vec{x_j}) - W(\vec{x_i} \rightarrow \vec{x_j})p(\vec{x_i})] \tag{2.40}$$

which simply states that all transitions out of a particular state must be exactly balanced by the transitions into the state. In equilibrium, the condition of detailed balance imposes a more strict condition that each process must be exactly balanced by a reverse process,

$$W(\vec{x_j} \rightarrow \vec{x_i})p(\vec{x_j}) = W(\vec{x_i} \rightarrow \vec{x_j})p(\vec{x_i}) \tag{2.41}$$

which is equivalent to Eqn. 2.18, differing only in notation. The equilibrium distribution of states $p(\vec{x_k})$ are known and correspond to the canonical or grand canonical ensembles, depending on the type of transition in question. This equilibrium condition places a constraint on the ratio of transition probabilities. For adsorption (ads) and desorption (des) moves,

$$\frac{W_{ads}}{W_{des}} \propto e^{-\beta(E_{des}-\mu)} \tag{2.42}$$

and for diffusive moves,

$$\frac{W_{i\rightarrow j}}{W_{j\rightarrow i}} \propto e^{-\beta(E_j-E_i)} \tag{2.43}$$

where $E_{des}$ denotes the change in energy between the unbound (desorbed) and bound (adsorbed) states, $\mu$ is the chemical potential of the ideal gas that the simulation cell is immersed in, and $E_i$ and $E_j$ correspond to the energy of the initial and final states, respectively.

While the detailed balance condition fixes the ratio of the transition rates to ensure the system converges to the correct equilibrium distribution, the absolute rate constants or at least those with a correct dynamical hierarchy are required for the investigation of dynamical phenomena.[71]. For activated processes, a pre-exponential factor is typically employed which is interpreted as a measure of the attempt fre-

quency of the move. Not surprisingly, this factor depends on the vibrational partition functions for the initial and transition states. A constant value of $10^{12} - 10^{13}\ s^{-1}$ is typically utilized as a crude approximation[70]. For non-activated processes, such as adsorption, this approximation is not valid as the pre-exponential factor needs to account for the large entropic loss in going from a free state in the gas phase to being bound to the surface of a material.

In this study, the pre-exponential factors for each rate constant are kept as free parameters in order to adjust the relative weights of each move type. This allows for a direct analysis of systems that, for example, may be limited by the rate of diffusion or may suffer from a high rate of desorption. In this context the transition probabilities for adsorption, desorption, and diffusion take the explicit form of

$$W_{ads} = \kappa_{ads} e^{\beta\mu} \quad W_{des} = \kappa_{des} e^{\beta E_{des}} \quad W_{i\to j} = \kappa_{ij} e^{\beta E_i} \quad W_{j\to i} = \kappa_{ji} e^{\beta E_j} \tag{2.44}$$

where $\kappa$ denotes the pre-exponential factor for each move type. At least three different regimes are typically of general interest: 1) The rate of diffusion is much larger than adsorption/desorption. 2) The rate of adsorption/desorption is much larger than diffusion. 3) The rates of diffusion and adsorption/desorption are comparable.

An important quantity of interest which results from the rf-KMC simulation is a measure of how long it takes for a system to reach equilibrium. A commonly used measure of this in experiments is the characteristic time, defined as the time required for the assumed pseudo-exponential coverage term to decay to $e^{-1}$. In practice, this will be determined by plotting the averaged coverage $N(t)$ available from the simu-

lations according to,

$$\ln\left(1 - \frac{N(t)}{N_{eq}}\right) = -\frac{1}{\tau}t \tag{2.45}$$

where $N_{eq}$ is the average coverage value and $\tau$ is the characteristic time. By plotting the left hand side of this equation vs the right hand side and finding the slope, the characteristic time can be obtained.

## 2.5 Software

The GCMC simulations were performed using a modified version of the Large-scale Atomic/Molecular Massively Parallel Simulator (LAMMPS)[15]. The 15May2015 version of LAMMPS was selected as the base for all code modifications. Below is a summary of the main modifications, extensions, and bug fixes made in order to perform the GCMC simulations conducted in this study:

- Bug Fix: Some successful rotation moves resulted in the center of mass of molecules moving outside of the GCMC simulation region.
- Added Feature: An option was added to prevent translation moves outside of the GCMC region.
- Added Feature: Dynamic tail corrections for energy and pressure were added for pairwise forces for fixes that cause the density of the system to change during the course of the simulation.
- Bug Fix: The functional form of the 10-4-3 wall potential was incorrect.
- Bug Fix: The logic for the attempted translation moves within a GCMC region could result in branching into an infinite while loop.

- Bug Fix: The energy calculated during a deletion move when using the full-energy option erroneously included the atom/molecule selected for possible deletion.
- Bug Fix: The functional form of the probability of atomic insertion was incorrect.
- Bug Fix: The insertion of molecules containing charged atoms resulted in an incorrect coulomb energy term when using the full-energy off option.
- Bug Fix: The full-energy on option included intramolecular forces resulting in very low insertion probabilities.
- Added Feature: The ability to dynamically adjust the maximum linear and rotational displacement values to achieve a target move acceptance percentage during the equilibration phase was added.
- Added Feature: A 2D and 3D pair-style table command was added which allows for the calculation of interactions due to general continuously represented surfaces.
- Added Feature: An option was added to use energy biasing in order to increase the acceptance of insertion moves.
- Optimization: The update of the gas list was optimized to remove an unnecessary center of mass calculation.

KMC simulations were performed using a modified version of Stochastic Parallel PARticle Kinetic Simulator (SPPARKS)[30]. The 26Feb2016 version of SPPARKS was selected as the base for all code modifications. Below is a summary of the

main modifications, extensions, and bug fixes made in order to perform the KMC simulations conducted in this study:

- Added Feature: Support for adsorption moves
- Added Feature: Support for desorption moves
- Added Feature: Support for binary gas species
- Added Feature: Species specific binding energy
- Added Feature: Location specific binding energy
- Added Feature: Support for multiple lattice types
- Added Feature: Environment dependent interactions
- Added Feature: Fine grained move statistics
- Added Feature: Enable rate constant adjustments
- Added Feature: Support for lattices of general configurations and connectivity (lattice vectors)
- Added Feature: A Command Line interface is being developed to automate the setup, submission, and post processing of the simulation scheme

All code is available at the following public repository: https://github.com/jpetucci/DU_dissertation_software.

# Chapter 3

# Results - Equilibrium

As discussed in Chapter 2, the investigation of adsorption through stochastic equilibrium methods, such as Grand Canonical Monte Carlo, allows one to elicit properties of systems that are beyond the time scale limitation of deterministic methods such as Molecular Dynamics. With GCMC, we can easily model the structure of an adsorbate using a non-lattice based approach with pairwise, or if necessary, more realistic many-body interactions. Due to this, equilibrium methods are much better suited for analyzing the location and strength of a material's binding sites as well as the underlying structure of the equilibrium adsorbed phase, as these would be inputs to a lattice based model. In the subsequent sections, adsorption is investigated for a variety of adsorbates on model carbon nanohorn aggregates and nanotube bundles; with the goal of developing structural and interaction models to describe the process of adsorption and identifying the key parameters/variables at play.

This chapter is organized as follows. In Section 3.1, calculations are presented which demonstrate the applicability of the chosen carbon dioxide interactions. In

Section 3.2, GCMC gas adsorption results for ethane on carbon nanohorns are given. Section 3.3 contains GCMC results for the adsorption of carbon dioxide on nanotube bundles. Finally, in Section 3.4, different structural models for nanotube bundles are compared and contrasted for various sorbent gases ($CO_2$, $C_2H_6$, and Ar).

This chapter contains content from the following journal articles co-authored by myself as permitted by the respective publishing entities (Royal Society of Chemistry and American Chemical Society):

[1] "Ethane adsorption on aggregates of dahlia-like nanohorns: experiments and computer simulation" in Phys. Chem. Chem. Phys., 2016, 18, 15436.

[2] "Thermodynamics and Kinetics of Carbon Dioxide Adsorption on HiPco Nanotubes" in J. Phys. Chem. C 2018, 122, 20410.

## 3.1 $CO_2$ Interactions

### 3.1.1 Graphitic Quadrupole Moment

The interaction between a surface and gas is more complex if either the gas or surface material has an intrinsic electric field. The interaction of carbon dioxide, which is a quadrupolar molecule, and graphitic materials (graphene, graphite, nanotubes, nanohorns, etc.), which has a quadrupole on each carbon atom due to the $\pi$-electrons, therefore may need to account for additional electrostatic interactions.[54, 55]

Single point energy calculations have been carried out to determine the quadrupole-quadrupole interactions between the carbon atoms comprising the substrate material

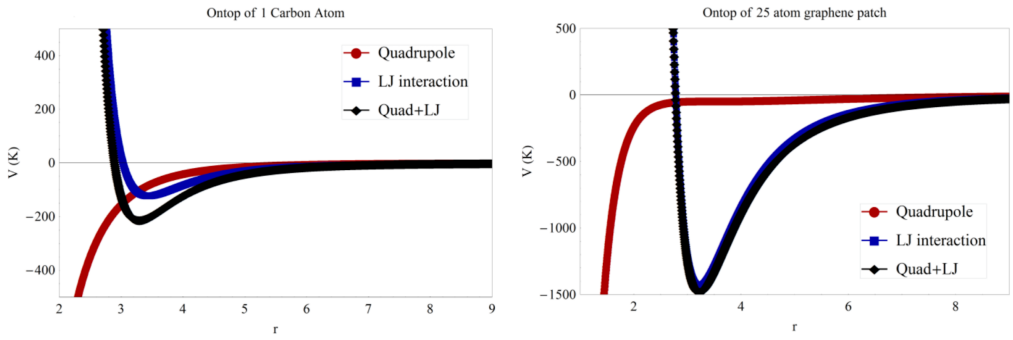


Figure 3.1: Substrate-CO2 interaction energy plots explicitly showing the quadrupole and LJ contributions.

and the $CO_2$ gas molecules as a function of separation distance. This interaction energy is calculated between the point charges present in the extended charge model for $CO_2$ (Table 2.1) and vertically oriented (perpendicular to the surface) quadrupoles centered on each carbon atom ($Q = -3.03 \times 10^{-40} \mathrm{Cm}^2$)[56] using Eqn. 2.4. The most favorable energetic configuration is adopted, where carbon dioxide is directly above a carbon atom (quadrupoles form a 'T-shape'), for a single carbon atom and the surface of a 25 atom graphene patch.

The results depicted in Figure 3.1 show that as the number of carbon atoms increases, the quadrupole-quadrupole interaction contributes less to the total interaction curve. This is due to the shifting of the quadrupole interaction that occurs as more atoms are added to the substrate, which is consistent with the findings of Kocman *et al.*[56] that the contribution goes to zero for an infinite sheet of graphene. Similar single point energy calculations have been performed for a $(11, 3)$ nanotube of length 10 nm as shown in Figure 3.2. Here, the quadrupoles located on the carbon atoms are oriented radially out of the tube.

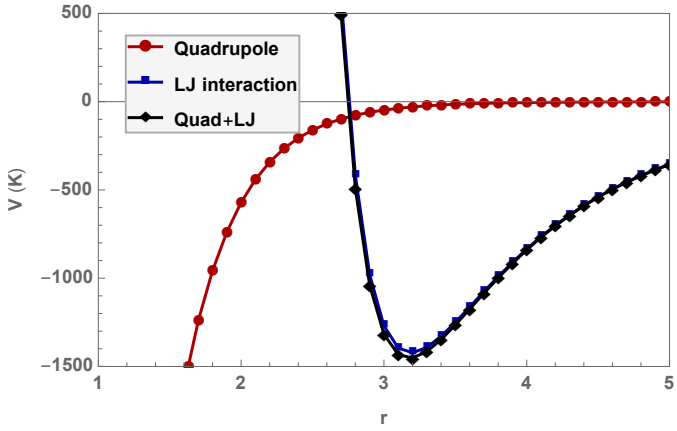


Figure 3.2: Nanotube-CO2 interaction energy plots explicitly showing the quadrupole and LJ contributions.

These results show only a 2-4% maximum deviation (depending on the size and chirality of the nanotubes, size and corrugation of the graphene patch, etc.) in the interaction energy when the quadrupole-quadrupole interaction is included along with the base Lennard-Jones interaction. Due to the weakness of the surface-gas quadrupole-quadrupole interaction for the $CO_2$-Carbon materials of interest, it can be neglected without incurring a significant error.

### 3.1.2 Bulk Carbon Dioxide Interactions

As the saturated vapor pressure value is reached along an isotherm, the isosteric heat of adsorption approaches a limiting value equal to the latent heat for the associated phase transition. Depending on the temperature, this transition either corresponds to liquid-vapor or solid-vapor. For temperatures below the triple point temperature, the phase coexistence is between solid and vapor. Between the critical and triple point temperatures, there is coexistence between the vapor and liquid phases. The isosteric heat of carbon dioxide, which has triple point temperature of

216.6K, will then approach a value corresponding to the latent heat of sublimation at high coverage for the temperatures considered later in this study. In this regime, the bulk phase is deposited. It is therefore imperative that the selected $CO_2$ interactions (Chapter 2.1.1) have the ability to produce a 3D solid with appropriate structure and energy, given the unique behavior of this sorbate's isosteric heat curve.

Simulated annealing calculations[63] were performed to determine the optimal solid configuration for the three charge site model of carbon dioxide. Given that the known crystal structure of the solid phase is face-centered cubic (FCC)[73, 74], $CO_2$ molecules were randomly oriented and placed with their molecular center at FCC lattice sites in the initial system configuration. A cubic and periodic simulation cell comprised of 32000 molecules with a side length of $20a$ was used, where $a$ is the lattice constant. For a chosen lattice constant, the system is then evolved from the initial configuration using molecular dynamics. The system is heated to an equilibrium temperature of 150K with the Berendsen thermostat using $1 \times 10^6$ MD steps and then all the kinetic energy is drained using a drag force proportional to the to the atomic velocities $-\gamma v_i$ in $2 \times 10^7$ MD steps. The system configuration and associated energy at the end of the run is defined as optimal for the chosen lattice constant. By performing a series of simulations, differing only by the lattice constant, the minimum energy lattice constant and optimal system configuration can be determined.

The results of the simulated annealing calculations are summarized in Figure 3.3a. The optimal lattice constant is determined to be 5.55 Å, at a minimum energy of 297.5 meV per molecule. These results compare favorably with those reported in the literature, for example Sponer *et al.*[73] reported values of 280 meV and 5.54 Å, for the cohesive energy and lattice constant, respectively. Figure 3.3b depicts

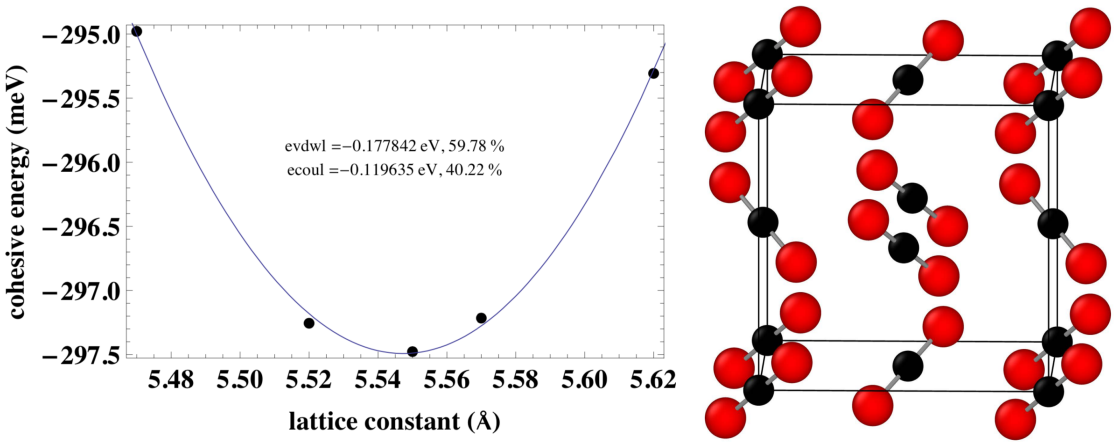


(a) (b)

Figure 3.3: (a) Optimal lattice constant for FCC carbon dioxide. Data points correspond to MD simulations, the curve is a polynomial fit. (b) The cubic Pa3 structure of solid structure $CO_2$ in the minimum energy configuration

the minimum energy configuration of carbon dioxide. This structure corresponds to the well known cubic *Pa3* (phase I) structure of solid $CO_2$[74], where molecules are centered on FCC lattice sites with orientations optimized for the electrostatic interactions. This calculation displays the importance of the orientationally dependent quadrupole-quadrupole energy, which accounts for 40% of the total bulk phase energy. This calculation shows that under the correct conditions, the interaction model used for carbon dioxide can produce the correct bulk phase.

The validity of an extended model, in which charges are placed on the Lennard Jones sites of a carbon dioxide molecule for the quadrupole-quadrupole interaction, requires justification. Specially, the interaction needs to demonstrate the correct behavior at large separation ($-r^{-5}$) to ensure that the use of a cutoff is valid. The values and locations of the charge sites are chosen in this model such that the monopole and dipole terms are zero at long separation. Here the electrostatic interaction energy

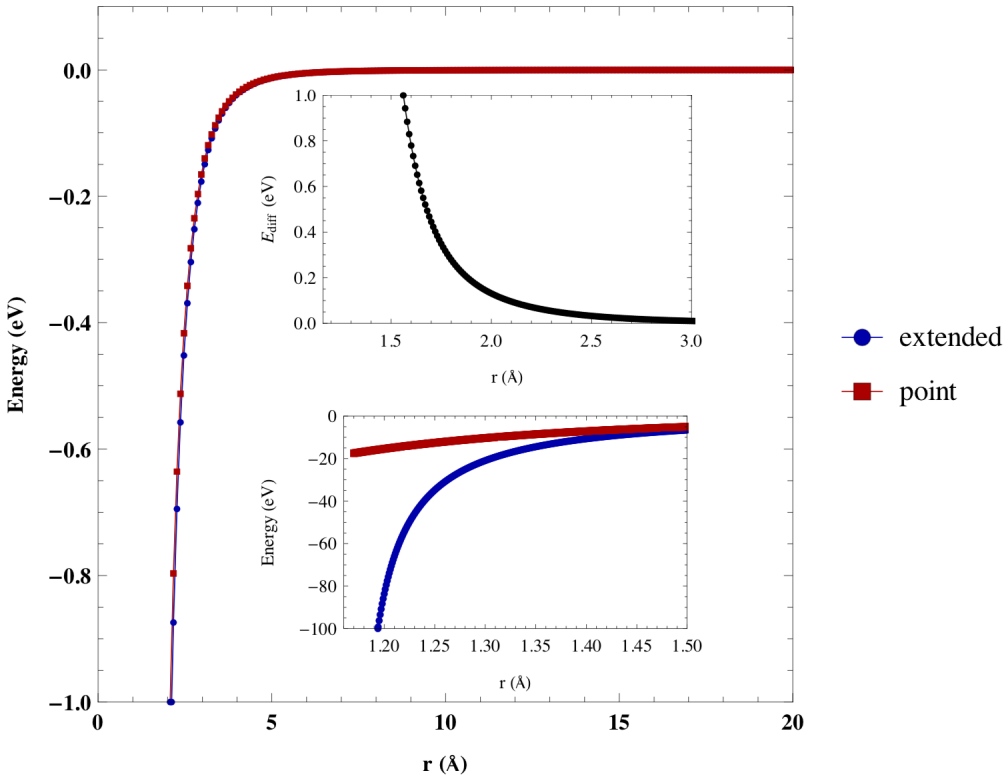


Figure 3.4: Comparison of the interactions between a pair of linear quadrupoles represented by point or extended charge distribution

of the extended charge model and explicit linear quadrupole will be compared to determine the region of validity.

A series of single point energy calculations were carried out to determine the interaction energy as a function of separation for the two quadrupole models. First, the lowest energy orientation for each model was determined by randomly placing two quadrupoles into a simulation cell with non-periodic boundaries and minimizing the energy using the steepest descent algorithm. Multiple energy minimization simulations with randomized initial positions and orientations were used to ensure that the quadrupoles converged to a consistent configuration. For both models, the lowest

energy configuration was found to be when the quadrupoles are oriented perpendicular, forming a 'T-shape'. Using this optimal orientation, the separation of quadrupole centers was increased in increments of 0.1 Å, where the energy was calculated for each separation value.

The results of the calculation are summarized in Figure 3.4, where the interaction energy is plotted as a function of distance. The main curve shows the consistency between both models for large separations consistent with the limiting ($-r^{-5}$) (Eqn. 2.5) expected form. The figure insets show a zoomed in view of the interaction and energy difference at shorter separation distances, where the agreement breaks down. At close distances ($< 3$ Å), the multipole expansion no longer rapidly converges and is therefore not dominated by the first non-zero pole. This calculation shows that the use of a molecular cutoff is valid with the extended charge model of a linear quadrupole. In addition, the nearest neighbor distance found for the solid $CO_2$ in Figure 3.3 of 3.92 Å ($a/\sqrt{2}$) is close to the distance at which the quadrupole term in the multipole expansion no longer dominates, favoring the use of the extended model.

## 3.2 Ethane on Nanohorns

As discussed in Chapter 1, the interest in studying ethane adsorption on carbon nanohorn aggregates is its position as a model linear sorbate. The adsorptive properties of ethane can provide insight into general questions in regards to how the sorption characteristics of a given system depend on the structure of both the gas species and the sorbent material. Of particular interest for ethane is the absence of

distinct isotherm steps, which are a common feature in the adsorption of spherical adsorbates, such as Ne and $CF_4$, on nanohorns.

Here, grand canonical Monte Carlo simulations are carried out to investigate the effect of different structural models of individual nanohorns as well as aggregates on the isotherm and isosteric heats of adsorption. Explicit access to the equilibrium molecular configurations of the adsorbed sorbate at increasing pressures allows us to directly correlate the features observed in the experimental isotherms with the formation of adsorbed phases in different regions of the aggregate. This allows us to address questions such as where the gas is adsorbing, the structure of the adsorbed phase, as well as the cause of the lack of isotherm sub-steps. In this section, computational results are used to compare and explain experimental results from the Migone group[14].

An abridged version of the computational results presented in this section has been published in the following journal article:

> "Ethane adsorption on aggregates of dahlia-like nanohorns: experiments and computer simulation" in Phys. Chem. Chem. Phys., 2016, 18, 15436.

### 3.2.1 Modelling and computer simulations

Due to the intrinsic heterogeneity of the aggregate arrangement and the limited knowledge of morphological details of the nanohorns, different models of the configuration and geometry were used to identify the structural features needed to best reproduce the experimentally observed adsorption behaviour. A model of a triangu-

lar array of parallel nanotubes (diameter of 20 Å) was used, with their ends closed by a hemispherical cap and a wall-to-wall separation distance of 3.4 Å. In addition to hemispheres, several caps of varying heights in the form of a paraboloid were also considered. Beyond using a capped nanotube as the model shape for a nanohorn, individual paraboloid (without a nanotube) were also modelled as potential nanohorn structures. The three structural models used to represent individual nanohorns are depicted in Figure 3.5.

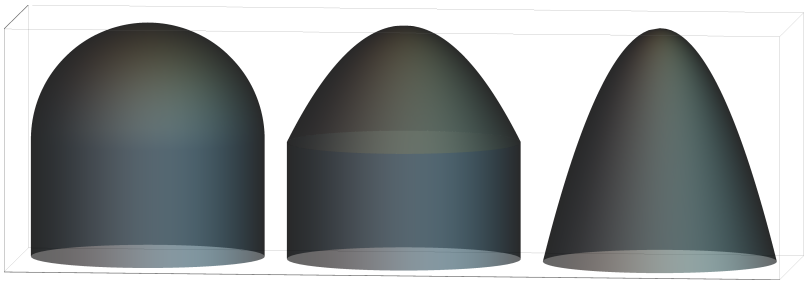

Figure 3.5: The three model structures for individual nanohorns: (Left) Cylindrical tube capped with a hemisphere, (Middle) Cylindrical tube capped with a paraboloid, (Right) Pure Paraboloid

The overall rationale behind these models is that they allow for the smallest adsorption spaces possible at the base of the caps while the region between the caps' walls provides increasingly wider adsorption spaces that resemble the outer sections of the aggregates.

GCMC simulations (Section 2.3) for ethane ($C_2H_6$) were performed on the model structures using the Metropolis Monte Carlo Algorithm. After reaching equilibrium, a GCMC run at fixed temperature, $T$, and volume, $V$, provides the average number of adsorbed molecules, $N$, as a function of either the chemical potential, $\mu$, or pressure, $P$. As justified in the next subsection, excess coverage effects are negligible for the temperature and pressure ranges considered. Then, by performing multiple GCMC

runs for a series of $\mu$ or $P$ values at a constant $T$, an adsorption isotherm curve can be generated. Each point of the adsorption isotherm is calculated using a GCMC run of $22.5 - 60$ million steps to bring the system into equilibrium, followed by $22.5 - 60$ million steps to take averages. Every MC step is comprised of a trial creation, destruction, displacement, or rotation move with attempt probabilities of 0.3, 0.3, 0.2, 0.2, respectively. In addition to this, the maximum rotation and displacement steps were dynamically adjusted during the equilibration phase to achieve a move acceptance value of 50%.

The coarse graining methods discussed in Section 2.1.2 were used to represent the model nanohorn structures as continuous distributions of carbon atoms with an effective surface density as well as the ethane molecule as two rigidly bonded methyl groups. The gas–gas and gas–substrate interactions are modelled using a Lennard-Jones potential (LJ) with a cut-off of $10\sigma$. The LJ potential parameters used are given in Table 2.1, where the unlisted mixed parameters are given by the standard Lorentz–Berthelot (Eqn 2.2).

In the early stages of this investigation an atomistic description of the carbon caps was explored. The coordinates of the carbon atoms comprising the cap were obtained from the open source program NanoCap, developed by M. Robinson *et al*[75, 76]. It is, however, important to note two things about this approach: firstly, as the authors clearly discuss, the possible ways of closing a nanotube of a given chirality with a carbon cap increases dramatically with the size of the tube, with all the cap configurations sharing very similar energies. Also, the un-optimized hemispherical cap generated by this algorithm using the default triangulated dual lattice force field settings produced a cap with a carbon surface density of approximately 0.48 $\text{Å}^{-2}$, a

value much higher than the typical 0.38 $Å^{-2}$ (characteristic of graphene, nanotubes, or $C_{60}$ molecules). Given the limitations on the exact knowledge of the aggregates, the surface density of the caps within the continuous carbon representation was kept as a variable in the simulations to understand its possible effects. The surface density of the tubes is fixed at 0.38 $Å^{-2}$ in all cases.

The adsorption of ethane is simulated on the exterior of a two-dimensional triangular lattice comprised of vertically oriented ($z$-direction) capped-nanotubes or paraboloids placed at each lattice point. The orthorhombic computational cell of dimensions 47.5 Å ×42.1 Å ×70 Å accommodates four such structures. Periodic boundary conditions were employed in the $x$- and $y$-directions with reflecting walls used along the axial $z$-direction. The length of the cell along this direction (70 Å) is large enough to avoid spurious effects that the presence of the walls may originate.

### 3.2.2 Results and Discussion

**Hemispherical cap:** Figure 3.6 shows simulated isotherms performed for nanotubes (with height $h = 10$ Å) closed with hemispherical caps (with radius $R = 10$ Å) and a carbon density of 0.48 $Å^{-2}$, for temperatures ranging from 125 to 200 K. As shown in the configurations depicted in Figure 3.7, the first isotherm step corresponds to filling the very narrow spaces between three tubes with a line of molecules along the tubes, while the second occurs as the molecules fully encircle the tubes, at the base of the caps. It should be noted that the first step in the simulated isotherms is only an artifact of the model that does not relate to the actual experimental systems. Comparison with the observed experimental behavior of Russell et al.[14] is therefore only meaningful for coverages above $N \sim 35$. The main and tallest step builds up

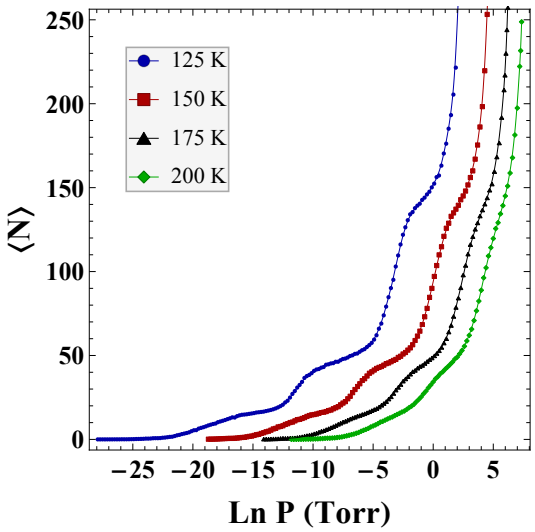


Figure 3.6: Simulated adsorption isotherms of ethane on hemi-spherically capped ($R = 10$ Å) nanotubes ($h = 10$ Å) at temperatures 125-200 K; the cap surface carbon density is 0.48 Å$^{-2}$.

as the molecules start to cover the external walls of the caps, from the bottom to the top, as can be seen in Figure 3.7. This steeper, taller sub-step corresponds to the lower binding energy sites, in agreement with the experimental isotherm reported by Russell et al.. Once this "monolayer" is completed at about $N \sim 150$, molecules quickly accumulate forming a thicker film, with no evident structure, that resembles the ethane bulk phase as the pressure reaches the saturation value.

An upper estimate for excess coverage effects (Eqn. 2.31) was calculated using the accessible volume given by the difference between the simulation cell volume and volume occupied by four hemi-spherically capped nanotubes. This volume ($\sim 119040$ Å$^3$) was used along with the equation of state of an ideal gas to calculate the excess coverage for the temperature and pressures considered. At monolayer coverage ($N \sim 150$), the excess coverage at 200 K corresponds to a 1.8% correction in the number of adsorbed molecules. At this same temperature at higher coverages ($N \sim 250$) the

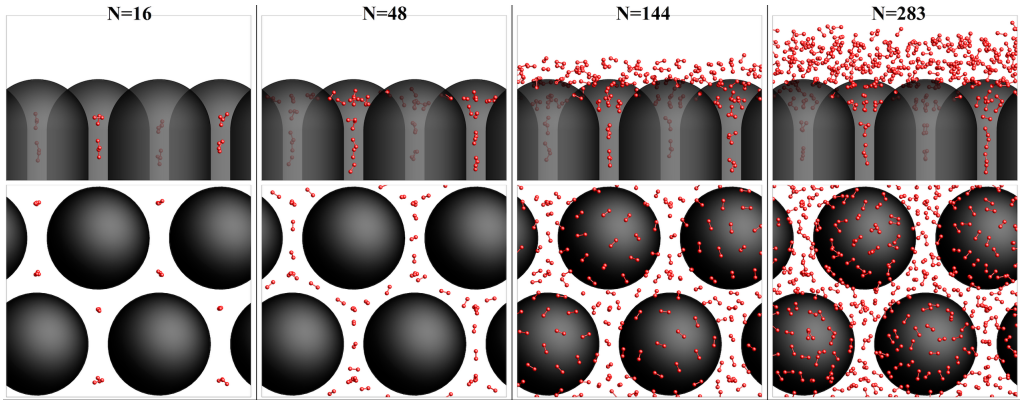


Figure 3.7: Side and top views of molecular configuration snapshots of ethane on hemi-spherically capped ($R$ = 10 Å) nanotubes ($h$ = 10 Å) at 150 K at increasing coverage; the cap surface carbon density is 0.48 Å$^{-2}$.

correction is 4%. At the lowest temperature of 125 K, the corrections correspond to 0.005% and 0.03%, for the monolayer and higher coverage regimes, respectively. It can therefore be concluded that excess coverage effects are not significant for the pressure and temperature ranges considered.

The bulk triple and critical points for ethane are 91 K and 305 K, respectively.[14] As all simulated isotherms fall within this temperature range, saturation corresponds to liquid-vapor coexistence. The isosteric heat of adsorption at high coverages then corresponds to the bulk heat of vaporization of ethane (152.8 meV[14]). In Figure 3.8, the isosteric heat values are shown, which correspond to the isotherms from Figure 3.6, as a function of the coverage. The isosteric heat is calculating using the average potential energy as given by Eqn. 2.28.

The dashed lines used in Figure 3.8 are to identify key features, allowing for a comparison with the experimental results given by Russel *et al.*[14]. The vertical line at $N \sim 35$ marks the beginning of the simulated coverage to be compared with experiment, as previously mentioned. The main plateau identified, which falls between

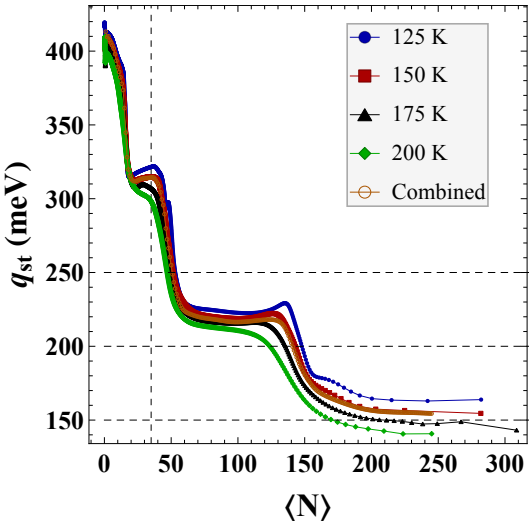


Figure 3.8: Isosteric heat of adsorption as a function of coverage for ethane on hemispherically capped ($R$ = 10 Å) nanotubes ($h$ = 10 Å) at various temperatures; the cap surface carbon density is 0.48 Å$^{-2}$. The combined curve is derived from the isotherm data given in Fig. 3.6

the range found experimentally as indicated by the horizontal dashed lines at 250 and 200 meV, corresponds with adsorption happening on the external walls of the caps. The agreement with the experimental results indicates that molecules are mostly occupying the outer regions of the aggregate. The features present at lower loadings in the experimental results most likely originated on a few sites in the narrower regions of the aggregate sample (corresponding to the sites at the base of the caps in the simulations), in addition to other possible higher binding defects in the aggregates. It is noted that all of the isosteric heat values in the main plateau region are above the bulk heat of vaporization.

The average total potential energy per molecule at 150 K as well as the individual contributions provided by the gas–surface interactions and the gas–gas interactions are shown in Figure 3.9 as a function of coverage. At low coverage, the energy is

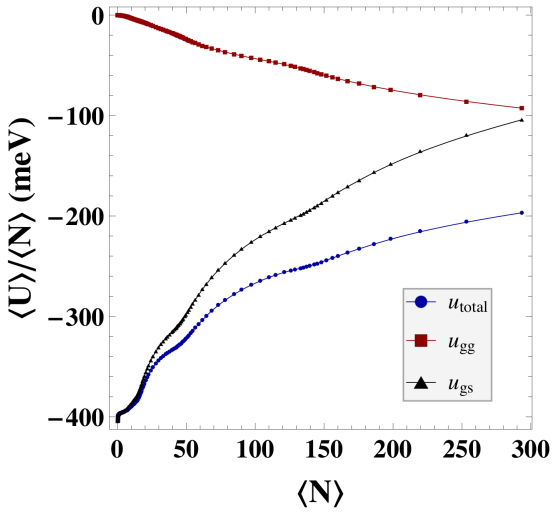


Figure 3.9: Average total, gas-gas (gg), and gas-substrate (gs) potential energy per molecule as a function of coverage for ethane adsorption on hemi-spherically capped ($R = 10$ Å) nanotubes ($h = 10$ Å) at 150 K; surface carbon density is 0.48 Å$^{-2}$

mostly determined by the external potential from the tubes (the gas–surface interactions); as the number of molecules increases, the effect from the surface decreases steadily while the molecular interactions become progressively more important. As the film approaches the bulk phase, the total energy reaches its final decreasing slope corresponding to the isosteric heat value of this phase. The kinks in the total energy per molecule indicate the transition points between the phases forming at the base of the caps and on the walls of the cap, before forming the multi-layered film near saturation.

The impact of carbon cap surface density is explicitly explored in Figure 3.10. Here, the isosteric heat of adsorption for ethane at 150 K on hemi-spherically capped ($R = 10$ Å) nanotubes ($h = 10$ Å) with a cap densities of 0.38 and 0.48 Å$^{-2}$ are compared along with a full atomistic representation of the hemi-spherically capped nanotubes. It is apparent that the larger carbon density of the cap results in an

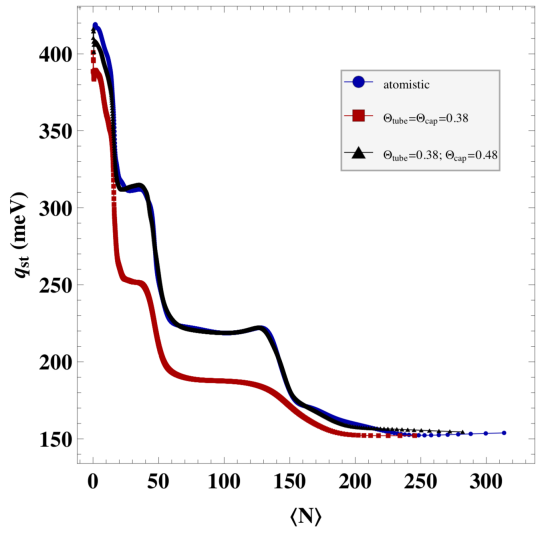


Figure 3.10: Isosteric heat of adsorption as a function of coverage for ethane on nanotubes with hemispherical caps of varying density at 150 K.

upwards shift of the isosteric heat at lower coverage values due to the stronger gas-surface interactions. The agreement between the atomistic representation and continuous surface with tube carbon surface density of 0.38 $\text{Å}^{-2}$ and cap carbon surface density 0.48 $\text{Å}^{-2}$ shows the validity of the continuous approximation.

**Mixed morphology:** The effect of the chosen morphology on the isosteric heats was first analyzed by considering two additional individual nanohorn structures: nanotubes with a paraboloid cap, and paraboloids with no nanotube present. Each of these structures has a total height and base-diameter of 20 Å. In all cases, the carbon density is set equal to 0.38 $\text{Å}^{-2}$ as this is the typical value for most of the uniform surface carbon structures (note that this is lower than the 0.48 $\text{Å}^{-2}$ value used for the hemispherical caps suggested by the atomistic approach and used in the preceding section.

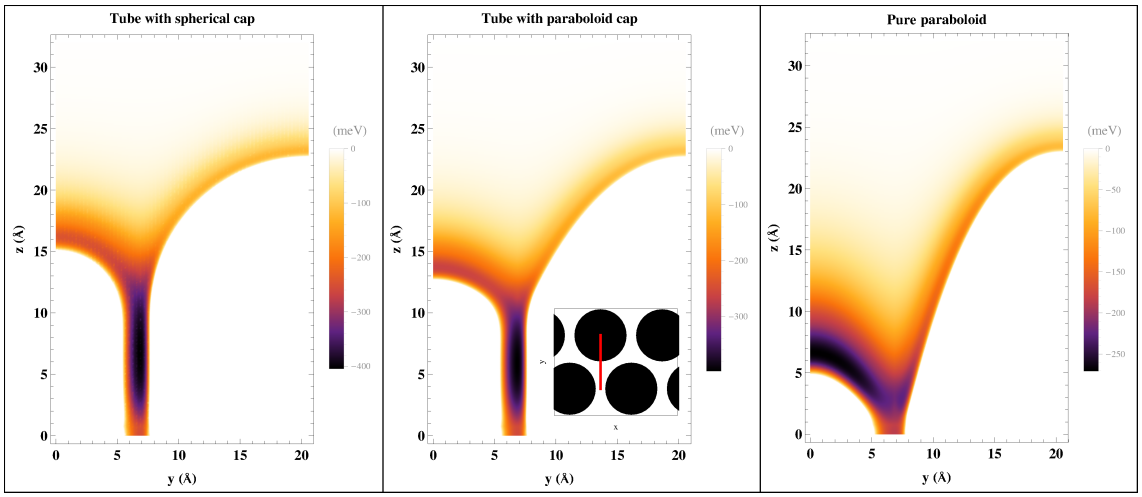


Figure 3.11: Potential Energy Surface calculation for an ethane molecule interacting with the three model nanohorn structures. The red line in the center inset depicts PES plane

A potential energy surface (PES) calculation was performed for an energetic comparison between the three nanohorn models and the results are presented in Figure 3.11. This figure was generated using the methods discussed in Chapter 2.2, where canonical Monte Carlo (MC) simulated annealing was utilized to find the minimum energy orientation at each grid point. With MC simulated annealing, the system is first evolved to equilibrium at an elevated temperature ($T_0 = 200$ K) using the rotational acceptance probability given in Chapter 2.3. The temperature of the system is then decreased geometrically according to geometric sequence given by, $T_i = T_0(\frac{3}{4})^i$, where for each new temperature $T_i$ the system is again equilibrated. As the temperature of the system approaches 0, the ethane molecule adopts the lowest energy configuration. The red line in the inset of Figure 3.11 depicts the slice in the $zy$ plane for which the PES was calculated. The capped tubes are energetically similar, with minimum energy sites of $-400$ meV located in the middle of the triangular region

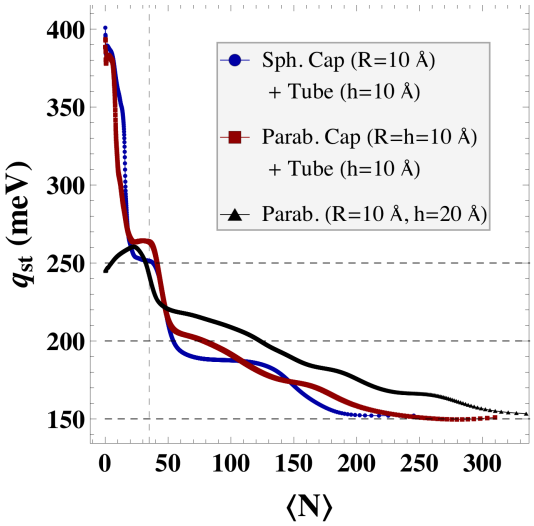


Figure 3.12: Isosteric heat of adsorption as a function of coverage for ethane on nanotubes with hemispherical and paraboloidal caps, and a pure paraboloid (no tube) at 150 K; the cap carbon density is 0.38 Å$^{-2}$.

formed by three capped tubes at about 5 Å above the $z = 0$ plane. For the the pure paraboloid surface, the minimum in energy is smaller in magnitude ( $-270$ meV) and shifts to between two adjacent nanohorns at about 6.5 Å above the $z = 0$ plane. For all three nanohorn structures, an energy gradient is observed in the $z$-direction.

Figure 3.12 depicts the isosteric heat corresponding to the three model nanohorn structures at a temperature of 150 K. Comparing the result shown here for hemispherically capped nanotubes with Fig. 3.8, the effect of the carbon surface density is clear; a higher density increases the isosteric heat in coverage regions where gas–surface interactions dominate. It is observed that the more elongated paraboloid shape leads to consistently higher isosteric heats across the whole coverage range, which generally improves the agreement with the experimental results of Russel *et al.*[14]. This elongation also tends to make the change in energy from the higher binding sites to the bulk value more gradual as the molecules follow the change in

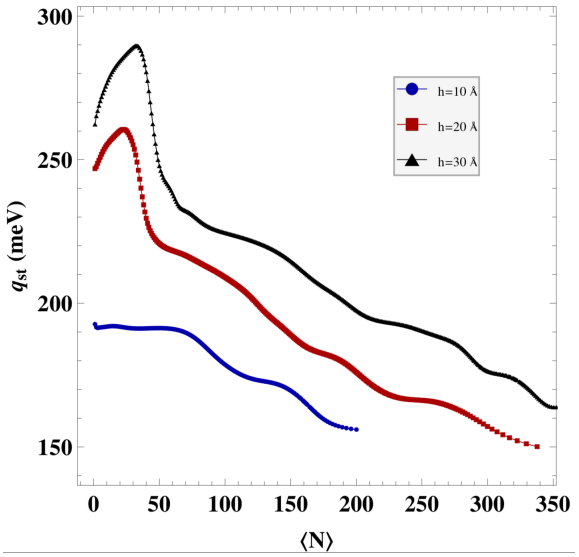


Figure 3.13: Isosteric heat of adsorption as a function of coverage for ethane on paraboloids of varying heights.

potential energy over the paraboloid structure as shown in the PES in Figure 3.11. A direct comparison of adsorption on pure paraboloid nanohorn structures of varying heights is presented in Figure 3.13. Here it can be seen that as the height of the paraboloid increases, the capacity and amount of energy variation tends to increase. The molecule configurations illustrated in Figure 3.14 also show a similar evolution as in Figure 3.7 with the main difference due to the larger number of molecules needed to cover the paraboloid surfaces.

**Spherical Aggregate morphology:** When compared with the experimental findings[14], these results suggest that the paraboloid structure may be a better model to reproduce the observed behavior, unless the carbon density is increased from its typical value of 0.38 $Å^{-2}$. However, it is observed that higher isosteric heat values can also be produced if the molecules feel the presence of additional carbon surfaces beyond that of an ideal triangular lattice geometry, a highly probable situation in the

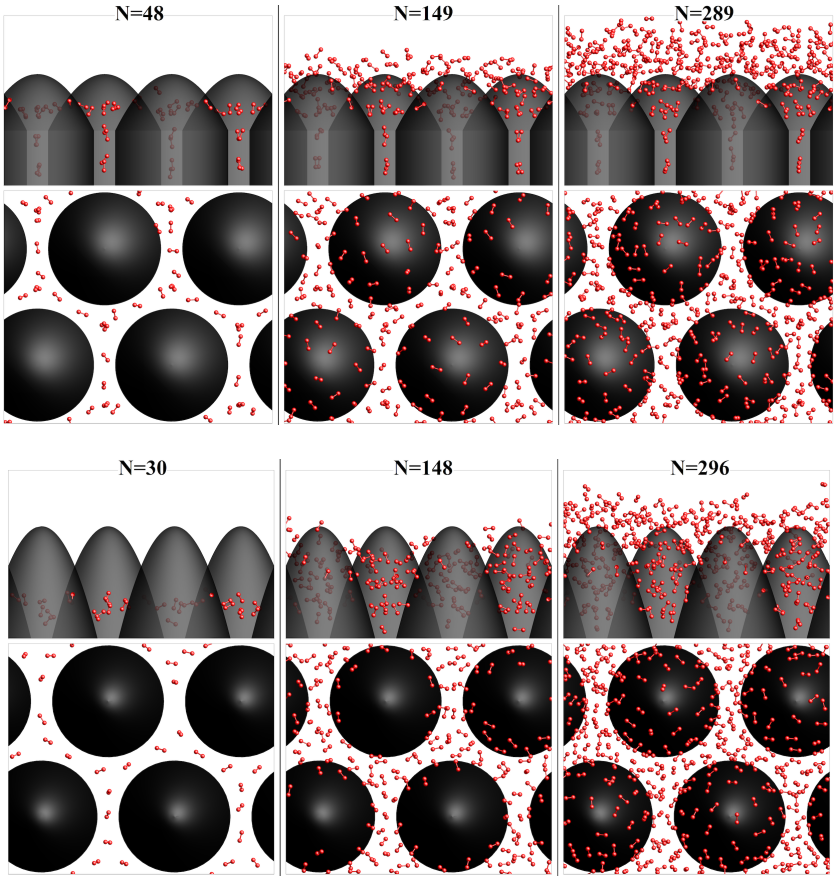


Figure 3.14: Side and top views of molecular configuration snapshots of ethane at 150 K (see Figure 3.12) on: (top) paraboloid capped ($R = h = 10$ Å) nanotubes ($h = 10$ Å); (bottom) pure paraboloids ($R = 10$ Å, $h = 20$ Å); in all cases, the carbon density is 0.38 Å$^{-2}$.

real aggregate. Therefore, as a final step on our modeling efforts, a spherical aggregate is considered which is made of nanohorns (with the typical carbon density of 0.38 Å$^{-2}$) as shown in Figure 3.15. Here, 62 paraboloid ($R = 10$ Å, $h = 30$ Å) structures are radially oriented and approximately uniformly spherically distributed. The location of the bases of the individual nanohorn structures were selected by patterning the surface of a sphere with a Fibonacci lattice[77]. One use of Fibonacci lattices is the patterning of arbitrary surfaces with an approximate uniform distribution. For the

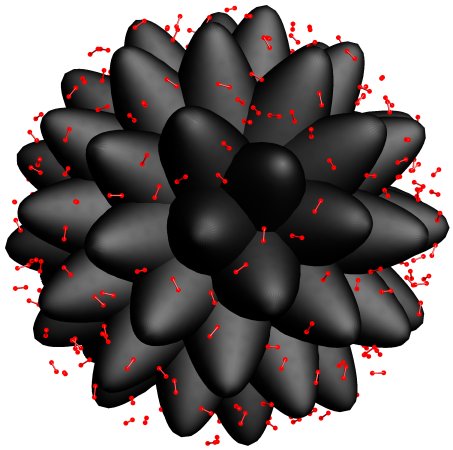

Figure 3.15: Snapshot of ethane adsorption on a spherical aggregate comprised of 62 radially aligned paraboloids.

patterning of a unit sphere with $N$ points, the positions on the surface are given in spherical coordinates with polar angle $\theta$ and azimuthal angle $\phi$,

$$\begin{aligned} \theta_i &= \arccos\left[(2i/N) - 1\right] \\ \phi_i &= i\gamma \end{aligned} \tag{3.1}$$

where $\gamma$ is the *golden angle* and $i$ takes on integer values from 1 to $N$.

The resulting isosteric heat is shown in Figure 3.16, which also includes the result for an aggregate structure made of hemi-spherically capped tubes. Even within the arbitrariness used to build this specific aggregate, it is apparent that the isosteric heat has generally increased and shows the best overall agreement with the experimental values, without the need to increase the surface carbon density. It is noted that the hemispherical caps tend to better reproduce the experimental coverage dependence suggesting that ethane is mainly absorbed on the most outer regions of the aggregate where only the very tip of the nanohorns produce the most noticeable effect.

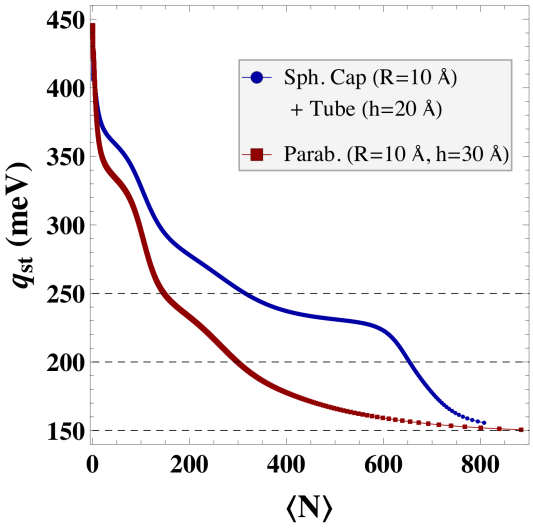


Figure 3.16: Isosteric heat of adsorption as a function of coverage for ethane on a spherical aggregate comprised of paraboloids and nanotubes with hemispherical caps at 150 K.

## 3.3 $CO_2$ on Nanotubes

As discussed in Chapter 1, the adsorptive behavior of carbon dioxide contrasts that of other sorbates, such as $H_2$, $N_2$, Ar, Ne, $CH_4$, $CH_4$, etc., on nanotube bundles. The unique sorbate-sorbate interactions present for $CO_2$ provide an opportunity to gain insight into how sorption characteristics depend on the gaseous species. Of particular interest in this case for carbon dioxide are the lack of distinct isotherm steps and the trending of the isosteric heat through a minimum value. On the sorbent side, nanotubes present a unique opportunity to study 1D phases of materials that present in the groove regions.

GCMC simulations are carried out to investigate the unique $CO_2$ sorbate isotherm and isosteric heat of adsorption features. The ability to explicitly decompose the energetic contributions to the isosteric heat as well as the access to the equilibrium

molecular configurations of the adsorbed phase at increasing pressures allow for the explanation of experimental results from the literature, especially from the Migone group[20].

An abridged version of the computational results presented in this section has been published in the following journal article:

> "Thermodynamics and Kinetics of Carbon Dioxide Adsorption on HiPco Nanotubes" in J. Phys. Chem. C 2018, 122, 20410.

### 3.3.1 Modelling and computer simulations

GCMC simulations were conducted to explore the equilibrium adsorptive behavior of $CO_2$ on the external surface of a carbon nanotube bundle. The procedure used in Section 3.2 is utilized again to generate adsorption isotherms from a series of runs at a fixed temperature. Each point of the adsorption isotherm is calculated using a GCMC run of 2-4 $\times$ $10^9$ steps to bring the system into equilibrium and to calculate averages. Every MC step is composed of a trial creation, destruction, displacement, or rotation move with attempt probabilities of 0.3, 0.3, 0.2, and 0.2, respectively. In addition to this, the maximum rotation and displacement steps were dynamically adjusted during the equilibration phase to achieve a move acceptance value of 50%.

The sorbent surface is modelled as the exterior of an infinite array of parallel single walled nanotubes (SWNT), of the same diameter (1.356 nm), arranged on a single plane (xy plane in the simulations). The wall-to-wall separation between the tubes is 0.32 nm. The simulation cell includes three nanotubes, spanning a distance of 50.28 Å

along the $x$-axis. This cell width is large enough to accurately account for the longer range of the $CO_2$–$CO_2$ interactions. Along the direction of the axis of the tubes (y-axis), the cell extends for a length of $20\sigma_{gg}$. Periodic boundary conditions are applied along both the $x$- and $y$-directions. The height of the cell (along the $z$-axis, pointing away from the plane of the tubes) is set to be 100 Å. This configuration choice for the representation of a nanotube bundle was made after a thorough exploration of many different models (as detailed in Section 3.4). The parallel array was chosen because it provided the most computationally cost-effective solution to reproduce and help understand the experimental results from the Migone experimental group[20]. As will be demonstrated, the unique characteristics of the gas–gas interaction for $CO_2$ in combination with its particular competition with the gas–surface interaction made the simulation results much more sensitive to the choice of the bundle model than is the case for the adsorption simulation of other adsorbates.

The $CO_2$–$CO_2$ interactions are modelled with the Harris–Yung potential[62], as discussed in Section 2.1.1, which represents the molecule as three linear Lennard-Jones sites with point charges centered at each site. The coarse graining methods discussed in Section 2.1.1 were used to represent the model nanotube structures as continuous distributions of carbon atoms with an effective surface density of 0.38 $Å^{-2}$. The gas–substrate interactions are modelled using a Lennard-Jones potential (LJ) under this continuous representation. The LJ parameters and charge values are given in Table 2.1. Molecules are not permitted to only partially interact with one another, which ensures proper convergence of the extended point charge quadrupole-quadrupole interactions.

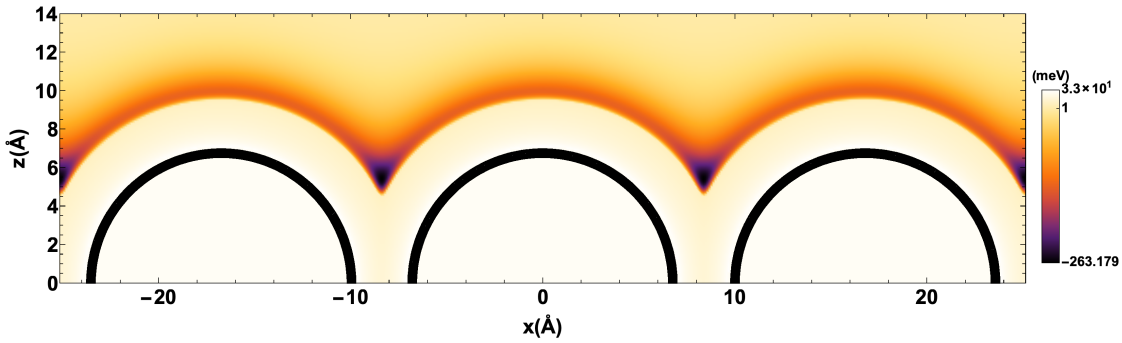


Figure 3.17: Potential Energy Surface calculation for a $CO_2$ molecule interacting with the model nanotube bundle. The black solid semicircle lines indicate the positions of the nanotubes.

### 3.3.2 Results and Discussion

A potential energy surface (PES) calculation was performed to show the energetic properties of the chosen nanotube bundle model and the results are presented in Figure 3.17. This figure was generated using the methods discussed in Chapter 2.2, where a series of single point energy calculations were used to find the energy at each grid point. The minimum energy orientation of the $CO_2$ molecule occurs when it aligns parallel to the tubes with the molecular axis oriented in the $y$ direction. The inner pore of the nanotube is closed in as-produced nanotubes, therefore no binding sites are present for inside of the nanotubes depicted by the black semicircular lines. On the exterior, two distinct binding site regions are shown: (1) The groove site, occurring between adjacent nanotubes, with strongest binding energy at $-263$ meV and (2) the external surfaces of the nanotubes away from the groove region which have an energy of around $-133$ meV.

A set of adsorption isotherms obtained from the simulations are presented in Figure 3.18 for temperatures ranging from 100 to 200 K. Excluding the lowest tem-

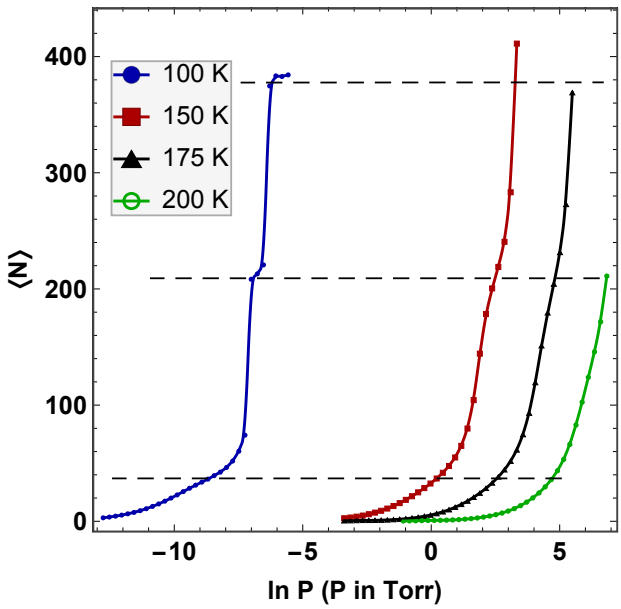


Figure 3.18: Adsorption isotherms from the simulations for carbon dioxide on a nanotube array bundle. The dotted lines indicate the coverage at which the three main configurations (groove, monolayer, and bilayer) can be resolved at low temperature.

perature, this temperature range was chosen for comparison with experimental results obtained by the Migone group[20]. The lowest temperature was used to better identify adsorption features that might be smoothed out by temperature effects. The isotherms are consistent with those obtained experimentally, substeps are practically nonexistent and hardly visible only at the lowest temperatures. This minor difference with respect to the experimental isotherms of the Migone group is indeed expected, as the model surface used in the simulations is perfectly homogeneous. Even in that case, the steps span a very narrow pressure range, pointing to the lack of clearly defined adsorption sites.

A look at the molecular configurations along the 100 K isotherm (Figure 3.19) indicates that the substep hinted in the 150 K isotherm at around $N \approx 200$ corre-

sponds to the formation of the monolayer. The other two dotted lines indicate the coverages corresponding to the filling of the grooves ($N \approx 30$) and the development of a bilayer ($N \approx 380$). However, these features are not discernible in any of the higher temperature simulated isotherms, in agreement with the experimental findings of the Migone group[14] in the 150-200 K temperature range.

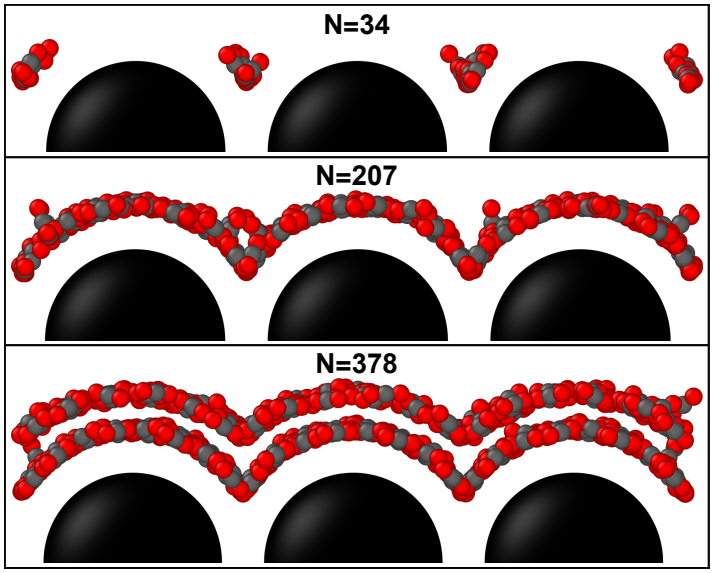


Figure 3.19: Cross section of the low-temperature (T = 100 K) configurations corresponding to the coverages indicated with the dotted lines in Figure 3.18

An upper estimate for excess coverage effects (Eqn. 2.31) was calculated using the accessible volume given by the difference between the simulation cell volume and volume occupied by 3 closed nanotubes of radius 6.78 Å, ($V_g \approx 281628$) Å$^{-3}$. At the highest coverages and pressures, the excess coverage correction is less than 4% and will therefore be neglected.

The triple point temperature for carbon dioxide is 216.6 K. All simulated isotherms were conducted below this temperature, such that saturation corresponds to solid-vapor coexistence. The isosteric heat of carbon dioxide will then approach a value

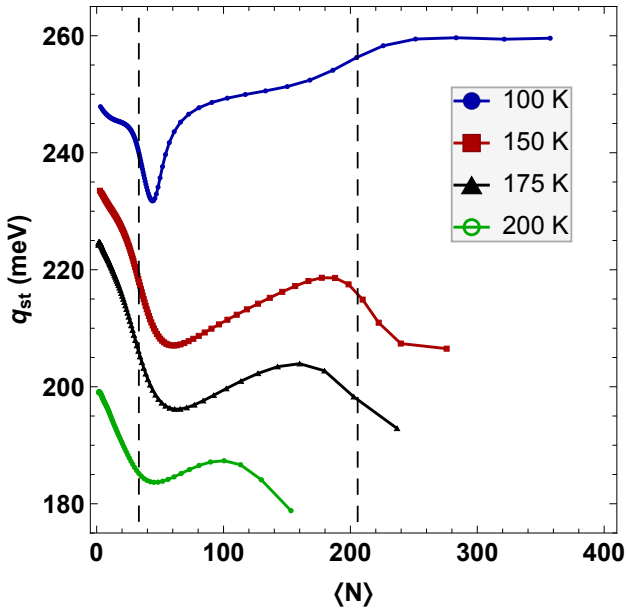


Figure 3.20: Isosteric heat of adsorption corresponding to the simulated isotherms. The dotted lines indicate the filling of the groove at low coverage ($N \approx 35$) and the monolayer completion ($N \approx 200$). As discussed in the text, the decreasing trend observed at the highest loadings for the three higher temperatures (T ¿ 150 K) is an artifact of the simulations for CO2 adsorption.

corresponding to the latent heat of sublimation (278 meV)[78] at high coverage for the temperatures considered in this study.

In Figure 3.20, the isosteric heat values as a function of the number of adsorbed molecules for each simulated isotherm are shown as calculated using Equation 2.28. As with the isotherms, there is an absence of distinguishable adsorption sites with characteristic energies (plateaus) in the isosteric heat curve. To understand this dependence, Figure 3.21 shows the energy per molecule as a function of coverage at the lowest temperature. At low coverage (when there are roughly 10 to 30 molecules adsorbed in the grooves), it is possible to recognize a region of nearly uniform isosteric heat only at the lowest temperature ($T = 100$ K). At higher temperatures, in this

same low-coverage range, the isosteric heat decreases steadily, indicating a dominance of entropic effects. The first vertical dotted line at $N \approx 35$ indicates the coverage at which the groove is fully filled and most of the molecules start to change their orientation to lie perpendicular to the groove and on the outer surface of the adjacent tubes. This produces a drastic reduction in the strength of the gas–surface interaction (as can be seen in Figure 3.21) that is most notable at the lowest temperature.

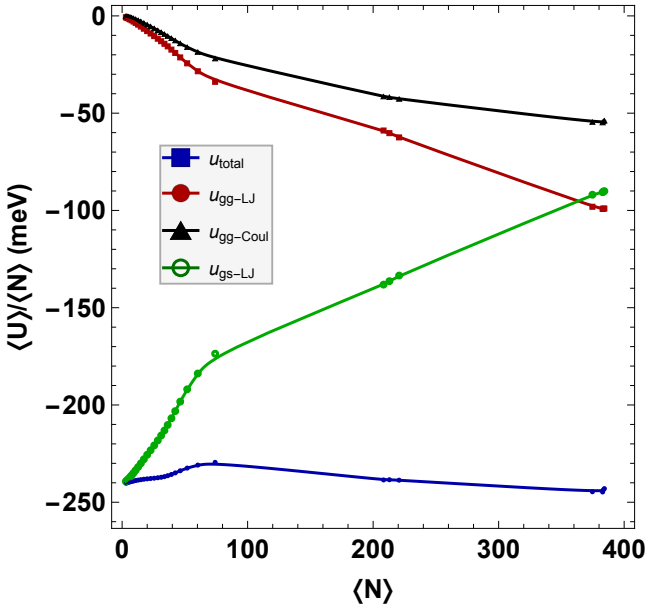


Figure 3.21: Energy per molecule as a function of coverage at 100 K; the total energy (blue line) is the sum of the gas–surface (green) and the gas–gas (red and black) contributions.

As the coverage increases, the gas–surface interaction keeps getting weaker, as expected, but the corresponding increase of the total gas–gas interaction for $CO_2$ (the LJ and the electrostatic components combined) overcomes this reduction causing the overall isosteric heat to increase as the monolayer phase develops. This is in striking contrast to what has been observed for many other adsorbates where the increase in the molecular interaction energy is typically not enough to make up for the loss of the

gas–surface interaction. The difference for $CO_2$ results from the contribution of the quadrupole–quadrupole interaction, which is not present for the other gases; although the magnitude of the LJ contribution is comparable to that of other adsorbates of similar size, the electrostatic energy is almost as large as the LJ energy, giving rise to gas–gas interaction energies that are roughly twice as large as those for other adsorbates.

The distinctive effect of the quadrupole–quadrupole interaction on the isosteric heat dependence with coverage is clearly demonstrated in Figure 3.22 where the isosteric heat is decomposed into individual components from each type of interaction, at 100 K. The dotted line, which does not include the contribution from the quadrupole–quadrupole interactions, follows the decreasing trend characteristic of simple LJ gases with no electrostatic interactions.

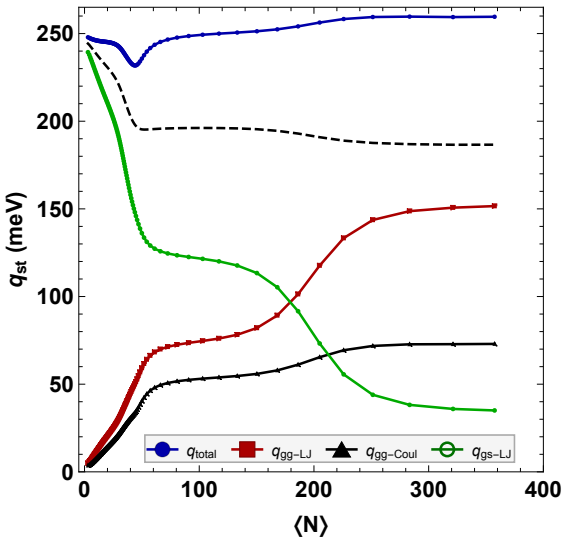


Figure 3.22: Individual contributions to the total isosteric heat at 100 K (blue curve) originated from each kind of interaction (green, red, and black, full lines); the increasing trend of the total isosteric heat (blue curve) contrasts with the decreasing function (dotted curve) that would be obtained if there were no electrostatic interactions.

After monolayer completion, the isosteric heat keeps increasing, slowly approaching the bulk value as a second layer forms. In the simulation, this can only be seen at the lowest temperature (see Figure 3.20). For higher temperatures, it becomes increasingly more difficult to ensure that the system is at equilibrium for the higher coverage phases because the interaction energy values strongly depend on the relative orientation of the molecules due to the quadrupole interactions. Slight deviations in orientation (because of thermal effects and/or variations in the external potential) produce relatively large changes in energy, making it much harder for the system to reach the equilibrium configurations (and hence energies) at high coverages. Once again, this is not the case for other adsorbates that only interact through LJ potentials. Therefore, the final decrease in isosteric heat for the higher temperature curves are considered to be an artifact of the simulations, indicating a clear limitation of this approach for simulating $CO_2$ adsorption under these specific conditions (deposition of a high density phase). It is emphasized that this difficulty does not occur when the same approach is used to simulate LJ gases (with no electrostatic interactions) or even when simulating $CO_2$ at lower coverage. In Section 3.1.2, the same molecule–molecule interactions were able to reproduce the correct bulk phase as well as the monolayer phase on graphite with no trouble. These results, which provide an internal consistency test, rule out problems with the potential used resulting from the choices made for the values of the parameters. Indeed, a top view of the monolayer configuration (Figure 3.23) reveals the typical T-shape orientations of the two-dimensional phase of $CO_2$.

In general, there is good agreement with the simulated low temperature isosteric heat curve and the experimental isosteric heat from the Migone group[20]. While an

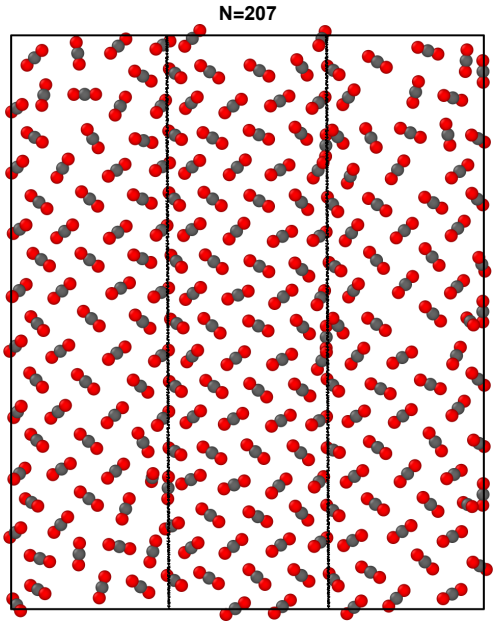


Figure 3.23: Top view (xy plane) of the monolayer phase at T = 100 K. The vertical lines indicate the location of the grooves between two tubes.

exact correspondence between the simulated and experimental loading scales is not possible, it can be estimated that $N \approx 200$ in the simulations corresponds to 6500 cc-Torr for the experiments. This deduction is based on the the molecular configurations from the simulations, which show the completion of the monolayer at about $N \approx 210$ (see Figures 3.18 and 3.23) and the experimental surface area determination that monolayer completion occurs at about 6500 cc-Torr. In the simulations, the isosteric heat values increase from the initial stages of monolayer formation ($N \approx 100$ in Figure 3.20) to the bulk value. Experimentally, the isosteric heat curve trends very similarly in the corresponding coverage range. Separate experimental measurements by Bienfait *et al.*[17] also agrees with the trend of the isosteric heat through a minimum, where a value of about 250-255 meV is reported at the monolayer coverage (this value is slightly below the isosteric heat value on graphite at 120 K, 262 meV). From the

simulations, at monolayer coverage for $T = 100$ K, the isosteric heat is 250 meV. Bienfait *et al.* report a value of 230 meV at 124 K. Overall, this constitutes rather good quantitative agreement between simulations and experiments near monolayer loading. Moreover, the value at the bilayer coverage in the simulations, 260 meV, also agrees with the experimental value of 262 meV found by Migone *et al.*.

At low coverage, as the grooves are being filled ($N < 30$), the isosteric heat values found in the simulations decrease with loading (Figure 3.20). The values measured experimentally at the lowest loading by Migone *et al.* are also a decreasing function of loading. The main difference between the simulations and the experimental results is that the values of the isosteric heat measured at very low loadings (less than 1000 cc-Torr) are much higher ($\sim$ 55 meV) than those obtained in the simulations. Experimentally, it is very likely that in the low-coverage region, the $CO_2$ molecules are adsorbing on the small number of impurities that are present in the sample and/or in the few, wider interstitial channels that may be present in the sample (as a result of stacking defects in the bundles). Either one of these alternatives (or both) will lead to the high isosteric heat values measured in the experiments. The sorbent in the simulation is perfect, and there are no impurities present; this accounts for the differences observed in this loading region.

## 3.4 Features of Adsorption

In Sections 3.2 and 3.3, realistic material models were utilized to study gas adsorption on specific systems with unique experimentally observed behavior. For the case of ethane, the lack of distinct substeps in the isotherm data is a result of the

binding location as well as the adsorbate's rotational degrees of freedom. For carbon dioxide, the unique isosteric heat behavior was found to be directly related to the gas-gas interactions. Understanding the interplay between the defining properties of an adsorbate/adsorbent and the ultimate adsorptive behavior of a given system is of general interest. To this effort, this section compares and contrasts how the isotherm and isosteric heat as a function of coverage depend on different model surfaces as well as adsorbate gases. Specifically, the adsorption of Ar, $CO_2$, and $C_2H_6$ on several nanotube bundle models is investigated.

### 3.4.1 Modelling and computer simulations

GCMC simulations were conducted to explore the equilibrium adsorptive behavior of Ar, $CO_2$, and $C_2H_6$ on the external surface of a carbon nanotube bundles. Several bundle models were considered:

- Parallel Array of 2 or 3 Tubes (e.g. Figure 3.17)
- Triangular 3 Tube Bundle (e.g. Figure Figure 3.24)
- Triangular 9 Tube Bundle (e.g. Figure Figure 3.24)

Where the 3 and 9 tube bundles are depicted in Figure 3.24. Homogeneous and heterogeneous bundles are investigated, where nanotube diameters sizes include: 8.137 Å $(6,6)$, 9.493 Å $(7,7)$, 12.206 Å $(9,9)$, 13.562 Å $(10,10)$.

As in Section 3.3, the parallel array simulation cell is periodic along both the length of the tubes and the direction separating the tubes. This effectively simulates an infinite array of nanotubes. While the simulations carried out on the bundles comprised of 3 and 9 nanotubes have cells that are periodic along the length of the

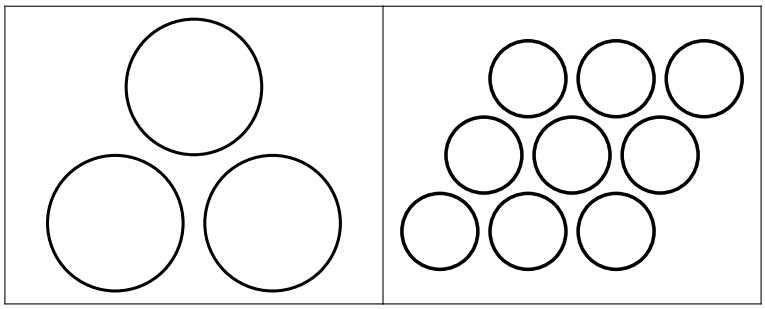

Figure 3.24: Top view of nanotube bundles comprised of 3 (left) and 9 (right) continuous nanotubes with carbon density 0.38 $Å^{-2}$ and wall to wall separation of 3.2 Å.

tubes, they are isolated such that the remaining dimensions have fixed or non-periodic boundaries.

The procedures utilized in Sections 3.2 and 3.3 are again employed to generate adsorption isotherms from a series of runs at fixed temperature as well as to generate isosteric heat curves as a function of coverage. Each point on the adsorption isotherm is calculated using a GCMC run of up to 2-4 $\times 10^9$ steps to bring the system into equilibrium and to calculate averages, depending on the sorbate and sorbent. MC steps are composed of a trial creation, destruction, or displacement move with attempt probabilities of 0.3, 0.3, and 0.4, respectively. For molecular adsorbate species, displacement moves are separated into displacement of the center of mass (with probability of 0.2) and rotational about the center of mass (with probability of 0.2). The maximum displacement and rotation step sizes are dynamically adjusted during the equilibration phase to achieve move acceptance values of 50%.

Gas-gas interactions are modelled as discussed in Section 2.1.2 with potential parameters given in Table 2.1. The gas–substrate interactions are modelled using a Lennard-Jones potential using the continuous carbon approximation with an effec-

tive carbon surface density of 0.38 $Å^{-2}$ and wall to wall separation of 3.2 or 3.4 Å. Both open and closed nanotube varieties are used, where open nanotubes provide an additional strong binding site region in the internal region of the tube.

### 3.4.2 Results and Discussion

**$C_2H_6$ on Closed and Open 3 tube bundles**: A potential energy surface (PES) calculation was performed to investigate the energetic properties of the various tube bundle models and the results are presented in Figure 3.25. These figures were generated using the methods discussed in Chapter 2.2, where a series of single point energy calculations were used to find the energy at each grid point. The minimum energy orientation is known, and occurs when the molecular axis oriented along the length of the tubes comprising the bundle. As depicted in 3.25 b and d, open nanotubes present three distinct adsorption sites: (1) In the inner region of the tubes, (2) the groove sites on the exterior between adjacent tubes, and (3) the external surface of the tubes. For closed tubes (3.25 a and c), the inner tube region is not accessible. Generally, the internal pore site presents the lowest (strongest) energy binding sites, followed by the groove and external surface sites. The strength of the binding in the inner pore region is observed to decrease as the radius of the nanotube increases. Externally, the opposite trend is observed as the decreased curvature with increasing radius serves to slightly increase the strength of the groove and external sites.

A set of adsorption isotherms obtained from the simulations are presented in Figure 3.26 for the homogeneous three tube (7,7) bundles of open and closed varieties. For the open tubes, three isotherm steps are observed which correspond to adsorption in the three distinct site types. The lower step, occurring at $N \approx 30$ corresponds to

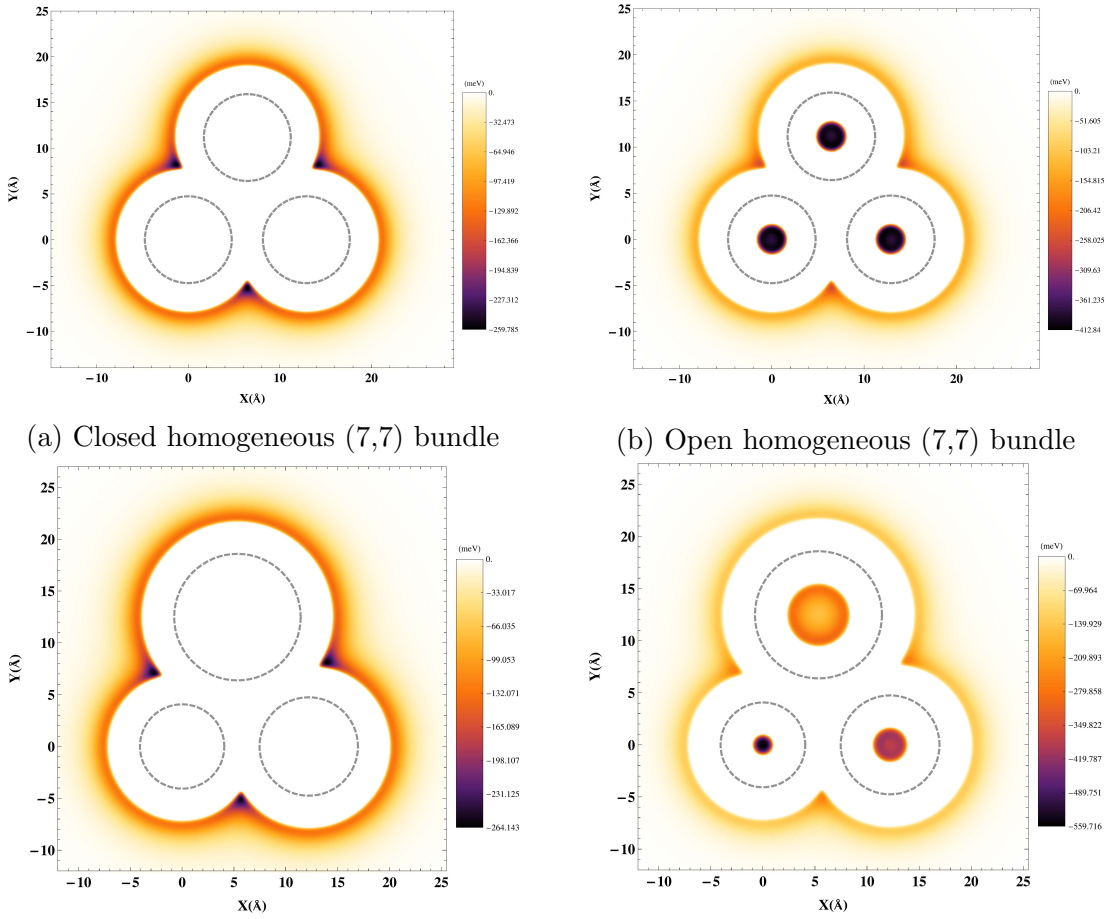


(a) Closed homogeneous (7,7) bundle

(b) Open homogeneous (7,7) bundle

(c) Closed (6,6), (7,7), (9,9) bundle

(d) Open (6,6), (7,7), (9,9) bundle

Figure 3.25: Potential Energy Surface plots for an ethane molecule on various three tube nanotube bundles.

the filling of the internal regions of the three tubes. The next step, is the filling of the groove sites at $N \approx 50$, and the final step at $N \approx 200$ corresponds to the completion of a monolayer on the exterior of the tubes. The isotherms for the closed tubes follow a similar trend, with the absence of the lower step corresponding to the lack of internal pore region. Generally, as the temperature is increased, the sharp step features are observed to smooth out.

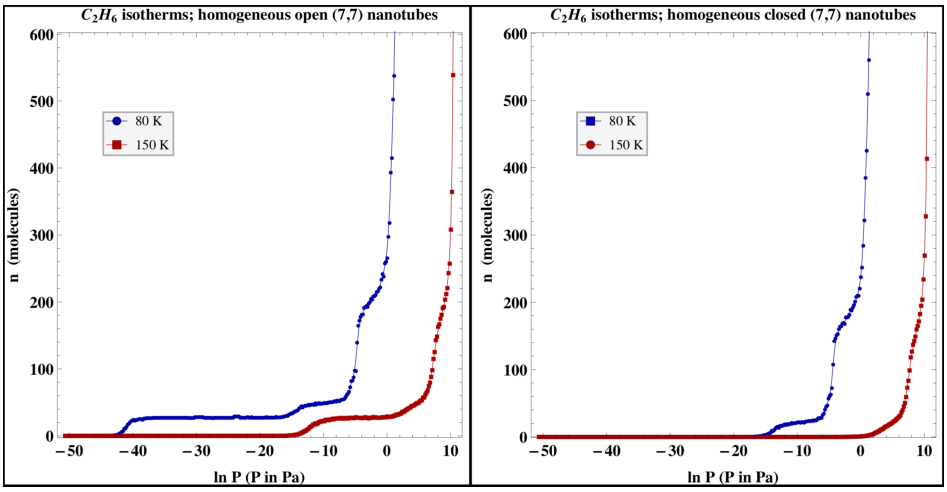


Figure 3.26: Adsorption isotherms from the simulations for ethane on a three tube (7,7) open (left) and closed (right) bundle.

Figure 3.27 depicts the adsorption isotherms for the heterogeneous three tubes bundles. At the lowest temperature for the open variety, 5 distinct steps are now observed which correspond to the three different internal pore regions and the external groove and nanotube surfaces. In comparing with the higher temperature curve, these three distinct steps in the inner pore are smoothed together, as the lower energy molecular orientations are no longer obtained at equilibrium for high temperatures. Comparing the closed variety for the heterogeneous and homogeneous bundles, the step height corresponding to the monolayer completion is larger for the heterogeneous case. This is consistent with the larger effective external surface area due to the (9,9) nanotube. The steps occur around the same pressure value indicating consistent energy profiles for the external sites, as expected given the PES data of Figure 3.25.

Isosteric heat curves as a function of coverage for the three tube bundle systems are show in Figure 3.28. The orange dashed lines are a guide to the eye and represent adsorption on distinct sites. For all bundle models and all temperatures the high cov-

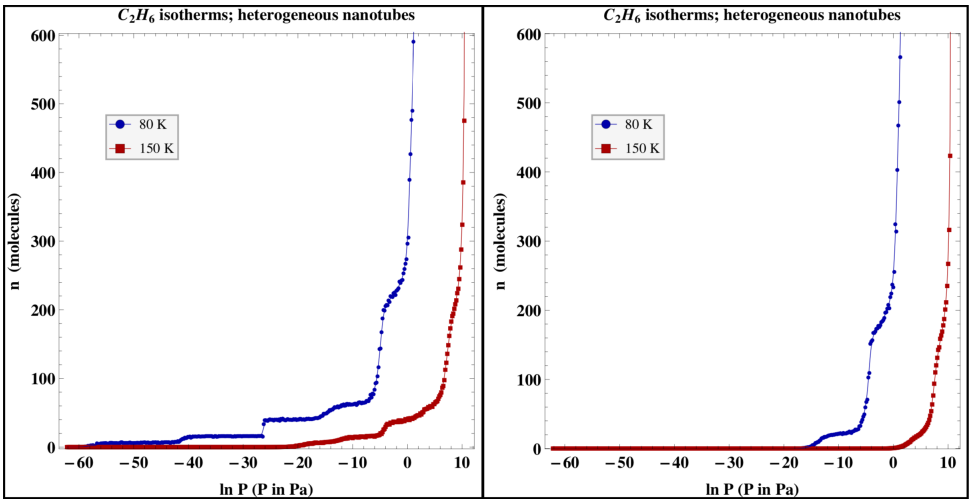


Figure 3.27: Adsorption isotherms from the simulations for ethane on a three tube (6,6), (7,7), (9,9) open (left) and closed (right) bundle.

erage isosteric heat is shown to be monotonically decreasing and approaches the latent heat corresponding to the bulk phase; here that is the latent heat of vaporization. Generally, the lower temperatures curves are higher in energy due to entropic effects that cause the molecules to not reach an energetically optimal equilibrium configuration. Both closed bundle models (Figure 3.28 a and c) show similar behavior with two plateau regions corresponding to adsorption in the groove sites and the external walls of the nanotubes. The monolayer completion corresponds to the second wider and lower energy plateau. The open heterogeneous bundle (Figure 3.28 d) depicts adsorption in 5 distinct sites as indicated with the dashed orange lines. These correspond to the five adsorption sites discussed in the corresponding PES (Figure 3.25 d) as well as the steps in the corresponding adsorption isotherm (Figure 3.27). As the internal nanotube sites are filled, the isosteric heat shows an increasing tendency as compared to the relatively flat behavior as the external sites are filled. This can be attributed to increased gas-gas interactions in the confined internal pore regions.

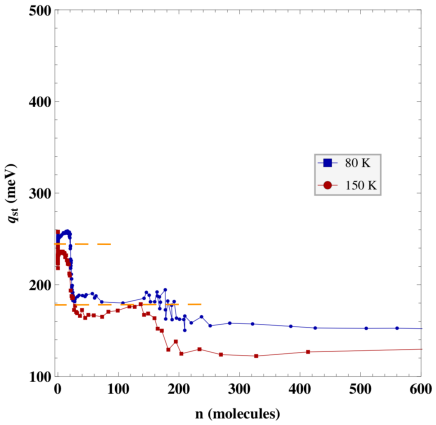


(a) Closed homogeneous (7,7) bundle

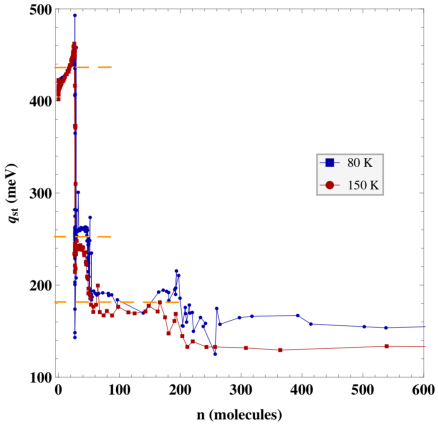


(b) Open homogeneous (7,7) bundle

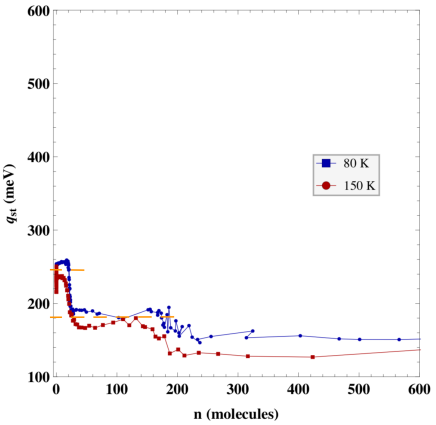


(c) Closed (6,6), (7,7), (9,9) bundle

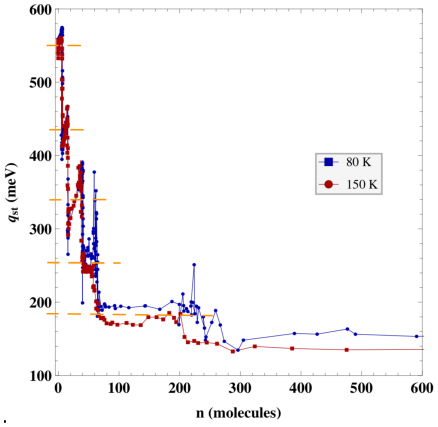


(d) Open (6,6), (7,7), (9,9) bundle

Figure 3.28: Isosteric heat as a function of coverage for the adsorption of ethane on three tube nanotube bundles. The dashed lines indicate adsorption in distinct sites.

A bundle represented as a parallel array of nanotubes was also considered, similar to the adsorbent system of Section 3.3. Here, the parallel array simulation cell consists of two closed tubes of radius 5 Å (closest to (7,7) tubes). For this system, the strength of the gas-gas interactions ($\epsilon$) was increased by $\sim 12\%$ above the value used for all other ethane simulations as reported in Table 2.1. The isotherm and isosteric heat curves as a function of coverage for a range of temperatures are shown in Figure 3.29. Low temperature isotherms and isosteric heat curves depict two distinct steps and

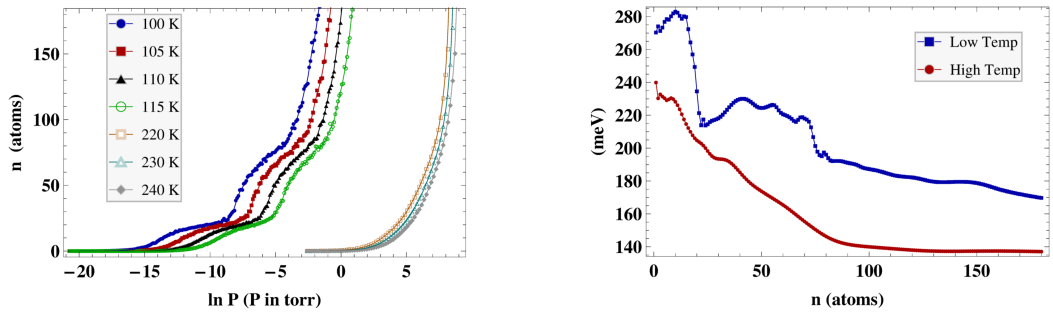


(a) Isotherms on parallel array

(b) Isosteric heat on parallel array

Figure 3.29: Adsorption isotherms and isosteric heat as a function of coverage for ethane on a parallel array of nanotubes.

plateaus corresponding to the filling of the groove region and the external surfaces of the nanotubes (monolayer), similar to the results for closed bundles (Figure 3.28). The increase in energy observed for in the isosteric heat is attributed to the increased strength of the ethane interaction parameter $\epsilon$.

**Ar on Open 3 tube bundles**: The adsorption of Argon on the three tube homogeneous (7,7) bundle was investigated to provide a point of comparison between molecular adsorbate species which have additional degrees of freedom through their ability to rotate. Adsorption at 50 K was considered and the resulting isotherm and isosteric heat, as a function of coverage, is presented in Figure 3.30. In comparison with the closed homogeneous bundle for ethane adsorption (Figures 3.26 and 3.28), three steps in the isotherm and three plateaus in the isosteric heat are observed, corresponding to adsorption in the strongest to weakest binding sites (internal tubes, groove sites, external nanotube surfaces). The additional degrees of rotational freedom in the case of ethane do not appear to have an impact in regards to causing an intrinsic spread in the binding energies. Despite the high curvature associated with

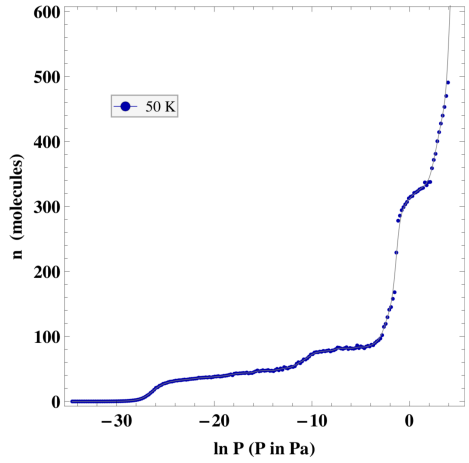


(a) Isotherms on 3 Tube Bundle

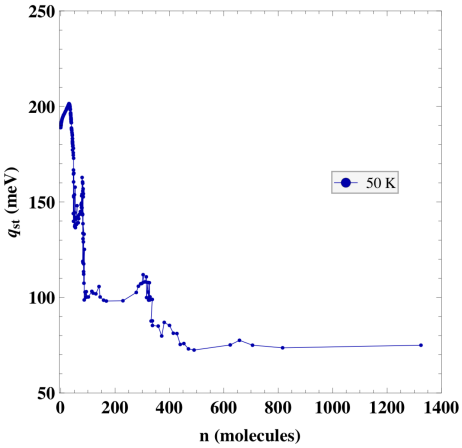


(b) Isosteric heat on 3 Tube Bundle

Figure 3.30: Adsorption isotherms and isosteric heat as a function of coverage for Argon on a 3 tube homogeneous (7,7) bundle

the (7,7) bundle, both ethane and Argon present distinct features, 2d monolayers, and the correct high coverage isosteric heat corresponding to the bulk 3D values.

**$CO_2$ on closed bundles**: Several closed nanotube bundle models were studied for the adsorption of carbon dioxide in an effort to understand how the properties of the bundles influence the isosteric heat of adsorption. Here, homogeneous bundles comprised of 3 and 9 tubes were utilized, along with the parallel array model. Tubes sizes of (7,7) and (10,10) were considered. A potential energy surface calculation was performed for the new 9 bundle model used in this section as shown in Figure 3.31. As with the other closed bundles (Figures 3.17 and 3.24), the 9 tube bundle presents two types of binding sites: (1) The groove site between adjacent nanotubes and (2) the external surfaces of the tubes. The slight increase in the binding strength in the groove site ($\sim$ 3 meV) as compared with the parallel array of tubes is due to the presence of additional tubes in the simulation cell.

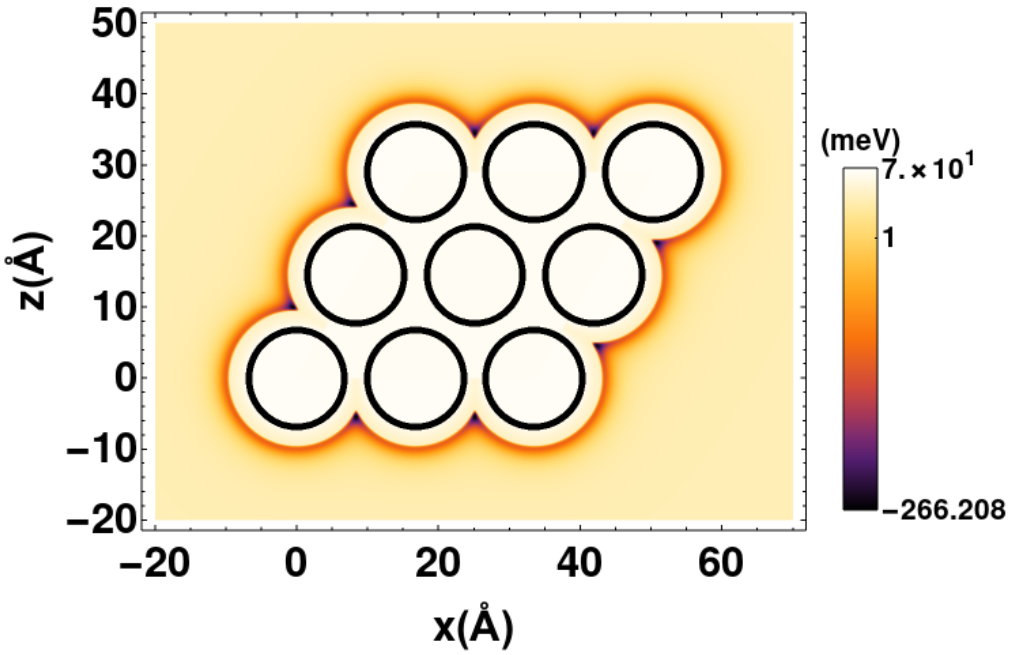


Figure 3.31: Potential Energy Surface calculation for a $CO_2$ molecule interacting with the a 9 tube homogeneous (10,10) nanotube bundle

The behavior of the adsorption isotherms and isosteric heat as a function of coverage are shown for several nanotube bundle systems at 100 K in Figure 3.32. Here all of the isotherms, except the parallel tube model ($2 \parallel (10, 10)$), lack clearly define steps. This is in direct contrast with the the adsorption of both Ar (Figure 3.30) and $C_2H_6$ (Figures 3.26 and 3.27) where distinct steps are observed corresponding to the filling of the groove sites and the completion of the monolayer on the external surfaces of the nanotubes. The distinct steps present in the isotherm of the parallel tube model occur only at the formation of the monolayer and bilayer, consistent with previous parallel tube model calculations performed for $CO_2$ adsorption (Figure 3.18). The lack of sub-steps are attributed to the larger ratio of the gas-gas to gas-surface that occurs for carbon dioxide due to the presence of the quadrupole-quadrupole interac-

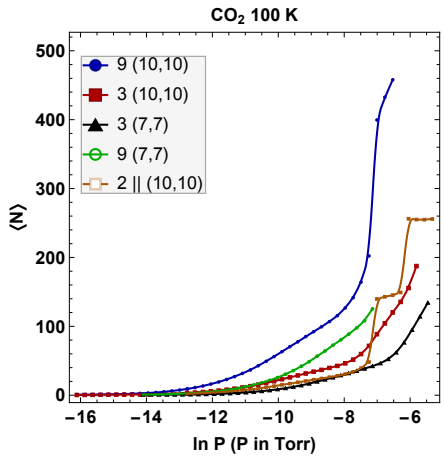


(a) $CO_2$ Isotherms

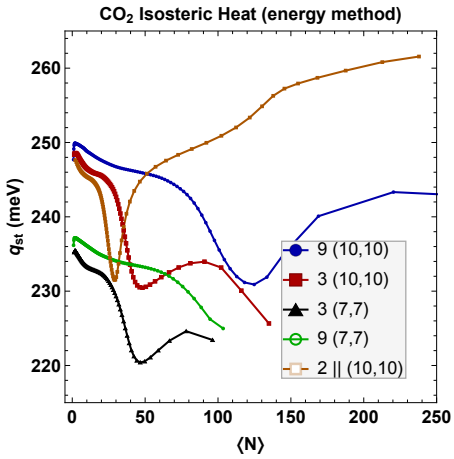


(b) $CO_2$ Isosteric Heat

Figure 3.32: Adsorption isotherms and isosteric heat as a function of coverage for carbon dioxide on several model nanotube bundles at 100 K

tion. The adsorption sites presented by the relatively weaker gas-surface interactions are less distinct in this case. This isotherm data is also consistent with the capacity differences between the bundle models, with the 9 tube $(10, 10)$ bundle adsorbing the most gas.

The isosteric heat curves in Figure 3.32 b display a clear distinction between the different tube models. The parallel tube model $(2 \,||\, (10, 10))$ and the 9 tube bundle $(9\ (10, 10))$ show similar behavior most consistent with experimental findings (Section 3.3) in that the isosteric heat does not display the monotonic decrease behavior at higher coverages. When comparing similar bundles (e.g. 9 tube bundles or 3 tube bundles) as the tube radius is increased, the isosteric heat is shifted upwards to higher energy. As opposed to the adsorption of ethane and argon on similar bundle systems, there is a lack of clearly defined plateau regions in the isosteric heat corresponding to groove and external surface adsorption sites.

As discussed in Section 3.3, the unique behavior of carbon dioxide is attributed to the presence of the quadrupole-quadrupole interaction due to its strength and dependence on the molecular orientations. For the case of other gases, such as Ar and $C_2H_6$, the isosteric heat is a monotonically decreasing function of coverage which approaches the corresponding bulk value of latent heat. The energy of the monolayer for those gases is above the value for the latent heat. For carbon dioxide, the monolayer energy is below the corresponding latent heat of the bulk phase.

The sensitivity of the interactions to orientation is displayed in the isosteric heat curves. The parallel array of tubes, which is an artificial construct and does not appear experimentally, let the $CO_2$ molecules arrange in a configuration closer to the experimental monolayer. The 9 tube $(10, 10)$ is the next best choice, when comparing to experiment, given the smaller curvature associated with the large tube radius as well as the length of the sides of the bundle (Figure 3.31). For the other bundle systems, the curvature of the tubes and/or the size of the bundle prohibits the formation of a monolayer and bulk phase with the required structure which would cause the characteristic increase of isosteric heat at higher coverage. This is further supported by adsorption simulations carried out on a planar graphite surface represented by a continuous plane of carbon (see Appendix B) at 120 K. The isosteric heat for coverages up to a monolayer are shown in Figure 3.33. This result compares well with the experimentally reported value of 262 meV at 120 K[20] on graphite. These results indicate that the correct behavior for carbon dioxide on an explicit nanotube bundle could be reproduced via simulations on much larger tube bundles.

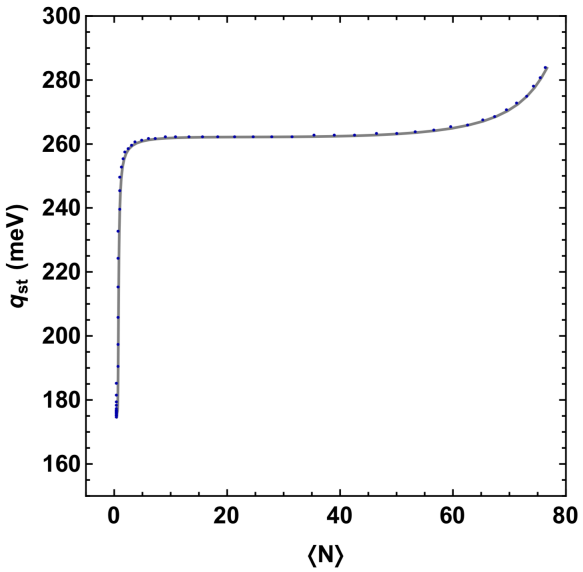


Figure 3.33: Isosteric heat as a function of coverage for $CO_2$ adsorption on graphite at 120 K.

# Chapter 4

# Results - Kinetics

While the study of adsorption using equilibrium Monte Carlo methods has proved extremely useful, the scope is clearly limited. In order to form a comprehensive and fundamental understanding of the processes at play, the evolution of the system from initial to final (equilibrium) state must also be studied. From a practical standpoint this information, such as the time it takes the system to reach equilibrium, is of critical interest. As discussed in Chapter 2, standard deterministic methods are simply unable to directly probe the time scales necessary to study adsorption. We therefore turn to dynamical stochastic methods to study the time evolution of adsorption with Kinetic Monte Carlo as discussed in Chapter 2.4.

This chapter summarizes a general 3D on-lattice KMC modelling scheme that was developed with a customized version of the open source SPPARKS[30] code (see Chapter 2.5) to investigate the kinetics of adsorption in materials that may present complex, inhomogeneous geometries and/or interaction profiles. This scheme, as visualized in Figure 4.1, is comprised of the definition of a lattice, adsorption species,

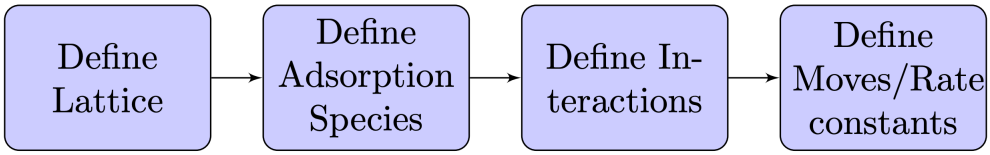


Figure 4.1: 3D KMC Scheme Flowchart

interactions, and the rate constants for possible moves. A specific model, developed to study adsorption in carbon nanohorns (see Chapter 2.1.2) which motivated this work, is created under this scheme utilizing available experimental data and the results of some preliminary simulations are presented and discussed.

## 4.1 Lattice and Connectivity

A lattice within the context of on-lattice KMC is a set of points in space on which events take place. Physically, lattice points can represent the location of adsorption sites, diffusive sites, locations of atoms, etc. Lattice sites have an associated vector, which defines their state. For example, in the case of simple adsorption a lattice site vector may be a single value of 0 or 1 corresponding to its occupancy (0=empty, 1=occupied). The relationship between lattice points is defined by their location and connectivity. The connectivity of the lattice defines the list of sites that can mutually participate in multi-lattice site events. For example, the diffusion of an atom from one lattice site to another can only occur between two sites that are appropriately connected.

Traditionally, the definition of this lattice and associated connectivity in our lab has been restricted to 1 or 2 dimensions. One reason for this is that any modification to the lattice structure required significant changes to the previously used KMC

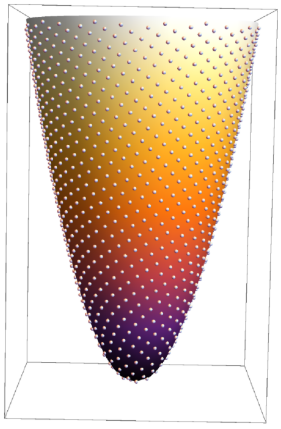

Figure 4.2: Lattice on a paraboloid surface

source code in order to accommodate the associated change in moves, energies, connectedness, etc. Within this scheme, with the modified SPPARKS code, the lattice and its associated connectivity are treated as inputs and can be easily generated without any source code modifications. This flexibility allows for much more rapid structural model development and testing.

By default, the original SPPARKS source code can automatically generate several lattice types including: 1D line (2 neighbors), 2D square (4 or 6 neighbors), 2D triangular (6 neighbors), 3D square (6 or 26 neighbors), 3D BCC (8 neighbors), 3D FCC (12 neighbors). Outside of this, a lattice generation tool has been created to construct additional lattices with customized shapes and connectedness, such as the cylindrical lattice defined in Figures 2.2 and 2.3. In addition, the lattice generation tool can pattern any parameterized surface with a Fibonacci lattice[77] and automatically generate the list of neighbor sites (connectedness). An example of this is demonstrated for the surface of a paraboloid in Figure 4.2.

## 4.2 Adsorbate Species

In the modified SPPARKS code, the adsorbate species is represented in an abstract manner via the state of a lattice site. These lattice state vectors encode the type of the occupying gas species, the lattice site type, the environment around the site (for interactions), and possible allowed moves. While currently only single and binary monatomic species are fully supported, the design choice of using lattice state vectors allows for straightforward extension to gaseous mixtures of any size, even including polyatomic gases. The ability to easily adjust the number and type of gas species at run-time in a KMC simulation is highly desirable in our lab group, as previously such changes would require significant changes to the in-house KMC source code.

## 4.3 Interactions

A general representation of the gas-gas and gas-surface interactions was chosen to provide maximum model flexibility, which was not a feature in the previous KMC code used in the group. The functional form of the energy of an occupied lattice site is given by,

$$E_i = \epsilon_{b_i}(x, y, z, type, species, \vec{g}) + \epsilon_{int}(x, y, z, species, \vec{g}) \tag{4.1}$$

where $\epsilon_{b_i}$ is the binding energy associated with the gas-surface interactions which can vary depending on the lattice site type, the occupying species, the location of the lattice site, as well as the state of the environment around the site which is defined by the vector $\vec{g}$. The gas-gas interactions, $\epsilon_{int}$ are a function of the position in the

lattice, the occupying species, and the state of the environment around the site. By taking into account the state of the local environment, non-pairwise effects can be included when necessary[79].

In practice, the environment dependent interactions are generated during the construction of the lattice where an energy is assigned to every possible combination of the neighboring sites as defined by the site connectivity and the number of gas species being simulated. For example, in a simulation comprised of a single species where each lattice site has 4 neighbors with a single state value (empty or occupied) there will be $2^4$ energies corresponding to all the possible neighbor configurations. For the case of simple pairwise gas-gas interactions, the energy will be proportional to the coordination of the lattice site.

The ability to vary the binding and interaction energy throughout the position of the lattice served as the initial motivation for the development of this general on-lattice KMC modelling scheme. Specifically, it was the interest to study the kinetics of adsorption in carbon nanohorns which have a binding energy profile that increases in strength moving deeper into the conical pore region. This energy variation is depicted in Figure 4.2, where the coloring corresponds to the lattice site binding energy (darker colors represent stronger binding). The described interactions in Eqn.4.1 can be used to study many different complex adsorbent materials without requiring changes to the underlying source code.

## 4.4 Moves and Rates

Adsorption, desorption, and diffusion moves are built into the modified SPPARKS code. The allowed moves for a given site are defined by its current occupied state, type, and the surrounding environment. Any lattice site in the system can be designated as an adsorption/desorption type at run-time, which allows for maximum flexibility during model development and testing. The lattice connectivity defines the list of neighboring sites to which an atom could hop/diffuse. Currently, only single hop diffusion type events are supported.

The rate constants, which define the probability that events will occur (Section 2.4), can be set at run-time. This ability is very useful for both investigations of real materials, where the pre-exponential factors may require adjustment in accordance with experimental data as well as general kinetic investigations where it is important to understand the effect of the ratios of the rate constants.

## 4.5 General Benefits of SPPARKS

The selection of SPPARKS to serve as the base code for the general on-lattice KMC scheme developed to study adsorption was based on several factors. Firstly, SPPARKS is modular by design which allows for the straightforward addition of features and functionality. The modifications for the present scheme are discussed in the previous sections of this chapter and listed in Section 2.5. SPPARKS is written in c++ and designed to perform efficiently at scale by computational scientists and software engineers at Sandia National Laboratories and the US Department of Energy. Several KMC solvers are available within SPPARKS: linear style $O(N)$[80, 81],

tree style $O(LogN)$[82], and group style $O(1)$[83], where the scaling refers to the computational cost to pick an event to perform out of $N$ total events. The computational efficiency of the tree and group style solvers allow for much larger (number of lattice sites and number of species) systems to be simulated. Although not yet utilized in the current scheme, a parallel KMC algorithm is implemented in SPPARKS using distributed memory parallelization via the message passing interface (MPI)[30]. This parallelization would further enable the ability to simulate larger systems and obtain results in a shorter amount of wall-time. The parallel algorithm is accomplished by decomposing the system in such a manner that multiple events are executed simultaneously in disconnected regions. The parallel algorithm is an approximation, with an accuracy that depends on the specifics of the system connectedness and interactions, as well as how frequently event information is communicated between different processors.

## 4.6 Results and Discussion

The purpose of this section is to demonstrate the usefulness and applicability of the developed scheme through the preliminary investigation of an adsorptive system. Gas adsorption of a monatomic species is studied in a 3D pore geometry designed to capture the essential feature of the nanohorn conical pore; the variation of the binding strength along the length. The lattice structure, connectivity, and energy function for this system are discussed in Chapter 2.1.2.

Several cases, defined mainly by their binding energies, were considered as summarized in Table 4.1 where dimensionless energy values are used with $\epsilon = E/k_BT$.

| Case No. | $\epsilon_{b_{outer}}$ | $\epsilon_{b_{center}}$ | Ends Open | $W_{i\to j}$ |
|---|---|---|---|---|
| 1 | -3 | -3 | 2 | $e^{\epsilon_i}$ |
| 2 | -3 | -1 | 2 | $e^{\epsilon_i}$ |
| 3 | -3 | -3 | 1 | $e^{\epsilon_i}$ |
| 4 | -3 | -1 | 1 | $e^{\epsilon_i}$ |
| 5 | [-1,-3] | [-0.5,-1] | 1 | $e^{\epsilon_i}$ |
| 6 | [-1,-3] | [-0.5,-1] | 1 | $e^{-\epsilon_j}$ |

Table 4.1: KMC parameters for the simulated cases

Here the $\epsilon_{b_{outer}}$ is the binding energy associated with the 4000 sites on the outer portion of the cylindrical pore and $\epsilon_{b_{center}}$ is the binding energy of the central line of 500 sites. Energy values of the form $[E_i, E_f]$ represent a linear variation of binding energies from $E_i$ at $z = 0$ to $E_f$ at $z = L$ (along the length of the tube). For example, in Case 5, the outer site binding energy is varied linearly along the length from an initial value of -1 at the top of the pore to a value of -3 at the bottom. Occupied sites can diffuse or jump to vacant nearest neighbor sites with a rate constant given by $W_{i\to j}$. For cases with 2 ends open, the 18 total sites in the top-most and bottom-most are eligible for adsorption and desorption events. For cases with a single end open, only the topmost layer of 9 sites are open to adsorption/desorption.

The KMC algorithm (Chapter 2.4) is executed for each case starting from an empty lattice until equilibrium is reached (the coverage no longer changes as a function of time). Each case is run multiple times with an increasing value of the chemical potential such that a range of equilibrium coverages are explored. As a matter of computational convenience, the chemical potential is assigned according to the expected equilibrium coverage value for a 2 state system with a single binding energy in the grand canonical ensemble,

$$\mu = \epsilon - \ln\left(\frac{1-N}{N}\right) \tag{4.2}$$

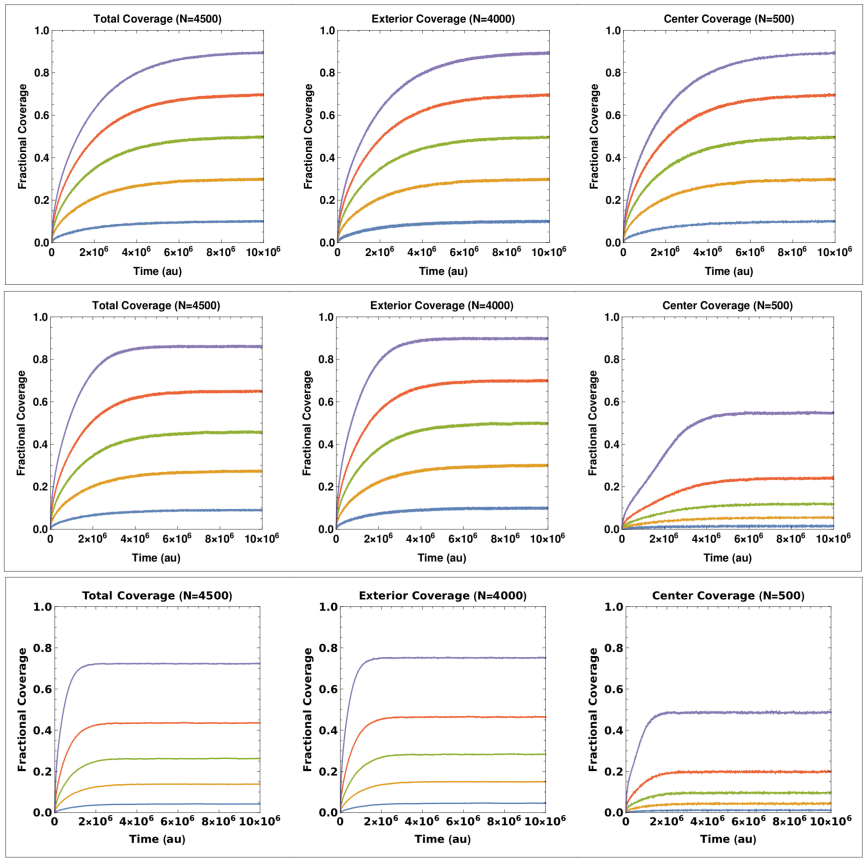


Figure 4.3: Fractional lattice coverage as a function of time for case 3 (top), case 4 (middle), and case 5 (bottom). Curves of the same color correspond to the same chemical potential value, where higher coverages correspond to simulations with larger values.

where $\epsilon = -3$ for all considered cases and $N$ values of 0.1, 0.3, 0.5, 0.7, and 0.9 are used. To increase statistical sampling each simulation case at a single chemical potential value consists of 60 individual runs differing only by an initial random seed value. The results of each run are combined by averaging the simulation state at defined temporal intervals.

The fractional coverage as a function of time obtained from the simulations for cases 3, 4, and 5 are presented in Figure 4.3. The coverage curves for case 3, which

corresponds to the system with homogeneous binding site energies, are shown to take the longest time to achieve equilibrium (no change in coverage) for a given chemical potential. When inhomogeneous binding is introduced (in cases 4 and 5), the time to reach equilibrium coverage is decreased, with case 5 being the fastest to reach equilibrium for all values of chemical potential considered. There is also a marked deviation from the exponential behavior that would be expected with Langmuir kinetics[24] observed in the inhomogeneous cases. This is most evident in the center coverage plot for case 4, which displays a clear linear regime before approaching the equilibrium value. Similar behavior was observed in a computational investigation of the kinetic effects of energy heterogeneity on surfaces by Burde *et al.*[25]. The presence of weak binding sites in cases 4 and 5 results in correspondingly smaller coverage values. This is an equilibrium feature directly related to the dependence of the equilibrium coverage on the chemical potential. Case 3, which has the strongest average binding energy per site, achieves the highest total fractional coverage for the largest chemical potential value at a value of 0.9. Cases 4 and 5 reach total fractional coverage values of 0.86 and 0.72, respectively, for the same chemical potential. For case 4, this reduction in coverage is shown to occur due to the decreased occupancy of the central line (as compared to case 3) which is comprised of sites that have binding energies 3 times weaker than the outer sites. In case 5 both the outer and center sites have a decreased equilibrium occupancy as compared to case 3, again due to the presence of weaker binding sites. Cases 1, 2, and 6, which are not depicted in Figure 4.3 exhibit similar coverage trends, however, equilibrium is achieved much faster. For cases 1 and 2, this is due to the additional end being open to adsorption which increases the ability to fill the pore. For case 6, the faster overall equilibration is attributed to the

diffusion rate increase by a factor of $e^{2\epsilon}$; which allows adsorbed atoms to move out of the end sites, making them eligible for additional adsorption events, and into the pore more rapidly.

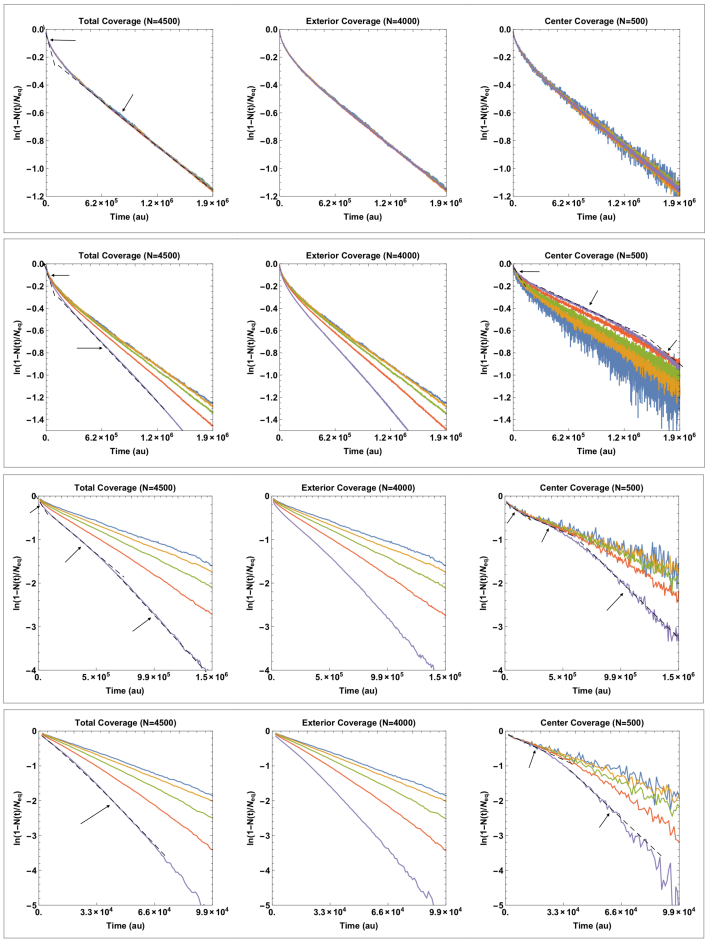


Figure 4.4: Rate plot curves in order for cases 3 (top) through 6 (bottom). Curves of the same color correspond to the same chemical potential value. Linear regions are identified with arrows and dashed line segments as a guide.

For a system defined by a single rate constant, the linear driver model[84] can be used to describe the kinetics, as given by Eqn. 2.45. Plotting the left hand side of the equation vs. time yields the rate constant as the slope. For porous systems with

multiple types of binding energies, it is not expected that a single rate constant will be able to describe the kinetics. However, plotting this rate curve and identifying the deviations from linearity and also the distinct linear regions can be useful in understanding the dynamics. If it can be expected that distinct adsorption processes take place at separate time intervals, separate linear segments should be present with an identifying rate constant. Rate plot curves for cases 3-6 are shown in Figure 4.4. As a guide to the eye, linear segments of the rate plots are marked with a dashed line and identified with an arrow. For all cases other than case 6, two linear segments can be observed on the total coverage plots with a larger rate (slope) occurring for the first segment. During this initial time period, fast adsorption occurs which corresponds to the initial filling of the open end sites. The abrupt decrease in slope corresponds to the system entering a diffusion limited phase, where the overall adsorption is slowed due to the time required for the the atoms to diffuse out into the pore. For case 6, which has a much larger diffusion rate, a single line fits the data for an extended time period. Presumably, the increased rate of diffusion allows the adsorbed atoms to quickly move out of the end adsorption sites and into the pore, without causing any blocking/slowdown. For cases 4-6, the center sites have line segments that transition from a smaller slope (slow overall rate) to a steeper slope (faster rate) at high time intervals. This change in rate can be understood in the context of a similar phenomenon observed by Burde *et al.* in their investigations of surface adsorption on sites with differing binding energies.[25] There, it was determined that the strongest binding sites reach equilibrium faster than they would in a system comprised of sites with equal binding. Similarly, the weaker binding sites took longer to reach equilibrium (as compared to the corresponding homogeneous binding system). It was found

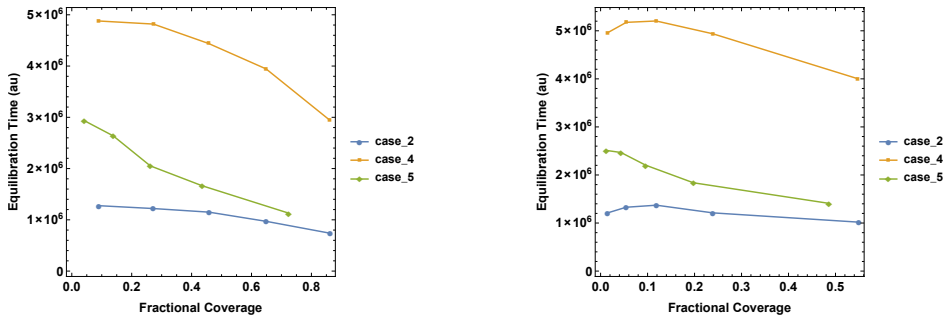


(a) Total system (b) Central line of sites

Figure 4.5: The equilibration time as a function of coverage for the total system (left) and central line (right)

that this increase in adsorption rate for the strongest sites was caused by diffusive transfer from the weaker sites. Effectively, the weaker sites offer an alternative path to adsorption to the stronger sites. Then, with this in mind for the present case, during the time period for the smaller slope, diffusion events are taking place which transfer atoms from the weaker binding central sites to the stronger binding outer sites. This period of transfer ceases when the outer sites become adequately filled, resulting in an increase of the overall rate for the filling of the center sites (increase in slope). All depicted cases except case 3 show a variation of rate constant across different values of chemical potential, due to its homogeneous binding energy profile.

The equilibration time vs coverage is shown in Figure 4.5 for the total system as well as the central line of sites for cases 2,4 and 5. This value is calculated from the coverage vs. time curves presented in Figure 4.3, where the equilibration time is defined as the time required to reach 98% of the equilibrium fractional coverage value, at a given chemical potential. All cases here, which have inhomogeneous binding, display a decrease in equilibration time with increasing coverage for the total system. This behavior is consistent with what is typically observed for the kinetics of monatomic

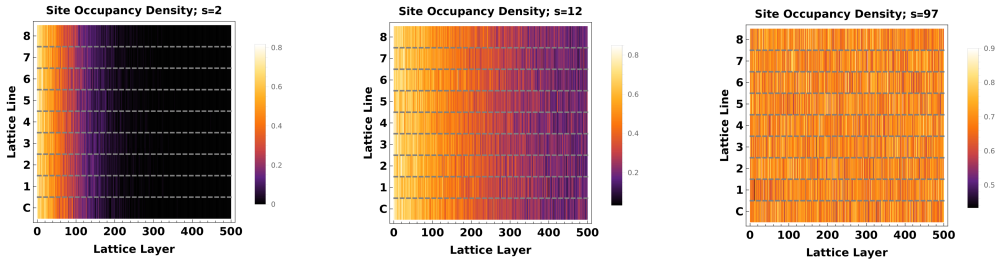


Figure 4.6: Site occupancy density plots for case 3 at successive values in time from left to right at a fixed chemical potential.

species on open surfaces or pores with no or relatively low gas-gas interactions in KMC simulations [24, 26] as well as experiment[49, 85]. This coverage dependence can be understood based on the fact that higher coverage values require correspondingly higher chemical potentials (pressures) which serves to accelerate adsorption events. When comparing sites of different energy, the weaker sites will require larger pressures to achieve a given value of fractional coverage, which again increases uptake.

The explicit dynamics of the system can be visualized using site occupancy plots at different values in time. Three such plots are visualized for case 3 in Figure 4.6 for increasing values of time moving from left to right. The vertical axis of each plot is arranged by lattice line (see Figure 2.2) where C denotes the central line of sites and lines 1-8 correspond to the outer sites. Dark colors indicate low site occupancy while lighter colors indicate sites with higher occupancy. For case 3, which has one open end and homogeneous binding, the dynamics are clear. Initially the sites closer to the open end (lattice layer 0) have a higher occupancy. As the gas diffuses into the pore the occupancy of the inner sites increase until there is a uniform occupancy across the system at equilibrium.

Figure 4.7 depicts similar occupancy density plots for case 5, which differs from case 3 in that a linear variation of binding site energies occur along the length of the

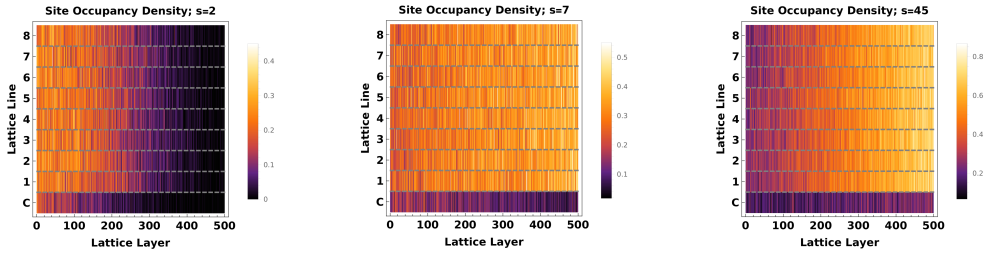


Figure 4.7: Site occupancy density plots for case 5 at successive values in time from left to right at a fixed chemical potential.

lattice and the central line of sites have weaker binding. The occupancy of the system at the earliest time (leftmost plot in Figure 4.7) shows similar behavior to case 3, in that a gradient of occupancy is observed with the most occupied sites occurring closest to the open end. Here the occupancy of the central line is lower than the outer sites (due to weaker binding), but a gradient is still observed. The system configuration at long time scales (rightmost plot in Figure 4.7) corresponds to near-equilibrium. Here, the effect of the linear variation of binding energy is apparent as the gradient of site occupancy has now shifted with the most occupied sites occurring at the bottom of the pore (lattice layer 500). This is an important first step towards investigating the difference in kinetics that occurs between nanotubes (no binding energy variation along the length) and nanohorns (binding that varies along the length). The central line of sites are also observed to lag behind the overall trend of the outer lines of sites. This can be seen in the middle plot of 4.7, where the central line of sites still show a gradient with the most occupied sites occurring near the open end, while at the same time the outer sites already have transitioned to having higher occupancy at the bottom of the pore.

# Chapter 5

# Conclusions and perspectives

The purpose of this study was to increase the understanding of gas adsorption on carbon nanohorn spherical aggregates as well as carbon nanotube bundles. In general, the identification of the key properties of a given sorbent and sorbate and the impact that they have on the adsorptive properties of the system as whole was sought. Through the development and application of structural and interaction models using computational simulations of gas adsorption, specific open questions from experiments were addressed. In addition, some general features of adsorption were identified through the controlled variation of model parameters. A general on-lattice KMC scheme was developed to enable the study of the dynamical adsorptive properties of systems previously unavailable to the group, such as those with complex geometries and interactions. The flexibility of this scheme allows for the rapid development and testing of models and parameters without the need to alter source code.

The behavior of a relatively complex adsorptive system was studied, ethane molecules on closed carbon nanohorn aggregates. This sorbent presents two main adsorp-

tion sites: (1) Strong binding sites in the internal area where the walls of individual nanohorns are close together, and (2) a weaker binding region on the outer portion of the aggregate. The molecular configurations from properly validated simulations showed that an experimentally observed quasi-plateau region in the isosteric heat curve corresponded to the majority of adsorption occurring on the exterior surfaces of individual nanohorns. The lack of sharp isotherm and isosteric heat features was found to be due to both the ability of the molecule to change orientation as well as the variation of the binding energies due to the structure of the adsorbent. Several different models were developed and explored in an effort to identify the most important defining features which govern the ultimate equilibrium adsorptive properties. In general, larger conical surfaces were found to increase the isosteric heat values as well as produce more variation over a given range of coverages. While it would be possible to design a particular structure to generate the best possible agreement with experiment, instead an exploration was performed to determine how the isosteric heat as a function of coverage depended on a particular model's structure.

The chosen interaction model for carbon dioxide was investigated to ensure the expected high coverage phase was stable with the correct energy and configuration. Using simulated annealing along with single point energy calculations, the 3 partial charge site LJ model was found to exhibit the correct structure and energy, which depended very strongly on the molecular orientations due to the quadrupole interactions. Gas adsorption of $CO_2$ was then simulated using GCMC to study the distinctive behavior that this gas was shown to exhibit in numerous experimental investigations; which includes significantly smoother isotherms with a lack of sub-steps. This characteristic was found to arise because of two supporting factors: (1) as with ethane,

the linear structure of $CO_2$ leads to a spread/broadening of the gas-surface interactions due to the available rotational degrees of freedom and (2) the larger gas-gas interactions, due to the presence of a quadrupole moment, cause $CO_2$ to be much less sensitive to any inhomogeneity in the surface such as would be present in nanotube bundles via the groove and external surface sites. Along with the behavior of the isotherm, the isosteric heat as a function of coverage for $CO_2$ on nanotube bundles was also found experimentally to exhibit contrasting behavior as compared to most simple gases. Specifically, it increases with coverage after the completion of the monolayer. By decomposing the isosteric heat into individual energetic components, this behavior was clearly shown to be caused by the quadrupole–quadrupole electrostatic interaction between the $CO_2$ molecules. The critical value for the quadrupole moment which causes this behavior is clearly between that of $CO_2$ and $N_2$ (which does not display the same isosteric heat properties). The orientational sensitivity of the quadrupole interactions cause the isosteric heat behavior for $CO_2$ to vary across several different nanotube bundle models at high coverage. This behavior is not observed for other adsorbates ($C_2H_6$ and Ar).

For the kinetic regime, a cylindrical pore model was developed using the new simulation scheme to initiate the investigation of the change in behavior of the equilibration time with coverage that was experimentally observed for ethane on closed nanohorns. With the flexibility of the model, the increasing equilibration trend that $CO_2$ displays across all varieties of nanohorns and nanotubes can also be studied. Preliminary simulations were carried out for six model cases which varied in their binding energy profiles, kinetic rates, as well as pore openings. The model case corresponding to a nanohorn, which has a binding energy profile that varies along the length of

the pore, was found to produce a change in the pore occupancy; mainly the highest occupancy was shifted towards the bottom of the pore to the stronger binding sites. This is an important step towards ultimately explaining the change (in the trend of the equilibration time) that occurs for ethane going from a nanotube (pore with no variation in binding energy along the length) to a nanohorn (pore with binding energy variation along the length). It is believed that the high occupancy (overcrowding) at the bottom of the pore is important because when gas-gas interactions are turned on they will be disproportionately enhanced, as each gas atom/molecule will feel the presence of many neighbors. Furthermore, large gas-gas interactions have shown the ability to cause the equilibration time to change from a decreasing trend to an increasing one for polyatomic molecules.[27] Future work will explore this possible path to resolving and understanding the open questions regarding the equilibration time of ethane and carbon dioxide on carbon nanostructure materials.

# Bibliography

[1] D.L. Hartmann et al. "Observations: Atmosphere and Surface". In: *Climate Change 2013: The Physical Science Basis. Contribution of Working Group I to the Fifth Assessment Report of the Intergovernmental Panel on Climate Change*. Ed. by T.F. Stocker et al. Cambridge, United Kingdom and New York, NY, USA: Cambridge University Press, 2013. Chap. 2, pp. 159–254. ISBN: ISBN 978-1-107-66182-0. DOI: 10.1017/CBO9781107415324.008. URL: www.climatechange2013.org.

[2] A Dabrowski. "Adsorption — from theory to practice". In: *Advances in Colloid and Interface Science* 93.1 (2001), pp. 135–224. ISSN: 0001-8686. DOI: https://doi.org/10.1016/S0001-8686(00)00082-8.

[3] L. W. Bruch, Milton W. Cole, and Eugene Zaremba. *Physical Adsorption: Forces and Phenomena*. Dover Publications, 2007.

[4] Wladyslaw Rudzinski and Tomasz Panczyk. "The Langmuirian Adsorption Kinetics Revised: A Farewell to the XXth Century Theories?" In: *Adsorption* 8.1 (Jan. 2002), pp. 23–34. ISSN: 1572-8757. DOI: 10.1023/A:1015214406179.

[5] Sumio Iijima. "Helical microtubules of graphitic carbon". In: *Nature* 354.6348 (Nov. 1991), pp. 56–58. ISSN: 1476-4687. DOI: 10.1038/354056a0. URL: https://doi.org/10.1038/354056a0.

[6] "Nano-aggregates of single-walled graphitic carbon nano-horns". In: *Chemical Physics Letters* 309.3 (1999), pp. 165–170. ISSN: 0009-2614. DOI: https://doi.org/10.1016/S0009-2614(99)00642-9. URL: http://www.sciencedirect.com/science/article/pii/S0009261499006429.

[7] Paramita Karfa et al. "2.07 - Functionalization of Carbon Nanostructures". In: *Comprehensive Nanoscience and Nanotechnology (Second Edition)*. Oxford: Academic Press, Jan. 2019, pp. 123–144. ISBN: 978-0-12-812296-9. URL: http://www.sciencedirect.com/science/article/pii/B9780128035818112251.

[8] A. C. Dillon and M. J. Heben. "Hydrogen storage using carbon adsorbents: past, present and future". In: *Applied Physics A* 72.2 (Feb. 2001), pp. 133–142. ISSN: 1432-0630. DOI: 10.1007/s003390100788. URL: https://doi.org/10.1007/s003390100788.

[9] Vaiva Krungleviciute et al. "Probing the Structure of Carbon Nanohorn Aggregates by Adsorbing Gases of Different Sizes". In: *The Journal of Physical Chemistry C* 112.15 (2008), pp. 5742–5746. DOI: 10.1021/jp710524q.

[10] Vaiva Krungleviciute, Aldo D. Migone, and Michael Pepka. "Characterization of single-walled carbon nanohorns using neon adsorption isotherms". In: *Carbon* 47.3 (2009), pp. 769–774. ISSN: 0008-6223. DOI: https://doi.org/10.1016/j.carbon.2008.11.036. URL: http://www.sciencedirect.com/science/article/pii/S0008622308006088.

[11] Daisuke Kasuya et al. “Selective Production of Single-Wall Carbon Nanohorn Aggregates and Their Formation Mechanism”. In: *The Journal of Physical Chemistry B* 106.19 (2002), pp. 4947–4951. DOI: 10.1021/jp020387n.

[12] Vaiva Krungleviciute et al. “Probing the Structure of Carbon Nanohorn Aggregates by Adsorbing Gases of Different Sizes”. In: *The Journal of Physical Chemistry C* 112.15 (2008), pp. 5742–5746. DOI: 10.1021/jp710524q.

[13] Dinesh. S. Rawat and Aldo. D. Migone. “Non-Monotonic Kinetics of Alkane Adsorption on Single-Walled Carbon Nanotubes”. In: *The Journal of Physical Chemistry C* 116.1 (2012), pp. 975–979. DOI: 10.1021/jp2095455.

[14] Brice A. Russell et al. “Ethane adsorption on aggregates of dahlia-like nanohorns: experiments and computer simulations”. In: *Phys. Chem. Chem. Phys.* 18 (22 2016), pp. 15436–15446. DOI: 10.1039/C6CP01861K. URL: http://dx.doi.org/10.1039/C6CP01861K.

[15] Steve Plimpton. “Fast Parallel Algorithms for Short-Range Molecular Dynamics”. In: *Journal of Computational Physics* 117.1 (1995), pp. 1–19. ISSN: 0021-9991. DOI: https://doi.org/10.1006/jcph.1995.1039. URL: https://lammps.sandia.gov.

[16] Aldo D. Migone. “Chapter Sixteen - Adsorption on Carbon Nanotubes: Experimental Results”. In: *Adsorption by Carbons*. Ed. by Eduardo J. Bottani and Juan [M.D. Tascan]. Amsterdam: Elsevier, 2008, pp. 403–430. ISBN: 978-0-08-044464-2. DOI: https://doi.org/10.1016/B978-008044464-2.50020-1. URL: http://www.sciencedirect.com/science/article/pii/B9780080444642500201.

[17] M. Bienfait et al. “Thermodynamics and structure of hydrogen, methane, argon, oxygen, and carbon dioxide adsorbed on single-wall carbon nanotube bundles”. In: *Phys. Rev. B* 70 (3 July 2004), p. 035410. DOI: 10.1103/PhysRevB.70.035410. URL: https://link.aps.org/doi/10.1103/PhysRevB.70.035410.

[18] D. S. Rawat, T. Furuhashi, and A. D. Migone. “Adsorption Characteristics of Linear Alkanes Adsorbed on Purified HiPco Single-Walled Carbon Nanotubes”. In: *The Journal of Physical Chemistry C* 114.47 (2010), pp. 20173–20177. DOI: 10.1021/jp108242x.

[19] Dinesh. S. Rawat and Aldo. D. Migone. “Non-Monotonic Kinetics of Alkane Adsorption on Single-Walled Carbon Nanotubes”. In: *The Journal of Physical Chemistry C* 116.1 (2012), pp. 975–979. DOI: 10.1021/jp2095455.

[20] Justin Petucci et al. “Thermodynamics and Kinetics of Carbon Dioxide Adsorption on HiPco Nanotubes”. In: *The Journal of Physical Chemistry C* 122.35 (2018), pp. 20410–20418. DOI: 10.1021/acs.jpcc.8b06156. URL: https://doi.org/10.1021/acs.jpcc.8b06156.

[21] Dr. Curt M. White et al. “Separation and Capture of CO2 from Large Stationary Sources and Sequestration in Geological Formations—Coalbeds and Deep Saline Aquifers”. In: *Journal of the Air and Waste Management Association* 53.6 (2003), pp. 645–715. DOI: 10.1080/10473289.2003.10466206.

[22] Douglas Aaron and Costas Tsouris. “Separation of CO2 from Flue Gas: A Review”. In: *Separation Science and Technology* 40.1-3 (2005), pp. 321–348. DOI: 10.1081/SS-200042244.

[23] Klaus S. Lackner. "A Guide to CO2 Sequestration". In: *Science* 300.5626 (2003), pp. 1677–1678. ISSN: 0036-8075. DOI: 10.1126/science.1079033. eprint: https://science.sciencemag.org/content/300/5626/1677.full.pdf. URL: https://science.sciencemag.org/content/300/5626/1677.

[24] Jared T. Burde and M. Mercedes Calbi. "Physisorption Kinetics in Carbon Nanotube Bundles". In: *The Journal of Physical Chemistry C* 111.13 (2007), pp. 5057–5063. DOI: 10.1021/jp065428k.

[25] Jared T. Burde et al. "Kinetics of External Adsorption on Nanotube Bundles: Surface Heterogeneity Effects". In: *The Journal of Physical Chemistry C* 113.39 (2009), pp. 16945–16950. DOI: 10.1021/jp905562y.

[26] Joshua M. Vann, Samantha L. Molnar, and M. Mercedes Calbi. "Equilibration processes during gas uptake inside narrow pores". In: *Phys. Chem. Chem. Phys.* 17 (19 2015), pp. 13021–13027. DOI: 10.1039/C5CP00502G. URL: http://dx.doi.org/10.1039/C5CP00502G.

[27] Jared T. Burde and M. Mercedes Calbi. "Adsorption dynamics of polyatomic molecules on planar surfaces". In: *Phys. Chem. Chem. Phys.* 19 (45 2017), pp. 30715–30725. DOI: 10.1039/C7CP05154A.

[28] Jared T. Burde and M. M. Calbi. "Adsorption kinetics of diatomic molecules". In: *Phys. Chem. Chem. Phys.* 16 (17 2014), pp. 8070–8077. DOI: 10.1039/C3CP55458A.

[29] Jared T. Burde and M. Mercedes Calbi. "Early Removal of Weak-Binding Adsorbates by Kinetic Separation". In: *The Journal of Physical Chemistry Letters* 1.5 (2010), pp. 808–812. DOI: 10.1021/jz900468t.

[30] Cristina Garcia Cardona et al. “Crossing the mesoscale no-mans land via parallel kinetic Monte Carlo.” In: (Oct. 2009). DOI: 10.2172/966942. URL: https://spparks.sandia.gov.

[31] E.M. Lifshitz. “THE THEORY OF MOLECULAR ATTRACTIVE FORCES BETWEEN SOLIDS”. In: *Soviet Phys. JETP* Vol: 2 (Jan. 1956).

[32] Minfang Zhang et al. “Individual Single-Wall Carbon Nanohorns Separated from Aggregates”. In: *The Journal of Physical Chemistry C* 113.26 (2009), pp. 11184–11186. DOI: 10.1021/jp9037705.

[33] V. Krungleviciute et al. “Neon and $CO_2$ Adsorption on Open Carbon Nanohorns”. In: *Langmuir* 29.30 (2013), pp. 9388–9397. DOI: 10.1021/la401033u.

[34] Takeshi Azami et al. “Large-Scale Production of Single-Wall Carbon Nanohorns with High Purity”. In: *The Journal of Physical Chemistry C* 112.5 (2008), pp. 1330–1334. DOI: 10.1021/jp076365o.

[35] S. Talapatra et al. “Gases Do Not Adsorb on the Interstitial Channels of Closed-Ended Single-Walled Carbon Nanotube Bundles”. In: *Phys. Rev. Lett.* 85 (1 July 2000), pp. 138–141. DOI: 10.1103/PhysRevLett.85.138. URL: https://link.aps.org/doi/10.1103/PhysRevLett.85.138.

[36] Matthew R. LaBrosse and J. Karl Johnson. “Defect and Nondefect Interstitial Channel Availability in Carbon Nanotube Bundles: Comparison of Modeling with Experiments”. In: *The Journal of Physical Chemistry C* 114.17 (2010), pp. 7602–7610. DOI: 10.1021/jp910966e.

[37] Christopher Matranga et al. “Trapped CO2 in Carbon Nanotube Bundles”. In: *The Journal of Physical Chemistry B* 107.47 (2003), pp. 12930–12941. DOI: 10.1021/jp0364654.

[38] T. Ohba et al. “N2 Adsorption in an Internal Nanopore Space of Single-Walled Carbon Nanohorn:GCMC Simulation and Experiment”. In: *Nano Letters* 1.7 (2001), pp. 371–373. DOI: 10.1021/nl010030f.

[39] K. Murata et al. “Porosity Evaluation of Intrinsic Intraparticle Nanopores of Single Wall Carbon Nanohorn”. In: *Nano Letters* 1.4 (2001), pp. 197–199. DOI: 10.1021/nl015509m.

[40] T. Ohba and K. Kaneko. “Internal Surface Area Evaluation of Carbon Nanotube with GCMC Simulation-Assisted N2 Adsorption”. In: *The Journal of Physical Chemistry B* 106.29 (2002), pp. 7171–7176. DOI: 10.1021/jp014604g.

[41] Katsuyuki Murata et al. “High-density of methane confined in internal nanospace of single-wall carbon nanohorns”. English. In: *Carbon* 43.13 (Nov. 2005), pp. 2826–2830. ISSN: 0008-6223. DOI: 10.1016/j.carbon.2005.05.043.

[42] Vaiva Krungleviciute et al. “CO2 Adsorption on Dahlia-Like Carbon Nanohorns: Isosteric Heat and Surface Area Measurements”. In: *The Journal of Physical Chemistry C* 116.1 (2012), pp. 306–310. DOI: 10.1021/jp208766u.

[43] Brice Russell et al. “Sorption Kinetics on Open Carbon Nanohorn Aggregates: The Effect of Molecular Diameter”. In: *Molecules* 21.4 (Apr. 2016), p. 521. ISSN: 1420-3049. DOI: 10.3390/molecules21040521. URL: http://dx.doi.org/10.3390/molecules21040521.

[44] Dinesh S. Rawat and Aldo D. Migone. "Phases of ethane adsorbed on purified HiPco single-walled carbon nanotubes". In: *Phys. Rev. B* 75 (19 May 2007), p. 195440. DOI: 10.1103/PhysRevB.75.195440. URL: https://link.aps.org/doi/10.1103/PhysRevB.75.195440.

[45] Fernando J. A. L. Cruz and Erich A. Muller. "Behavior of ethylene and ethane within single-walled carbon nanotubes. 1-Adsorption and equilibrium properties". In: *Adsorption* 15.1 (Feb. 2009), pp. 1–12. DOI: 10.1007/s10450-009-9154-0.

[46] Isabel A.A.C. Esteves et al. "Determination of the surface area and porosity of carbon nanotube bundles from a Langmuirian analysis of sub- and supercritical adsorption data". In: *Carbon* 47.4 (Apr. 2009), pp. 948–956. URL: http://www.sciencedirect.com/science/article/pii/S0008622308006507.

[47] Dinesh S. Rawat and Aldo D. Migone. "Ethylene Films Adsorbed onto Purified HiPco Single Walled Carbon Nanotubes: A Comparison with Ethane and Longer Alkanes". In: *Adsorption Science and Technology* 29.8 (2011), pp. 723–731. DOI: 10.1260/0263-6174.29.8.723.

[48] Alberto G. Albesa et al. "Ethane/Ethylene Adsorption on Carbon Nanotubes: Temperature and Size Effects on Separation Capacity". In: *Langmuir* 28.3 (2012), pp. 1824–1832. DOI: 10.1021/la204314a.

[49] Dinesh S. Rawat, M. Mercedes Calbi, and Aldo D. Migone. "Equilibration Time:Kinetics of Gas Adsorption on Closed- and Open-Ended Single-Walled Carbon Nanotubes". In: *The Journal of Physical Chemistry C* 111.35 (2007), pp. 12980–12986. DOI: 10.1021/jp072786u.

[50] Danny Perez et al. “Long-Time Dynamics through Parallel Trajectory Splicing”. In: *Journal of Chemical Theory and Computation* 12.1 (2016). PMID: 26605853, pp. 18–28. DOI: 10.1021/acs.jctc.5b00916. eprint: https://doi.org/10.1021/acs.jctc.5b00916. URL: https://doi.org/10.1021/acs.jctc.5b00916.

[51] Michael P. Allen and Dominic J. Tildesley. *Computer Simulation of Liquids*. 2nd. USA: Oxford University Press, Inc., 2017. ISBN: 0198803206.

[52] Arthur F. Voter. “INTRODUCTION TO THE KINETIC MONTE CARLO METHOD”. In: *Radiation Effects in Solids*. Ed. by Kurt E. Sickafus, Eugene A. Kotomin, and Blas P. Uberuaga. Dordrecht: Springer Netherlands, 2007, pp. 1–23. ISBN: 978-1-4020-5295-8.

[53] George Stan et al. “Uptake of gases in bundles of carbon nanotubes”. In: *Phys. Rev. B* 62 (3 July 2000), pp. 2173–2180. DOI: 10.1103/PhysRevB.62.2173. URL: https://link.aps.org/doi/10.1103/PhysRevB.62.2173.

[54] W. A. Steele. “Monolayers of Linear Molecules Adsorbed on the Graphite Basal Plane:Structures and Intermolecular Interactions”. In: *Langmuir* 12.1 (1996), pp. 145–153. DOI: 10.1021/la940935r.

[55] Alexei Vernov and William A. Steele. “The electrostatic field at a graphite surface and its effect on molecule-solid interactions”. In: *Langmuir* 8.1 (1992), pp. 155–159. DOI: 10.1021/la00037a029.

[56] Mikulaa Kocman, Martin Pykal, and Petr Jureaka. “Electric quadrupole moment of graphene and its effect on intermolecular interactions”. In: *Phys. Chem. Chem. Phys.* 16 (7 2014), pp. 3144–3152. DOI: 10.1039/C3CP54701A. URL: http://dx.doi.org/10.1039/C3CP54701A.

[57] Xiongce Zhao and J. Karl Johnson. "An Effective Potential for Adsorption of Polar Molecules on Graphite". In: *Molecular Simulation* 31.1 (2005), pp. 1–10. DOI: 10.1080/0892702042000272889.

[58] D.D. Do and H.D. Do. "Effects of quadrupole moments of graphite surface on adsorption of simple gases on graphitized thermal carbon black". In: *Colloids and Surfaces A: Physicochemical and Engineering Aspects* 300.1 (2007), pp. 50–59. ISSN: 0927-7757. DOI: https://doi.org/10.1016/j.colsurfa.2006.10.008. URL: http://www.sciencedirect.com/science/article/pii/S0927775706007473.

[59] L. W. Bruch. "Ground state energy and structure of physisorbed monolayers of linear molecules". In: *The Journal of Chemical Physics* 79.6 (1983), pp. 3148–3156. DOI: 10.1063/1.446146.

[60] Daan Frenkel and Berend Smit. *Understanding Molecular Simulation From Algorithms to Applications*. 2nd. Academic Press, 2002. ISBN: 0122673511.

[61] Marcus G. Martin and J. Ilja Siepmann. "Transferable Potentials for Phase Equilibria. 1. United-Atom Description of n-Alkanes". In: *The Journal of Physical Chemistry B* 102.14 (1998), pp. 2569–2577. DOI: 10.1021/jp972543+.

[62] Jonathan G. Harris and Kwong H. Yung. "Carbon Dioxide's Liquid-Vapor Coexistence Curve And Critical Properties as Predicted by a Simple Molecular Model". In: *The Journal of Physical Chemistry* 99.31 (1995), pp. 12021–12024. DOI: 10.1021/j100031a034.

[63] Justin Petucci et al. "Diffusion, adsorption, and desorption of molecular hydrogen on graphene and in graphite". In: *The Journal of Chemical Physics* 139.4

(2013), p. 044706. DOI: 10.1063/1.4813919. eprint: https://doi.org/10.1063/1.4813919. URL: https://doi.org/10.1063/1.4813919.

[64] Graeme Henkelman and Hannes Jónsson. "Improved tangent estimate in the nudged elastic band method for finding minimum energy paths and saddle points". In: *The Journal of Chemical Physics* 113.22 (2000), pp. 9978–9985. DOI: 10.1063/1.1323224.

[65] Graeme Henkelman, Blas P. Uberuaga, and Hannes Jónsson. "A climbing image nudged elastic band method for finding saddle points and minimum energy paths". In: *The Journal of Chemical Physics* 113.22 (2000), pp. 9901–9904. DOI: 10.1063/1.1329672.

[66] D.W. Heermann. *Computer Simulation Methods in Theoretical Physics*. 2nd. Springer-Verlag, 1990. ISBN: 0387522107.

[67] Randall Q. Snurr, Alexis T. Bell, and Doros N. Theodorou. "Prediction of adsorption of aromatic hydrocarbons in silicalite from grand canonical Monte Carlo simulations with biased insertions". In: *The Journal of Physical Chemistry* 97.51 (1993), pp. 13742–13752. DOI: 10.1021/j100153a051. eprint: https://doi.org/10.1021/j100153a051. URL: https://doi.org/10.1021/j100153a051.

[68] V. A. Bakaev and W. A. Steele. "Grand canonical ensemble computer simulation of adsorption of argon on a heterogeneous surface". In: *Langmuir* 8.1 (1992), pp. 148–154. DOI: 10.1021/la00037a028. eprint: https://doi.org/10.1021/la00037a028. URL: https://doi.org/10.1021/la00037a028.

[69] Jeremy C. Palmer et al. “Adsorptive behavior of CO2, CH4 and their mixtures in carbon nanospace: a molecular simulation study”. In: *Phys. Chem. Chem. Phys.* 13 (9 2011), pp. 3985–3996. DOI: 10.1039/C0CP02281K.

[70] Mie Andersen, Chiara Panosetti, and Karsten Reuter. “A Practical Guide to Surface Kinetic Monte Carlo Simulations”. In: *Frontiers in Chemistry* 7 (2019), p. 202. ISSN: 2296-2646. DOI: 10.3389/fchem.2019.00202. URL: https://www.frontiersin.org/article/10.3389/fchem.2019.00202.

[71] Kristen A. Fichthorn and W. H. Weinberg. “Theoretical foundations of dynamical Monte Carlo simulations”. In: *The Journal of Chemical Physics* 95.2 (1991), pp. 1090–1096. DOI: 10.1063/1.461138. URL: https://doi.org/10.1063/1.461138.

[72] Alexander Slepoy, Aidan P. Thompson, and Steven J. Plimpton. “A constant-time kinetic Monte Carlo algorithm for simulation of large biochemical reaction networks”. In: *The Journal of Chemical Physics* 128.20 (2008), p. 205101. DOI: 10.1063/1.2919546. eprint: https://doi.org/10.1063/1.2919546. URL: https://doi.org/10.1063/1.2919546.

[73] H. Sponer and M. Bruch-Willstatter. “The Lattice Energy of Solid CO2”. In: *The Journal of Chemical Physics* 5.9 (1937), pp. 745–751. DOI: 10.1063/1.1750110.

[74] Xue Yong et al. “Crystal structures and dynamical properties of dense CO2”. In: *Proceedings of the National Academy of Sciences* 113.40 (2016), pp. 11110–11115. ISSN: 0027-8424. DOI: 10.1073/pnas.1601254113.

[75] M. Robinson, I. Suarez-Martinez, and N. A. Marks. "Generalized method for constructing the atomic coordinates of nanotube caps". In: *Phys. Rev. B* 87 (15 Apr. 2013), p. 155430. DOI: 10.1103/PhysRevB.87.155430.

[76] M. Robinson and N.A. Marks. "NanoCap: A framework for generating capped carbon nanotubes and fullerenes". In: *Computer Physics Communications* 185.10 (2014), pp. 2519–2526. ISSN: 0010-4655. DOI: https://doi.org/10.1016/j.cpc.2014.05.029.

[77] Alvaro Gonzalez. "Measurement of Areas on a Sphere Using Fibonacci and Latitude–Longitude Lattices". In: *Mathematical Geosciences* 42.1 (Nov. 2009), p. 49. ISSN: 1874-8953. DOI: 10.1007/s11004-009-9257-x.

[78] A. Terlain and Y. Larher. "Phase diagrams of films of linear molecules with large quadrupole moments (CO2, N2O, C2N2) adsorbed on graphite". In: *Surface Science* 125.1 (1983), pp. 304–311. ISSN: 0039-6028. DOI: https://doi.org/10.1016/0039-6028(83)90467-3.

[79] Justin M. Petucci. "A study of crack propagation in metals in the presence of defects". PhD thesis. 2013, p. 115. ISBN: 978-1-303-07220-8. URL: http://search.proquest.com/docview/1357140733/.

[80] Daniel T Gillespie. "A general method for numerically simulating the stochastic time evolution of coupled chemical reactions". In: *Journal of Computational Physics* 22.4 (1976), pp. 403–434. ISSN: 0021-9991. DOI: https://doi.org/10.1016/0021-9991(76)90041-3.

[81] A.B. Bortz, M.H. Kalos, and J.L. Lebowitz. "A new algorithm for Monte Carlo simulation of Ising spin systems". In: *Journal of Computational Physics* 17.1

(1975), pp. 10–18. ISSN: 0021-9991. DOI: https://doi.org/10.1016/0021-9991(75)90060-1.

[82] Michael A. Gibson and Jehoshua Bruck. "Efficient Exact Stochastic Simulation of Chemical Systems with Many Species and Many Channels". In: *The Journal of Physical Chemistry A* 104.9 (2000), pp. 1876–1889. DOI: 10.1021/jp993732q.

[83] Alexander Slepoy, Aidan P. Thompson, and Steven J. Plimpton. "A constant-time kinetic Monte Carlo algorithm for simulation of large biochemical reaction networks". In: *The Journal of Chemical Physics* 128.20 (2008), p. 205101. DOI: 10.1063/1.2919546.

[84] Dinesh. S. Rawat and Aldo. D. Migone. "Non-Monotonic Kinetics of Alkane Adsorption on Single-Walled Carbon Nanotubes". In: *The Journal of Physical Chemistry C* 116.1 (2012), pp. 975–979. DOI: 10.1021/jp2095455.

[85] D. S. Rawat et al. "Dependence of Single-Walled Carbon Nanotube Adsorption Kinetics on Temperature and Binding Energy". In: *Langmuir* 24.23 (2008), pp. 13465–13469. DOI: 10.1021/la8022002.

[86] Inc. Wolfram Research. *Mathematica, Version 10.2*. URL: https://www.wolfram.com/mathematica.

[87] William A. Steele. "The physical interaction of gases with crystalline solids: I. Gas-solid energies and properties of isolated adsorbed atoms". In: *Surface Science* 36.1 (1973), pp. 317–352. ISSN: 0039-6028. DOI: https://doi.org/10.1016/0039-6028(73)90264-1. URL: http://www.sciencedirect.com/science/article/pii/0039602873902641.

# Appendix

## Appendix A: LJ paraboloid surface

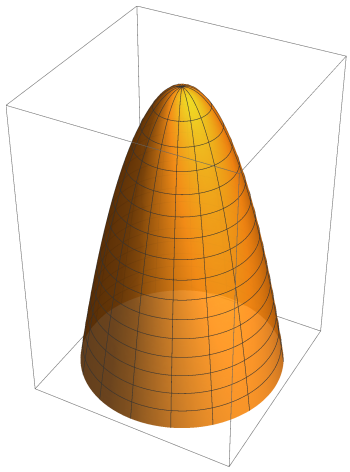

Figure A.1: Paraboloid Surface

One structural model used in this study to represent a carbon nanohorn, which has a radius that varies along its length, is a paraboloid. This surface is created by rotating a parabola about its symmetry axis. A convenient parameterization for a paraboloid of height $h$ and base radius of $R$ is given by,

$$\vec{r}(\rho,\theta) = x(\rho,\theta)\,\hat{i} + y(\rho,\theta)\,\hat{j} + z(\rho,\theta)\,\hat{k} \tag{A.1}$$

$$\vec{r}(\rho,\theta) = R\sqrt{\frac{\rho}{h}}\cos\theta\ \hat{i} + R\sqrt{\frac{\rho}{h}}\sin\theta\ \hat{j} + (h-\rho)\ \hat{k} \tag{A.2}$$

where $0 \leq \theta < 2\pi$ and $0 \leq \rho < h$. For this parameterization, the origin is set to $(0,0,0)$ with a $\hat{k}$ symmetry axis. The paraboloid base sits in the $\hat{i}\hat{j}$ plane.

The differential surface area element for the parameterization given in Eqn. A.2 is,

$$dA = \|\vec{r}_\rho \times \vec{r}_\theta\| d\rho\, d\theta \tag{A.3}$$

where $\vec{r}_\rho$ and $\vec{r}_\theta$ are the surface's tangent vectors given by,

$$\begin{aligned}\vec{r}_\rho(\rho,\theta) &= \frac{d}{d\rho}x(\rho,\theta)\ \hat{i} + \frac{d}{d\rho}y(\rho,\theta)\ \hat{j} + \frac{d}{d\rho}z(\rho,\theta)\ \hat{k} \\ &= \frac{R}{2\sqrt{\rho h}}\cos\theta\ \hat{i} + \frac{R}{2\sqrt{\rho h}}\sin\theta\ \hat{j} - \hat{k}\end{aligned} \tag{A.4}$$

and

$$\begin{aligned}\vec{r}_\theta(\rho,\theta) &= \frac{d}{d\theta}x(\rho,\theta)\ \hat{i} + \frac{d}{d\theta}y(\rho,\theta)\ \hat{j} + \frac{d}{d\theta}z(\rho,\theta)\ \hat{k} \\ &= -R\sqrt{\frac{\rho}{h}}\sin\theta\ \hat{i} + R\sqrt{\frac{\rho}{h}}\cos\theta\ \hat{j}\end{aligned} \tag{A.5}$$

The cross product of these two tangent vectors yields,

$$\vec{r}_\rho \times \vec{r}_\theta = R\sqrt{\frac{\rho}{h}}\cos\theta\ \hat{i} + R\sqrt{\frac{\rho}{h}}\sin\theta\ \hat{j} + \frac{R^2}{2h}\ \hat{k} \tag{A.6}$$

which has a magnitude of,

$$\|\vec{r}_\rho \times \vec{r}_\theta\| = \frac{R}{2h}\sqrt{R^2 + 4\rho h} \tag{A.7}$$

Finally, the differential area element from Eqn. A.3 is given by,

$$dA = \frac{R}{2h}\sqrt{(R^2 + 4\rho h)}\, d\rho\, d\theta \tag{A.8}$$

The Lennard-Jones interaction between an LJ site and a differential patch of carbon, $dn = \Theta\, dA$, on the paraboloid surface can be expressed as,

$$\begin{aligned} d\phi_{LJ} &= 4\epsilon\, dn \left[\left(\frac{\sigma}{d}\right)^{12} - \left(\frac{\sigma}{d}\right)^{6}\right] \\ &= \frac{2\epsilon\Theta R}{h}\sqrt{(R^2 + 4\rho h)}\left[\left(\frac{\sigma}{d}\right)^{12} - \left(\frac{\sigma}{d}\right)^{6}\right] d\rho\, d\theta \end{aligned} \tag{A.9}$$

where $d$ is separation distance between the LJ site and the carbon patch and $\Theta$ is the carbon surface density. For a general LJ site location given in cylindrical coordinates, $(\gamma\cos\psi, \gamma\sin\psi, z)$, the separation distance, $d$, is given by,

$$d^2 = R^2\frac{\rho}{h} + \gamma^2 - 2\gamma R\sqrt{\frac{\rho}{h}}\cos(\theta - \psi) + (h - z - \rho)^2 \tag{A.10}$$

With the above defined $d\phi_{LJ}$ and $d^2$, the interaction due to the entire surface can be obtained through integration,

$$\begin{aligned} \phi_{LJ}(\gamma, \psi, z) &= \iint_A d\phi_{LJ} \\ &= \frac{2\epsilon\Theta R}{h}\int_0^{2\pi}\int_0^{h}\sqrt{(R^2 + 4\rho h)}\left[\left(\frac{\sigma}{d}\right)^{12} - \left(\frac{\sigma}{d}\right)^{6}\right] d\rho\, d\theta \end{aligned} \tag{A.11}$$

$$= \frac{2\epsilon\Theta R}{h} \int_0^{2\pi} \int_0^h \left[ \frac{\sigma^{12}(R^2+4\rho h)^6}{(R^2\frac{\rho}{h}+\gamma^2-2\gamma R\sqrt{\frac{\rho}{h}}\cos(\theta-\psi)+(h-z-\rho)^2)^6} \right] - \left[ \frac{\sigma^6(R^2+4\rho h)^3}{(R^2\frac{\rho}{h}+\gamma^2-2\gamma R\sqrt{\frac{\rho}{h}}\cos(\theta-\psi)+(h-z-\rho)^2)^3} \right] d\rho\, d\theta \quad \text{(A.12)}$$

Due to the azimuthual/cylindrical symmetry of the paraboloid, it is expected that $\phi_{LJ}$ is independent of $\psi$. For an integrable function $f(x)$ with periodicity $T$,

$$\int_0^T f(x)dx = \int_a^{a+T} f(x)dx \quad \text{(A.13)}$$

for $a \in \mathbb{R}$. For the integrand in Eqn. A.12 the periodicity is $T = 2\pi$, due to the cosine function. Applying a substitution of $u = \theta - \psi$ gives,

$$= \frac{2\epsilon\Theta R}{h} \int_{-\psi}^{2\pi-\psi} \int_0^h \left[ \frac{\sigma^{12}(R^2+4\rho h)^6}{(R^2\frac{\rho}{h}+\gamma^2-2\gamma R\sqrt{\frac{\rho}{h}}\cos(u)+(h-z-\rho)^2)^6} \right] - \left[ \frac{\sigma^6(R^2+4\rho h)^3}{(R^2\frac{\rho}{h}+\gamma^2-2\gamma R\sqrt{\frac{\rho}{h}}\cos(u)+(h-z-\rho)^2)^3} \right] d\rho\, du \quad \text{(A.14)}$$

Invoking the relation given in Eqn. A.13 for $a = -\psi$ results in the elimination of $\psi$,

$$\phi_{LJ}(\gamma,z) = \frac{2\epsilon\Theta R}{h} \int_0^{2\pi} \int_0^h \left[ \frac{\sigma^{12}(R^2+4\rho h)^6}{(R^2\frac{\rho}{h}+\gamma^2-2\gamma R\sqrt{\frac{\rho}{h}}\cos(u)+(h-z-\rho)^2)^6} \right] - \left[ \frac{\sigma^6(R^2+4\rho h)^3}{(R^2\frac{\rho}{h}+\gamma^2-2\gamma R\sqrt{\frac{\rho}{h}}\cos(u)+(h-z-\rho)^2)^3} \right] d\rho\, du \quad \text{(A.15)}$$

The above expression for $\phi_{LJ}$, which depends on the horizontal distance of the Lennard-Jones site from the paraboloid symmetry axis ($\gamma$) and the distance above

the base ($z$) is solved using numerical integration methods in the Mathematica[86] software.

# Appendix B: LJ planar surface

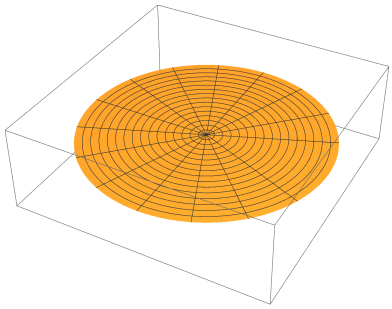

Figure B.1: Planar Surface

One structural model used in this study to represent a graphene sheet is an unstructured planar surface. A convenient parameterization for a planar surface is given by,

$$\vec{r}(\rho,\theta) = x(\rho,\theta)\,\hat{i} + y(\rho,\theta)\,\hat{j} + z(\rho,\theta)\,\hat{k} \tag{B.1}$$

$$\vec{r}(\rho,\theta) = \rho\cos\theta\,\hat{i} + \rho\sin\theta\,\hat{j} \tag{B.2}$$

where $0 \leq \theta < 2\pi$ and $0 \leq \rho < R$ and $R$ is the radius of the circular planar surface centered on $(0,0,0)$ in the $\hat{i}\hat{j}$ plane.

The differential surface area element for the parameterization given in Eqn. B.2 is,

$$dA = \|\vec{r}_\rho \times \vec{r}_\theta\| d\rho\, d\theta \tag{B.3}$$

where $\vec{r}_\rho$ and $\vec{r}_\theta$ are the surface's tangent vectors given by,

$$\begin{aligned} \vec{r}_\rho(\rho,\theta) &= \frac{d}{d\rho}x(\rho,\theta)\,\hat{i} + \frac{d}{d\rho}y(\rho,\theta)\,\hat{j} + \frac{d}{d\rho}z(\rho,\theta)\,\hat{k} \\ &= \cos\theta\,\hat{i} + \sin\theta\,\hat{j} \end{aligned} \tag{B.4}$$

and

$$\begin{aligned}\vec{r}_\theta(\rho,\theta) &= \frac{d}{d\theta}x(\rho,\theta)\ \hat{i} + \frac{d}{d\theta}y(\rho,\theta)\ \hat{j} + \frac{d}{d\theta}z(\rho,\theta)\ \hat{k} \\ &= -\rho\sin\theta\ \hat{i} + \rho\cos\theta\ \hat{j}\end{aligned} \tag{B.5}$$

The cross product of these two tangent vectors yields,

$$\vec{r}_\rho \times \vec{r}_\theta = (\rho\cos^2\theta + \rho\sin^2\theta)\ \hat{k} \tag{B.6}$$

which has a magnitude of,

$$\|\vec{r}_\rho \times \vec{r}_\theta\| = \rho \tag{B.7}$$

Finally, the differential area element is given by,

$$dA = \rho\, d\rho\, d\theta \tag{B.8}$$

The Lennard Jones interaction between a LJ site and a differential patch of carbon, $dn = \Theta\ dA$, on the cylindrical surface can be expressed as,

$$\begin{aligned}d\phi_{LJ} &= 4\epsilon\, dn\ \left[\left(\frac{\sigma}{d}\right)^{12} - \left(\frac{\sigma}{d}\right)^{6}\right] \\ &= 4\epsilon\Theta\rho\left[\left(\frac{\sigma}{d}\right)^{12} - \left(\frac{\sigma}{d}\right)^{6}\right] dz\, d\theta\end{aligned} \tag{B.9}$$

where $d$ is separation distance between the LJ site and $\Theta$ is the carbon surface density. For a general LJ site location given in cylindrical coordinates, $(\gamma\cos\psi, \gamma\sin\psi, z)$, the

separation distance, $d$, is given by,

$$d^2 = \rho^2 + \gamma^2 - 2\rho\gamma\cos(\theta - \psi) + z^2 \tag{B.10}$$

With the above defined $d\phi_{LJ}$ and $d^2$, the interaction due to the entire surface can be obtained through integration,

$$\begin{aligned}\phi_{LJ}(\gamma, \psi, z) &= \iint_A d\phi_{LJ} \\ &= 4\epsilon\Theta \int_0^{2\pi} \int_0^R \rho \left[ \left(\frac{\sigma}{d}\right)^{12} - \left(\frac{\sigma}{d}\right)^{6} \right] d\rho\, d\theta\end{aligned} \tag{B.11}$$

$$= 4\epsilon\Theta \int_0^{2\pi} \int_0^R \left( \frac{\rho\sigma^{12}}{(\rho^2 + \gamma^2 - 2\rho\gamma\cos(\theta - \psi) + z^2)^6} \right) - \left( \frac{\rho\sigma^6}{(\rho^2 + \gamma^2 - 2\rho\gamma\cos(\theta - \psi) + z^2)^3} \right) d\rho\, d\theta \tag{B.12}$$

Invoking the relation given in Eqn. A.13 for $a = -\psi$ results in the elimination of $\psi$,

$$\phi_{LJ}(\gamma, z) = 4\epsilon\Theta \int_0^{2\pi} \int_0^R \left( \frac{\rho\sigma^{12}}{(\rho^2 + \gamma^2 - 2\rho\gamma\cos(\theta) + z^2)^6} \right) - \left( \frac{\rho\sigma^6}{(\rho^2 + \gamma^2 - 2\rho\gamma\cos(\theta) + z^2)^3} \right) d\rho\, d\theta \tag{B.13}$$

The above expression for $\phi_{LJ}$, which depends on the horizontal distance of the Lennard Jones site from the center of the planar disk ($\gamma$) and the distance above the surface ($z$) is solved using numerical integration methods in the Mathematica[86] software. For the special case of an infinite planar surface ($R \to \infty$), without loss of

generality the LJ site can be aligned on the vertical $\hat{k}$ axis ($\gamma \to 0$), which yields,

$$\begin{aligned}
\phi_{LJ}(z) &= 4\epsilon\Theta \int_0^{2\pi} \int_0^{\infty} \left( \frac{\rho\sigma^{12}}{(\rho^2+z^2)^6} \right) - \left( \frac{\rho\sigma^6}{(\rho^2+z^2)^3} \right) d\rho\, d\theta \\
&= 8\epsilon\Theta\pi \int_0^{\infty} \left( \frac{\rho\sigma^{12}}{(\rho^2+z^2)^6} \right) - \left( \frac{\rho\sigma^6}{(\rho^2+z^2)^3} \right) d\rho \\
&= 8\epsilon\Theta\pi \int_0^{\infty} \left( \frac{\rho\sigma^{12}}{(\rho^2+z^2)^6} \right) - \left( \frac{\rho\sigma^6}{(\rho^2+z^2)^3} \right) d\rho \\
&= 2\epsilon\theta\pi\sigma^2 \left[ \frac{2}{5} \left( \frac{\sigma}{z} \right)^{10} - \left( \frac{\sigma}{z} \right)^4 \right]
\end{aligned} \tag{B.14}$$

Eqn. B.14 can be used to approximate the interaction of gas with a single sheet of graphene. Steele[87] has shown that graphite, which is composed of multiple stacked layers of graphene, can also be approximated with an analytic form that is dependent only on the perpendicular distance from the material surface. This expression is derived by representing the top layer of graphite in accordance with Eqn. B.14, while the remaining layers are considered as a continuous solid. The Steele 10-4-3 potential is given by,

$$\phi_{LJ}(z) = 2\epsilon\theta\pi\sigma^2 \left[ \frac{2}{5} \left( \frac{\sigma}{z} \right)^{10} - \left( \frac{\sigma}{z} \right)^4 - \frac{\sigma^4}{3\Delta(0.61\Delta + z)^3} \right] \tag{B.15}$$

where $\Delta$ is the interlayer spacing distance.

# Appendix C: LJ cylindrical surface

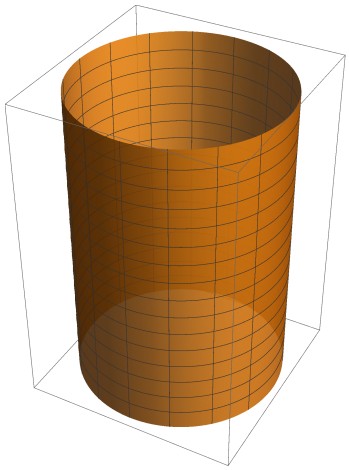

Figure C.1: Cylindrical Surface

One structural model used in this study to represent a carbon nanotube is an unstructured cylindrical surface. A convenient parameterization for a cylindrical surface is given by,

$$\vec{r}(\rho,\theta) = x(z,\theta)\,\hat{i} + y(z,\theta)\,\hat{j} + z(z,\theta)\,\hat{k} \tag{C.1}$$

$$\vec{r}(\rho,\theta) = \rho\cos\theta\,\hat{i} + \rho\sin\theta\,\hat{j} + z\,\hat{k} \tag{C.2}$$

where $0 \leq \theta < 2\pi$ and $\frac{h}{2} \leq z < \frac{h}{2}$, $h$ is the height of the cylinder, and $\rho$ is the radius.

The differential surface area element for the parameterization given in Eqn. C.2 is,

$$dA = \|\vec{r}_z \times \vec{r}_\theta\| dz\, d\theta \tag{C.3}$$

where $\vec{r}_z$ and $\vec{r}_\theta$ are the surface's tangent vectors given by,

$$\begin{aligned}\vec{r}_z(z,\theta) &= \frac{d}{dz}x(z,\theta)\ \hat{i} + \frac{d}{dz}y(z,\theta)\ \hat{j} + \frac{d}{dz}z(z,\theta)\ \hat{k} \\ &= \hat{k}\end{aligned} \tag{C.4}$$

and

$$\begin{aligned}\vec{r}_\theta(z,\theta) &= \frac{d}{d\theta}x(z,\theta)\ \hat{i} + \frac{d}{d\theta}y(z,\theta)\ \hat{j} + \frac{d}{d\theta}z(z,\theta)\ \hat{k} \\ &= -\rho\sin\theta\ \hat{i} + \rho\cos\theta\ \hat{j}\end{aligned} \tag{C.5}$$

The cross product of these two tangent vectors yields,

$$\vec{r}_z \times \vec{r}_\theta = \rho\cos\theta\ \hat{i} + \rho\sin\theta\ \hat{j} \tag{C.6}$$

which has a magnitude of,

$$\|\vec{r}_z \times \vec{r}_\theta\| = \rho \tag{C.7}$$

Finally, the differential area element is given by,

$$dA = \rho\, dz\, d\theta \tag{C.8}$$

The Lennard Jones interaction between an LJ site and a differential patch of carbon, $dn = \Theta\ dA$, on the planar surface can be expressed as,

$$\begin{aligned}d\phi_{LJ} &= 4\epsilon\, dn\ \left[\left(\frac{\sigma}{d}\right)^{12} - \left(\frac{\sigma}{d}\right)^{6}\right] \\ &= 4\epsilon\Theta\rho\left[\left(\frac{\sigma}{d}\right)^{12} - \left(\frac{\sigma}{d}\right)^{6}\right] dz\, d\theta\end{aligned} \tag{C.9}$$

where $d$ is separation distance between the LJ site and $\Theta$ is the carbon surface density. For a general LJ site location given in cylindrical coordinates, $(\gamma\cos\psi, \gamma\sin\psi, z_0)$, the separation distance, $d$, is given by,

$$d^2 = \rho^2 + \gamma^2 - 2\rho\gamma\cos(\theta - \psi) + (z - z_0)^2 \tag{C.10}$$

With the above defined $d\phi_{LJ}$ and $d^2$, the interaction due to the entire surface can be obtained through integration,

$$\begin{aligned}\phi_{LJ}(\gamma, \psi, z_o) &= \iint_A d\phi_{LJ} \\ &= 4\epsilon\Theta \int_0^{2\pi} \int_{-\frac{h}{2}}^{\frac{h}{2}} \rho \left[ \left(\frac{\sigma}{d}\right)^{12} - \left(\frac{\sigma}{d}\right)^{6} \right] dz\, d\theta\end{aligned} \tag{C.11}$$

$$= 4\epsilon\Theta \int_0^{2\pi} \int_{-\frac{h}{2}}^{\frac{h}{2}} \left( \frac{\rho\sigma^{12}}{(\rho^2 + \gamma^2 - 2\rho\gamma\cos(\theta - \psi) + (z - z_0)^2)^6} \right) - \left( \frac{\rho\sigma^{6}}{(\rho^2 + \gamma^2 - 2\rho\gamma\cos(\theta - \psi) + (z - z_0)^2)^3} \right) dz\, d\theta \tag{C.12}$$

Invoking the relation given in Eqn. A.13 for $a = -\psi$ results in the elimination of $\psi$,

$$\phi_{LJ}(\gamma, z_o) = 4\epsilon\Theta \int_0^{2\pi} \int_{-\frac{h}{2}}^{\frac{h}{2}} \left( \frac{\rho\sigma^{12}}{(\rho^2 + \gamma^2 - 2\rho\gamma\cos(\theta) + z^2)^6} \right) - \left( \frac{\rho\sigma^{6}}{(\rho^2 + \gamma^2 - 2\rho\gamma\cos(\theta) + z^2)^3} \right) dz\, d\theta \tag{C.13}$$

The above expression for $\phi_{LJ}$, which depends on the horizontal distance of the Lennard Jones site from the cylinder symmetry axis ($\gamma$) and the distance above

(or below) the $z = 0$ plane ($z_0$) is solved using numerical integration methods in the Mathematica[86] software. For the special case of an infinite tube, $h \to \infty$, the integral can be reduced further,

$$\phi_{LJ}(\gamma, z_o) = 4\epsilon\Theta \int_0^{2\pi} \int_{-\infty}^{\infty} \left( \frac{\rho\sigma^{12}}{(\eta^2 + (z - z_0)^2)^6} \right) - \left( \frac{\rho\sigma^6}{(\eta^2 + (z - z_0)^2)^3} \right) dz\, d\theta \quad \text{(C.14)}$$

where,

$$\eta^2 = \rho^2 + \gamma^2 - 2\rho\gamma\cos(\theta) = \rho^2(1 + \frac{\gamma^2}{\rho^2} - 2\frac{\gamma}{\rho}\cos\theta) \quad \text{(C.15)}$$

$$\begin{aligned}
\phi_{LJ}(\gamma) &= 3\epsilon\Theta\rho\pi \int_0^{2\pi} \left( \frac{21\sigma^{12}}{64\eta^{11}} - \frac{\sigma^6}{2\eta^5} \right) d\theta \\
&= 3\epsilon\Theta\rho\pi \int_0^{2\pi} \frac{(21/64)\sigma^{12}}{\left(\sqrt{\rho^2(1 + \frac{\gamma^2}{\rho^2} - 2\frac{\gamma}{\rho}\cos\theta)}\right)^{11}} - \frac{(1/2)\sigma^6}{\left(\sqrt{\rho^2(1 + \frac{\gamma^2}{\rho^2} - 2\frac{\gamma}{\rho}\cos\theta)}\right)^{5}} d\theta \\
&= 3\pi\epsilon\Theta\sigma^2 \left[ \frac{21}{64} \left( \frac{\sigma}{\rho} \right)^{10} I_{11}(x) - \frac{1}{2} \left( \frac{\sigma}{\rho} \right)^4 I_5(x) \right]
\end{aligned} \quad \text{(C.16)}$$

where,

$$I_n(x) = \int_0^{2\pi} \frac{d\theta}{(1 + x^2 - 2x\cos\theta)^{\frac{n}{2}}}; \qquad x = \frac{\gamma}{\rho} \quad \text{(C.17)}$$

# Appendix D: LJ hemispherical surface

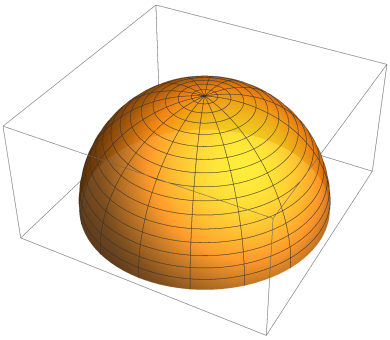

Figure D.1: Hemispherical Surface

One structural model used in this study to represent the cap of a carbon nanotube is an unstructured hemispherical surface. A convenient parameterization for a hemispherical surface of radius $\rho$ is given by,

$$\vec{r}(\rho,\theta) = x(\theta,\phi)\,\hat{i} + y(\theta,\phi)\,\hat{j} + z(\theta,\phi)\,\hat{k} \tag{D.1}$$

$$\vec{r}(\rho,\theta) = \rho\sin\theta\cos\phi\,\hat{i} + \rho\sin\theta\sin\phi\,\hat{j} + (\cos\theta + h)\,\hat{k} \tag{D.2}$$

where $0 \leq \theta < \pi$, $0 \leq \phi < 2\pi$, and $z = h$ is the location of the base of the hemispherical surface in the $\hat{i}\hat{j}$ plane.

The differential surface area element for the parameterization given in Eqn. D.2 is,

$$dA = \|\vec{r}_\theta \times \vec{r}_\phi\| d\theta\, d\phi \tag{D.3}$$

where $\vec{r}_z$ and $\vec{r}_\theta$ are the surface's tangent vectors given by,

$$\begin{aligned}\vec{r}_\theta(\theta,\phi) &= \frac{d}{d\theta}x(\theta,\phi)\ \hat{i} + \frac{d}{d\theta}y(\theta,\phi)\ \hat{j} + \frac{d}{d\theta}z(\theta,\phi)\ \hat{k} \\ &= \rho\cos\theta\cos\phi\ \hat{i} + \rho\cos\theta sin\phi\ \hat{j} - \rho\sin\theta\ \hat{k}\end{aligned} \tag{D.4}$$

and

$$\begin{aligned}\vec{r}_\phi(\theta,\phi) &= \frac{d}{d\phi}x(\theta,\phi)\ \hat{i} + \frac{d}{d\phi}y(\theta,\phi)\ \hat{j} + \frac{d}{d\phi}z(\theta,\phi)\ \hat{k} \\ &= -\rho\sin\theta\sin\phi\ \hat{i} + \rho\sin\theta\cos\phi\ \hat{k}\end{aligned} \tag{D.5}$$

The cross product of these two tangent vectors yields,

$$\vec{r}_\theta \times \vec{r}_\phi = \rho^2\sin^2\theta\cos\phi\ \hat{i} + \rho^2\sin^2\theta\sin\phi\ \hat{j} + \rho^2\sin\theta\cos\theta\ \hat{k} \tag{D.6}$$

which has a magnitude of,

$$\|\vec{r}_\theta \times \vec{r}_\phi\| = \rho^2\sin\theta \tag{D.7}$$

Finally, the differential area element is given by,

$$dA = \rho^2\sin\theta\, d\theta\, d\phi \tag{D.8}$$

The Lennard Jones interaction between an LJ site and a differential patch of carbon, $dn = \Theta\ dA$, on the hemispherical surface can be expressed as,

$$\begin{aligned}d\phi_{LJ} &= 4\epsilon\, dn\ \left[\left(\frac{\sigma}{d}\right)^{12} - \left(\frac{\sigma}{d}\right)^{6}\right] \\ &= 4\epsilon\Theta\rho^2\sin\theta\left[\left(\frac{\sigma}{d}\right)^{12} - \left(\frac{\sigma}{d}\right)^{6}\right] d\theta\, d\phi\end{aligned} \tag{D.9}$$

where $d$ is separation distance between the LJ site and $\Theta$ is the carbon surface density. For a general LJ site location given in cylindrical coordinates, $(\gamma\cos\psi, \gamma\sin\psi, z)$, the separation distance, $d$, is given by,

$$d^2 = (h-z)^2 + \gamma^2 + \rho^2 + 2(h-z)\rho\cos\theta - 2\gamma\rho\cos(\phi-\psi)\sin\theta \tag{D.10}$$

With the above defined $d\phi_{LJ}$ and $d^2$, the interaction due to the entire surface can be obtained through integration,

$$\begin{aligned}\phi_{LJ}(\gamma,\psi,z) &= \iint_A d\phi_{LJ} \\ &= 4\epsilon\Theta\rho^2 \int_0^{2\pi}\int_0^{\pi} \sin\theta \left[\left(\frac{\sigma}{d}\right)^{12} - \left(\frac{\sigma}{d}\right)^{6}\right] d\theta\, d\phi\end{aligned} \tag{D.11}$$

$$\begin{aligned}= 4\epsilon\Theta\rho^2 \int_0^{2\pi}\int_0^{\pi} &\left(\frac{\sigma^{12}\sin\theta}{((h-z)^2+\gamma^2+\rho^2+2(h-z)\rho\cos\theta-2\gamma\rho\cos(\phi-\psi)\sin\theta)^6}\right) - \\ &\left(\frac{\sigma^{6}\sin\theta}{((h-z)^2+\gamma^2+\rho^2+2(h-z)\rho\cos\theta-2\gamma\rho\cos(\phi-\psi)\sin\theta)^3}\right) d\theta\, d\phi\end{aligned} \tag{D.12}$$

Invoking the relation given in Eqn. A.13 for $a = -\psi$ results in the elimination of $\psi$,

$$\begin{aligned}\phi_{LJ}(\gamma,z) = 4\epsilon\Theta\rho^2 \int_0^{2\pi}\int_0^{\pi} &\left(\frac{\sigma^{12}\sin\theta}{((h-z)^2+\gamma^2+\rho^2+2(h-z)\rho\cos\theta-2\gamma\rho\cos(\phi)\sin\theta)^6}\right) - \\ &\left(\frac{\sigma^{6}\sin\theta}{((h-z)^2+\gamma^2+\rho^2+2(h-z)\rho\cos\theta-2\gamma\rho\cos(\phi)\sin\theta)^3}\right) d\theta\, d\phi\end{aligned} \tag{D.13}$$

The above expression for $\phi_{LJ}$, which depends on the horizontal distance of the Lennard Jones site from the hemispherical symmetry axis ($\gamma$) and the distance above

(or below) the $z = 0$ plane ($z$) is solved using numerical integration methods in the Mathematica[86] software.